WIND TUNNEL TESTING OF A NACELLE BYPASS CONCEPT FOR A QUIET SUPERSONIC AIRCRAFT

BY

YONG HAN YEONG

THESIS

Submitted in partial fulfillment of the requirements
for the degree of Master of Science in Aerospace Engineering
in the Graduate College of the
University of Illinois at Urbana-Champaign, 2009

Urbana, Illinois

Advisers:

Professor Michael Bragg
Professor Gregory Elliott

Abstract

Sonic boom attenuation is a considerable design challenge to enable civilian aircraft to operate at supersonic flight conditions. One technology proposed by Gulfstream Aerospace Corporation for the production of low-noise supersonic aircraft is the high-flow nacelle bypass concept in which an outer nacelle surface is used to encircle the asymmetric external engine protuberances of a traditional turbine engine. Although this bypass flow may reduce the overall sonic boom signature of the vehicle, the engine gearbox and protuberances create a highly complex 3-D flow in the annular bypass region. To better understand the 3-D flow features, an approximately 1/6th engine model was tested in a newly constructed 11.1 inch diameter axisymmetric test section of a subsonic wind tunnel at the University of Illinois at Urbana Champaign. By rotating the test section, pressure measurements were obtained over a range of circumferential angles and radial positions. The pressure measurements were used to create planar maps of nondimensionalized total and dynamic pressure upstream and downstream of the bypass model. Wind tunnel testing was performed on the empty axisymmetric wind tunnel followed by model configurations of increasing complexity until a full test configuration of the engine model with the gearbox fairing and crane beam mounts was achieved. Results show significant pressure loss behind the gearbox fairing further characterized using surface flow visualization. Due to the blockage created by the gearbox fairing mounted at the underside of the model, results also show increased flow velocity in the upper section of the bypass duct.

Acknowledgments

Conducting this research project has been challenging. Nevertheless, the experience has been ultimately rewarding and I have enjoyed it tremendously. The completion of this phase of the research is made possible with the assistance from various outstanding individuals.

First, my sincere thanks goes out to Associate Dean and Professor Michael Bragg and Professor Gregory Elliott for providing me with the opportunity to work on this exicting project. Your guidance over the period of my masters program is invaluable. Thanks also goes out to Dr. Andy Broeren, former research scientist in the department for the assistance provided during the initial phase of this project. I would also like to thank fellow colleagues in the Icing Research and Aircraft Aerodynamics Group, Greg Busch and Joe Bottalla for their assistance with the facility design and construction. Special thanks goes out to Nachiket Kale for helping in the design of the test section rotational system as well as with the LabVIEW coding.

Finally, I want to thank my parents for their love, faith and support. Your sacrifices over the years for the sake of my higher education have been tremendous and for that I thank you from the bottom of my heart.

Table of Contents

List of Tables

List of Figures

Nomenclature

A	Area
C_p	Surface static pressure coefficient
D	Diameter at the start of the contraction cone
L	Length of the contraction cone
M	Mach number
N	Diffuser length
P	Pressure
Q	Dynamic pressure
R	Radius
T	Temperature
U	Velocity
$\tilde{u}$	Flow nonuniformity
W	Uncertainty
W_1	Diameter of duct before aft body diffuser
x	Axial coordinate of the cubic arc for the contraction cone
X_m	Matching point of cubic arcs for the contraction cone
X	X_m/L

Greek Symbols

ρ	Air density
γ	Air specific heat
θ	Conical diffusive angle
Δ	Difference

Acronyms

2-D	Two dimensional
3-D	Three dimensional
A/D	Analog to Digital
CAD	Computer-Aided Design
CFD	Computational Fluid Dynamics
CR	Contraction Ratio
DARPA	Defence Advanced Research Projects Agency
EEPROM	Electrically Erasable Programmable Read-Only Memory
ESP	Electronically Scanned Pressure
FAA	Federal Aviation Administration
LCD	Liquid Crystal Display
LED	Light Emitting Diode
NASA	National Aeronautics and Space Administration
NI	National Instruments Corporation
PVC	Polyvinyl Chloride
RPM	Rotations Per Minute
RSM	Reynolds Stress Model
SSBD	Shaped Sonic Boom Demonstrator
SST	Supersonic Transport
SLA	Stereolithography
VFD	Variable Frequency AC Drive

Subscripts

1	Upstream location of wind tunnel inlet
2	Downstream location of wind tunnel inlet
3	Location corresponding to the start of the axisymmetric tunnel section
4, inlet	Location corresponding to the start of the bypass annulus
amb	Ambient condition
avg	Averaged
baseline	Engine baseline model
core	Area at the center of the tunnel excluding boundary-layer regions
inner	Radius of the engine baseline model wall
m	Point of measurement
max	Maximum
model	Engine baseline model with blockage component attached
non-dim.	Nondimensionalized
outer	Radius of the tunnel wall
s	Static pressure
t	Total pressure
tunnel	Empty tunnel
tap1	First axial surface static tap
%	Percent

Superscipts

*	Normalized radius

Chapter 1

Introduction

1.1 Background

1.1.1 History and Challenges of Civil Supersonic Flight

Since the introduction of civil aviation, almost all commercial flights have been operated subsonically. Through out the years, the technology of these civil subsonic aircraft has improved. For example, major improvements in aircraft aerodynamics and engine technology have resulted in a drastic decrease in fuel burned. A study conducted in the 1990's shows that for long-range cruise mode, fuel consumption has decreased more than 64% for an aircraft designed with a range of less than 4000 miles as compared to 30 years ago.[1] The success of the operation of civil subsonic aircraft has also resulted in a decrease in operating costs per passenger seat and subsequently led to an increase in the number of aircraft passengers. According to the Bureau of Transportation Statistics, the number of scheduled domestic and international passengers on U.S. airlines for the full year of 2008 reached 740 million.

However, similar success has not been reached by civil supersonic aviation. There have only been three significant civil supersonic programs, the Tupolev Tu-144, the Boeing 2707 supersonic transport (SST), and the Concorde.[2] The Tupolev TU-144 was the first civil aircraft in the world to break the speed of sound and subsequently reach a maximum cruising speed above Mach 2.3.[3] However, two crashes involving fatalities resulted in the termination of the program just seven months after it entered service. After securing funding from the U.S. government to build a supersonic transport jet, the Boeing company initiated the Boeing 2707 program to compete with the TU-144 and Concorde programs. However, rising developmental costs and subsequent funding cut from the U.S. Senate in the later

stages of design prompted the cancellation of the project. Hence, the Concorde was the only successful civil supersonic aircraft until it was taken out of service in 2003. The reason behind the Concorde's success is that the aircraft was able to display operational safety characteristics and performance consistent with the current fleet of commercial subsonic aircraft. The technical innovations - intake flow management, after burning, center of gravity control as well as the operational innovations - transonic acceleration and deceleration and supercruise were all proven to be reliable.[4]

However, even with the ability to fly reliably at supersonic speeds, the Concorde was not considered to be a practical civil supersonic aviation. This is partly because the Concorde was restricted from supersonic flight over land due to its loud sonic boom. The boom "carpet" was about 40 nautical miles wide and extends forward for 35 nautical miles after the aircraft has slowed to subsonic speeds. Therefore, for a cross-atlantic flight, the Concorde's deceleration and descent has to be planned carefully so that the aircraft is subsonic at least 50 miles before reaching land as not to affect coastal residents.[5] For flights across Europe and the Middle East, for example from London to Bahrain, the Concorde flight path has to follow flight points that were carefully selected so that the aircraft can avoid noise sensitive areas. These flight points were termed "Ghost Waypoints".[5] Therefore, these flight restrictions severely prevented the Concorde from becoming more than just an aviation novelty.

Current Federal Aviation Administration(FAA) rules prohibit supersonic flight over land due to noise concerns. In Title 14, Volume 2, Chapter 1, Section 91.817, Federal Aviation Regulations state that:

1. *No person may operate a civil aircraft in the United States at a true flight Mach number greater than 1 except in compliance with conditions and limitations in an authorization to exceed Mach 1 issued to the operator under appendix B of this part.*

2. *In addition, no person may operate a civil aircraft for which the maximum operating limit speed M_{M0} exceeds a Mach number of 1, to or from an airport in the United States, unless*

   (a) *Information available to the flight crew includes flight limitations that ensure that*

flights entering or leaving the United States will not cause a sonic boom to reach the surface within the United States; and

(b) *The operator complies with the flight limitations prescribed in paragraph (b)(1) of this section or complies with conditions and limitations in an authorization to exceed Mach 1 issued under appendix B of this part.*

The main reason for the restriction of supersonic flight as stated in the Federal Aviation Regulations is due to noise concerns over land. Therefore, for civilian aircraft to fly unrestricted at supersonic speeds, low-boom flight has to be achieved. Although design methodologies and our understanding of supersonic flight has improved since the design of the Concorde, low-noise supersonic flight continues to challenge aircraft designers.

1.1.2 Formation of Sonic Boom

When an aircraft travels at supersonic speeds, it is moving faster than the speed of sound. Therefore, the aircraft moves out and ahead of its sound waves, creating a Mach Cone. Since flow information within the Mach Cone cannot propagate upstream, two zones are effectively created; a zone of silence in front of the Mach Cone and ahead of the aircraft and a zone of action located over and aft of the aircraft. This is shown in Fig. 1.1.[6]

When the Mach Cone passes by a person on the ground, the person will be suddenly exposed to the zone of action and will experience the immediate overpressure as a sonic boom. The pressure will steadily decline across the length of the aircraft into negative pressures at the tail before suddenly rising again to return to normal pressure conditions. This creates a "double boom" effect. This pattern of pressure variation is also commonly known as the "N" wave when plotted against time. An example of the "N" wave characteristic of an F-15 aircraft is shown in Fig. 1.2. However, passengers in the supersonic aircraft will not experience the same sonic boom effect as compared to the person on the ground because they always stand fixed relative to the Mach Cone and never pass through them. The effect of the sonic boom on the ground can be perceived as a detonation noise, resembling the noise of thunder.[7]

The "double boom" effect is also known as the primary sonic boom because it reaches the ground and is under the aircraft. There is also a portion of pressure disturbance that propagates upward away from the aircraft and is called "over-the-top" boom which is still not clearly understood. It is less predictable than the primary sonic boom, has a more random signature as compared to the "N" wave and travels a longer distance through the atmosphere. The effect of this boom when observed from the ground varies and is largely dependent upon atmospheric conditions.[7]

1.2 Motivation

1.2.1 Sonic Boom Suppression Technologies

To minimize sonic boom, the goal is reduce the two rising peaks of the "N" wave of a supersonic aicraft. Seebass and George[8] attempted to reduce the overpressure signatures by careful aerodynamic design of the aircraft. By changing the area development of the equivalent body of revolution, they proved that the sonic boom signature can be reduced to levels just below 1 lb/ft^2.

In 2003, in a DARPA/NASA Quiet Supersonic Platform program, the forward fuselage of an F-5E aircraft was modified and shaped to become the Shaped Sonic Boom Demonstrator(SSBD)(Fig. 1.3a). The modified aircraft was flown supersonically over Harper Lake, California and its overpressure signatures on the ground were recorded. Results were compared against an unmodified F-5E aircraft in Fig. 1.3b where the Shaped Sonic Boom Demonstator produced a lower "flat top" overpressure signature as compared to the peak signature from the F5-E aircraft.[9] This breakthrough in low boom research proved that the boom signature of a supersonic aircraft could be controlled using careful shaping of the vehicle.

Recently, Gulfstream Aerospace Corporation has been developing sonic boom suppresion technologies. One of the low boom technologies that was developed was the the Quiet Spike^{TM}. The Quiet Spike^{TM} is an extendable nose cone that morphs the forward fuselage of the aircraft into a needle-like shape during supersonic flight to reduce the overpressure signatures propagating from the front of the vehicle (Fig. 1.4).[10] Flight tests at speeds of

up to Mach 1.8 on a NASA F-15 research aircraft where the Quiet Spike^{TM} technology was implemented show that the Quiet Spike^{TM} transforms the forward half of the sonic boom into a low pressure characteristic resembling a weak sine half-wave.[11]

1.2.2 High Flow Nacelle Bypass Concept

The development of sonic boom technologies thus far have been focused on forward fuselage morphing techniques. However, to collectively soften an entire aircraft's sonic boom characteristic, additional techniques are needed for the attenuation of the second peak of the "N" wave which is caused by the highly 3-D flowfield around the wing, empennage and engine nacelle. This introduces a more challenging design problem as compared to the front section of the aircraft and requires the use of additional and concurrent technologies involving shaping options for both the airframe and propulsion system.[12,13,14,15,16]

One of the propulsion system low-boom concepts developed by Gulfstream Aerospace Corporation, and also the subject of this thesis is the High Flow Nacelle Bypass Concept. This concept involves using an outer nacelle surface to increase the engine inlet's mass capture, circularize the nacelle around non-axisymmetric external engine protuberances and reduce the projected surface profile presented by the nacelle to incoming supersonic flow.[17,18] As shown in Fig. 1.5a, a traditional nacelle has an outer nacelle that completely covers the inlet, engine and nozzle. Comparatively, a High-Flow Bypass Nacelle (Fig. 1.5b) has an outer nacelle that not only completely circularizes the inlet, engine and nozzle but also creates a duct between the surfaces of the nacelle and the engine. Therefore, incoming flow will be split into two paths; the first path being the primary flow into the engine, the second path being the nacelle bypass flow through the duct. Hence, the exhaust of the entire propulsion system will be the combination of the primary exhaust from the engine and the bypass flow exhaust.

1.2.3 Advantages and Challenges of the Nacelle Bypass Concept

Referring to Fig. 1.5a, it can be observed that there is a gearbox on the lower quadrant of the engine. By using a traditional nacelle, the outer surface of the nacelle follows the engine gearbox geometry. Hence, this creates a large external bulge at the under-side of the

engine nacelle. When exposed to incoming supersonic flow, the bulge creates a nacelle pressure drag, increases the nacelle-airframe-wing interference drag and collectively increase the strength of the second sonic boom assosicated with the aft-features of a supersonic aircraft. However, with the Nacelle Bypass Concept, the outer nacelle is shaped so that there will be minimal surface bulging from the gearbox (Fig. 1.6). This reduces the undersirable effects associated with a traditional nacelle. In addition to lowering the pressure and interference drag, the nacelle bypass flow increases the primary stream thrust from improved core flow total pressure recovery. Concurrently, the nacelle's contribution to overall boom signature of the supersonic aircraft is reduced.

However, the Nacelle Bypass Concept is not without its challenges. Fully circularizing a nacelle around legacy-type engines can require nacelle bypass levels of up to 100% or more of the primary engine flow demand.[18] More importantly, as observed in Fig. 1.5b, the bypass flow path is obstructed with various engine components; the largest component being the gearbox. The bypass flow path is also blocked by a pair of crane beam mounts whose purpose is to structurally connect the engine and its nacelle to the aircraft fuselage. Refering to Fig. 1.7, a combination of inlet splitter, gearbox fairing, engine aero-shroud and exhaust features can be collectively used to capture, subsonically diffuse and divert the flow around the gearbox blockage, then choke and re-expand the flow to supersonic speeds within the bypass nozzle.[18] This creates a bypass geometry that will result in a highly complex 3-D flow field within the duct. Therefore, the success of the Nacelle Bypass concept is compromised due to the degradation of flow within the bypass.

1.3 Objectives and Approach

Due to the complexity of the bypass flow path geometry, predicting the behavior of the flow-field is challenging. Therefore, experimental studies of the flow geometry are useful in providing flow-field data for the validation of numerical results. This thesis focuses on the experimental work conducted at the Aerodynamics Research Lab at the University of Illinois-Urbana Champaign with the following objectives:

1. Understand the steady state characteristics of the bypass flow at the exit station

2. Assess the effect of external engine components/geometry on bypass flow-field

3. Provide flow-field data for CFD validation and development

The following chapter, Experimental Methodologies, will contain details about how a unique wind tunnel facility was designed and fabricated for the testing of a subscale High-Flow Nacelle Bypass model produced by Gulfstream Aerospace Corporation. Results from the experimental tests will be analyzed and discussed in detail in the 3rd chapter, Results and Disucssion. The final chapter summarizes this experimental study with conclusions.

Chapter 2

Experimental Methods

This chapter provides details about the methods used to perform an experimental simulation of the bypass flow path in a wind tunnel facility. First, the test model for the turbofan engine used for the Nacelle Bypass Concept is described. This chapter also includes details about the modification of an existing 15 inch x 15 inch wind tunnel facility into a bypass facility. A description will be provided about the operation of this facility. The chapter ends with a discussion on the data acquisition techniques and methods of nondimensionalization employed for flow variables in this experimental effort with an uncertainty analysis.

2.1 Experimental Models

The experimental model consists of different components: the engine component simulating the shroud covering the turbofan engine, and the primary blockage feature within the bypass annulus consisting of the engine gearbox fairing and a pair of crane beams. Front and aft "non-engine" flow components are also attached on the experimental model. Each of these components is described with a description of the model assembly process.

2.1.1 Rolls Royce Tay Turbofan Engine

The engine component of the full test model is scaled from a high-flow bypass concept developed by Gulfstream for the Rolls Royce Tay turbofan engine. The full scale article is sized to flow at supersonic on-design operating condition with a mass fraction equivalent to approximately 70 % of Tay engine flow demand, and this ratio sets the key radial dimensions of the test model. Taking into consideration the constraints of the axisymmetric test section of the bypass wind tunnel facility which is described in Section 2.2, the engine test model

was scaled to be approximately 1/6th of the full-scale article. A full surface laser scan of the Rolls Royce Tay Turbofan Engine can be seen in Fig. 1.5b.

2.1.1.1 Engine Baseline Model

The bypass flow path begins at the face of the inlet splitter and terminates at the end of the nozzle and are labelled bypass inlet and bypass outlet, respectively, as shown in Fig. 1.5b. However, as observed in Fig. 1.5b, the bypass flow path expands at regions around the turbofan engine and contracts again near the choke plane, creating a "pinch-waist" design. Referring further to Fig. 1.5b, other than the gearbox component located at the under-side of the engine, there are also several components located on the surface of the turbofan engine. These components create more protrusions along the bypass flow path in addition to the gearbox component. Hence, simulating this flow path to understand the fundamental steady-state flow characteristics of the annulus will be experimentally challenging. To simplify the geometry of the flow path, an axisymmetric shroud was introduced to enclose the inlet, engine component and the nozzle (Fig. 1.7). This design creates an annular bypass flow path consisting of a smooth, constant diameter cylinder referred to as the engine baseline model. The protrosion from the gearbox component remains in place and will be enclosed by a gearbox fairing which will be discussed in Section 2.1.1.2.

The total length of the engine baseline model represents the core section from the bypass inlet to the bypass outlet and is 37.7 inches long with a diameter of 8.42 inches (Fig. 2.1). The entire model was fabricated using a rapid prototyping technique called Stereolithography (SLA) at Gulfstream Aerospace Corporation in Savannah, Georgia. Stereolithography is a technique in which layers of ultraviolet photopolymer resin are cured and solidified by an ultraviolet laser to fabricate a high precision model with a high quality surface finish. Further information about stereolithography can be found in Gebhardt.[19] Due to the size of the engine baseline model, the model was split and fabricated in five parts. The different engine baseline segments with their respective lengths can be found in Fig. 2.2. At the center of the bypass baseline pieces is a square shaped cavity with support struts or webbing with a thickness of 0.25 inches (Fig. 2.3). Futher discussion will be made about the cavity design in Section 2.1.3. To connect these different parts together to form a complete

engine baseline model, tabs were designed to protrude an inch out of each of these baseline segments. The tabs are 0.3 inch thick curved plates designed to match and connect to the inner surface of the engine baseline model segments (Fig. 2.4). These tabs will fit into the center cavity of the next corresponding baseline segment to form a connection between the two seperate parts. A series of figures on how the engine baseline segments are connected are shown in Fig. 2.5. After fabrication, the models were then sanded down and painted black.

Since the gearbox fairings and the crane beams will be attached to the engine baseline model, holes at specific locations on the engine baseline segments were fabricated via Stereolithography to serve as pilot holes for the attachment of those blockage components. Once the rapid protypting fabrication was completed, the pilot holes were drilled to a larger size and matched with the holes from the blockage components to ensure an accurate fit.

2.1.1.2 Gearbox Fairing

As observed in Fig. 1.5b, the gearbox component of the Tay turbofan engine provides the main blockage feature within the bypass flow path. To improve the flow quality around and aft of the gearbox, a fairing consisting of an in-flow diverter, main and close-out fairing was designed. These components were designed to attach flush to the under side surface of the engine baseline model and were also fabricated via the Stereolithography technique. Fig. 2.6 and Fig. 2.7 shows a CAD and Stereolithography model for the gearbox fairing respectively.

The in-flow diverter is at a longitudinal location immediately aft of the inlet splitter leading edge on the full-scale geometry. Moving 12.3 inches aft of its leading edge, the diverter expands about a plane of symmetry, reaching its maximum circumferential blockage extent of 110° at a longitudinal position corresponding to the Tay turbofan engine face for the full-scale configuration. This maximum circumferential blockage extent, representing the main gearbox fairing, is maintained at constant value aft for 8.41 inches. The close-out fairing then extends for an additional 6.39 inches. The main gearbox fairing employs full blockage in the radial direction, whereas the closeout fairing itself uses a wedged beavertail that pulls steadily away from the outer engine baseline model wall and terminates radially

with the surface of the core cylinder at a flushed interface. The total length of the fairing is 27.1 inches. The position of these fairing components with respect to the Tay turbofan engine and the nacelle is shown in Fig. 1.7. For the purpose of attachment to the engine baseline model, countersunk through-holes were fabricated on the gearbox fairing; two each on the in-flow diverter and close-out fairing and four on the main gearbox fairing.

2.1.1.3 Crane Beams

The main gearbox fairing is not the only blockage component within the bypass flow path. A pair of crane beam-type mounts are used to structurally attach the entire engine nacelle to the aircraft fuselage. These are represented in the test model by two identical beams, modified for high flow pass-through and attached to the engine baseline model in tandem. The forward and aft crane-beams are located 16.8 inches and 25.6 inches aft of the leading edge of the gearbox fairing in-flow diverter, respectively. This is shown in Fig. 2.8a. Each beam spans 105° circumferentially, with the center-point of the beam's arc located 142.5° from the gearbox fairing's plane of symmetry. Each beam is also 0.96 inches along its radial extent with a longitudinal depth of 0.67 inches. Six webs, spaced equidistantly in the circumferential direction, divide each beam, each web of 0.05 inch thickness as shown in Fig. 2.8b. Once attached to the engine baseline model, a 0.22 inch and 0.16 inch gap separates the outboard and inboard surface of each beam from the nacelle inner wall and engine baseline model wall, respectively. These two walls form an annulus which will represent the bypass flow path. Futher information about simulating the inner nacelle wall will be described in Section 2.2. An oblique view showing the placement of the crane beams on the engine baseline model is shown in Fig. 2.9. As observed in Fig. 2.10, the crane beams are mounted onto the baseline model via four struts located on the crane beams inboard surface.

2.1.2 Front and Aft Flow Components

The installation of the turbofan engine model consisting of the engine baseline model with the attached blockage components of gearbox fairing and crane beams in a wind tunnel facility requires the installation of additional "non-engine" flow components at the front

and aft of the engine model. The assembly of these flow component with the full engine model described from Section 2.1.1.1 to Section 2.1.1.3 will form the full test model.

2.1.2.1 Contraction Cone

The function of the contraction cone is to guide incoming flow from the wind tunnel inlet as uniformly as possible and without flow seperation into the bypass inlet section. To accomplish this goal, practical wind tunnel contraction design guidelines from Morel[20] were studied and implemented. Due to adverse pressure gradients near the wall at both the contraction inlet and outlet, the exit velocity profile will be non-uniform and if the design is not treated with care, flow seperation will occur at the contraction exit. One quick solution to the problem is to increase the contraction length to reduce the pressure gradients. However, this solution method is not practical due to issues concerning cost and space. In addition, the long contration length will promote undesirable boundary-layer growth.

Therefore, the contraction cone was designed to be two matching cubic arcs with low flow separation and non-uniformity values. Information about the contraction cone design is detailed in Appendix A. Once the contraction design was validated by computational fluid dynamics (CFD) calculations, the design was finalized. Fig. 2.11 shows a CAD rendering of the contraction cone with different views. To minimize the risk of injury with a sharp-ended cone, the tip of the cone was slightly rounded. Four struts were also added 3.8 inches aft of the tip of the cone to provide structural support for the test model installed within the test facility. Since the struts were located upstream from the bypass inlet section, they were designed to be in the shape of a NACA 0012 airfoil to reduce undesirable flow disturbances into the inlet section. The struts are 2 inches long with a thickness of 0.24 inches and are located 90° circumferentially from each other. To simplify the installation of the contraction cone within the axisymmetric test facility, half inch spacers were attached to each end of the struts. These spacers are also in a shape of a NACA 0012 airfoil to match the shape of the struts on the contraction cone.

With the exception of the spacers, the contraction cone was fabricated at the Gulfstream Aerospace Corporation in Savannah, Georgia via a rapid protoyping method called 3-D Printing. Since the size of the model exceeded the capability of the 3-D printing machine,

the contraction cone was split into two sections; the first section consists of the tip of the cone with the struts measuring 5.2 inches long while the second section measures 8.4 inches long. The two sections were connected together via 0.25 inch pins fabricated into the aft surface of the first section of the contraction cone. Tabs similar to the design from the engine baseline model were also fabricated into the second section of the contraction cone so that the cone can be secured onto the baseline model. The 3-D printing model with its two split sections are shown in Fig. 2.12 and Fig. 2.13 respectively.

The internal square cavity design is replicated and implemented on the contraction cone similar to the engine baseline models. As observed in Fig. 2.14, there are also two struts measuring 1 inch in diamater connecting the contour surface to the lower two surfaces of the internal square cavity. The struts serve as channels for the attachment of a pair of 0.25 inch set screws to help secure and position the contraction cone as well as the entire test model onto an internal square beam.

2.1.2.2 Aft-Body Diffuser

The second flow component of the test model is the aft-body diffuser located downstream of the contraction cone and the engine baseline model. The primary goal of the diffuser is to diffuse the bypass flow in the annulus as efficiently as possible. The conical aft-body diffuser will not only minimize flow separation but also maximize total-pressure recovery as well. The design of this flow component is based on diffuser design guidelines from Blevins.[21] Blevins states that for a wide range of turbulent flows (Reynolds number, based on inlet flow velocity and inlet diameter, in excess of 5×10^4), the stall characteristics of a diffuser are primarily a function of diffuser geometry. Therefore, based upon a design chart for conical diffusers by Blevins, the aft-body diffuser was designed using an angle of 4.5° extending a total length, N of 44 inches with the diameter of the bypass duct, W at 2.68 inches (The diameter of the bypass duct on one side is 1.34 inches and fixed by the geometry of the engine baseline model). However, the cone does not extend all the way to a vertex point, rather, the tip of the cone was truncated to form a flat circular base of approximately 1.5 inches in diameter. Further details on the design of the aft-body diffuser can be found in Appendix B.

The aft-body diffuser was made out of polyvinyl chloride (PVC) and is shown in Fig. 2.15. A hole was drilled down the center of the cone to accomodate the installation of the 3 inch x 3 inch aluminum tube. The tube will serve as the backbone for the entire test model. To fit the engine baseline model onto the aft-body diffuser, a straight cavity measuring 1.5 inches deep was fabricated at the wide end of the cone. This cavity provides space for the attachment of tabs from the engine baseline model to the diffuser cone. The figure depicting the installation of the 3 inch x 3 inch aluminum tube within the aft-body diffuser as well as the straight cavity is shown in Fig. 2.16.

There are also two sets of one inch square aluminum struts attached through the diffuser cone and onto the aluminum tube; four of them installed at 8.5 inches from the leading edge of the aft-body diffuser and the next set consisting of also 4 struts spaced approximately 18.5 inches from the first set. The distances were chosen to minimize flow disturbances that might propagate upstream into the bypass duct. The method for acquiring the appropriate spacing distances is detailed in Appendix B. The struts were designed to attach to the axisymmetric tunnel and serve as the main structural support to position and secure the entire test model within the wind tunnel. To avoid scratching the inner surface of the axisymmetric tunnel, the tip of the struts were attached with nylon spacers rounded accordingly to the inner curvature of the test section (Fig. 2.17). Finally, the struts were streamlined using styrofoam to reduce the pressure loss as well as the wake propagating downstream into the wind tunnel diffuser (Fig. 2.18).

2.1.3 Model Assembly

The assembly of the contraction cone, engine baseline model with the gearbox fairing and crane beams, as well as the aft-body diffuser into a full test model takes place on the 3 inch x 3 inch aluminum tube measuring 6 feet in length and 1/4 inch in thickness as a support beam to be positioned at the center of all the components. The cantilevered center beam is attached with the struts from the aft-body diffuser described in Section 2.1.2.2 in the wind tunnel test section, and supports the load from all the test components. Hence, with the exception of the aft-body diffuser, a square cavity with support struts was fabricated at the center of each of the contraction cone and engine baseline model sections to hold the

aluminum beam. This is shown in Fig. 2.3. When positioned in the correct orientation, the square cavity forms a diamond shape measuring 3.03 inches on each side. Referring to Fig. 2.19, the square cavity was designed to be off-centered from the axis by 0.03 inches. This allows for the models to be positioned at the centerline of the test section. To minimize the stresses in the cavities when the model is fully assembled and positioned in the wind tunnel facility, the top corner of the cavity was rounded to a radius of 0.375 inches. This is shown in Fig. 2.3. The assembly of the full test model is relatively straight forward since the aluminum beam is "locked" in place at the center of the aft-body diffuser (Fig. 2.16). The step by step assembly process is described in Appendix C with the complete assembly of the test model shown in Fig. C.1.

2.2 Wind Tunnel Design

To drive an experimental bypass flow path in a wind tunnel facility, the full assembly of the test model shown in Fig. C.1 was installed at the center of an axisymmetric tube. This experimental set up uses the inner wall of the axisymmetric tube to represent the inner surface of the nacelle while the full extent of the engine shroud with the blockage components are represented by the test model. The set-up creates an annular passage between the test model surfaces and the inner wall of the axisymmetric tube, also known as the bypass flow path. This configuration simplifies the geometry of the bypass flow path with a reasonably accurate simulation of the bypass flow development.

A subsonic, open-return wind tunnel with a 15 inch x 15 inch test section at the Aerodynamics Research lab at the University of Illinois was modified to drive the bypass flow simulation. The modification involved replacing the 15 inch x 15 inch test section with an axisymmetric test section designed to accomodate the test model. Fig. 2.20a shows a CAD rendering of the existing 15 inch x 15 inch wind tunnel facility while Fig. 2.20b depicts the replacement of the existing test section with an axisymmetric test section. The existing wind tunnel inlet and diffuser and fan system have been retained for the use of the new bypass facility.

2.2.1 Wind Tunnel Components

The complete axisymmetric test section is assembled from various components as shown in Fig. 2.21. The functionality of these components can be divided into three categories:

1. To serve as the test section
2. To rotate the test section
3. To serve as structural support for the test section

The axisymmetric tube sections as well as the square-to-round sections with flanges serve as the test section while the gear bearings, ring gear and stepper motor are responsible for rotating the axisymmetric tube pieces. The rotating test section is described in detail in Section 2.2.1.2. The components serving as the test section, and to rotate the test section, are closely related and a breakdown of these components can be found in an exploded CAD view in Fig. 2.22. The frames with casters are the structural support for the test section. The following sub-sections will be focused on the dicussion of these different components while the process of assembly of all the components into an axisymmetric test section with the installation of the test model will be described in Section 2.2.2.

2.2.1.1 Square-To-Round Sections

To make the transition from the existing wind tunnel to the new test section, a pair of square-to-round sections were needed; one upstream connecting the wind tunnel inlet to the axisymmetric section while the second is located downstream connecting the axisymmetric test section to the existing wind tunnel diffuser. The square end of this component is 15 inches x 15 inches while the round end measures 11.1 inches to match the inner diameter of the axisymmetric sections. This is shown in Fig. 2.21 and Fig. 2.22. The entire piece was designed to be 33 inches long and which sets the contraction angle at 3.38°. This angle was designed based upon the guidelines from Rae & Pope[22] and the 15 inch x 15 inch wind tunnel fully-attached diffuser design by Jacobs.[23]

The entire square-to-round section was made constructed from 14-gage cold rolled steel with square and round flanges welded at both ends to connect to other components of the

wind tunnel facility. Further measurements of the square-to-round section with the round flanges can be found in Fig. H.1 and Fig. H.2 in Appendix H .

2.2.1.2 Axisymmetric Tunnel Sections

As described previously in Section 2.2, the axisymmetric tunnel sections will serve as the test section for the engine test model. These axisymmetric sections were constructed from an aluminum circular tube measuring 12 inches in outer diamater. Honing was performed to improve the inner surface of the sections resulting in a 11.1 inch tube inner diamater.

For ease of assembly and rotation, the aluminum tube was divided into three sections; tunnel sections A, B and a rotating test section C measuring 24 inches, 42 inches and 42 inches in length, respectively. Tunnel section A is connected to the wind tunnel inlet via the first square-to-round section followed by the rotating test section and tunnel section B while while tunnel section B transitions into the wind tunnel diffuser via the second square-to-round section. The set-up can be observed in both Fig. 2.21 and Fig. 2.22. The tunnel sections were then connected to one another using gear bearings and gear housings described in Section 2.2.1.3. This design fixes tunnel sections A and B but provides the test section C with the ability to rotate. The reason for designing a rotating test section comes from the experimental need to map the entire 360° of the bypass flow annulus to understand the flow characteristics in that region. Placing probe devices at multiple circumferential positions on the axisymmetric test section to achieve that goal is not only costly but impractical. Therefore, the idea was to rotate the nacelle wall, which is represented by the axisymmetric test section C, while the inner engine model remains fixed to the rest of the facility. With the placement of a pressure probe on a radial traverse to the rotating test section C, measurements can then be made over the full range of circumferential and radial positions. To ensure that the engine baseline model with blockage components and subsequently the bypass flow path is within the rotating test section for data acquisition purposes, the full test model is attached 13.7 inches aft of the inlet of tunnel section A. This set-up also ensures that the front and aft-flow components are within fixed tunnel sections A and B, respectively (Fig. 2.21). Further information about the design of the axisymmetric tunnel sections can be found in Appendix D.

For data acquisition purposes, two sets of probe holes were located 4.25 inches from each end of the rotating test section C with one set on each end. The location of the set of upstream and downstream probe holes correspond to the bypass inlet and outlet locations, respectively. Each set consists of two probe holes, 3/4 inch in diameter and are drilled through the wall of the test piece 180° circumferentially apart. A flat surface of approximately 1.5 inches squared and 0.003 inches in depth was machined so that a probe plug can be mounted on the test section and into the probe hole. A picture of the probe hole with the machined outer surface is shown in Fig. 2.23. The probe plug is a component in which the pressure probe, secured by an 1/8 inch NPT mounting chuck can be inserted through to position the pressure probe within the bypass annulus for data acquistion. It consists of a rounded-end cylinder attached on a square piece. The rounded-end was machined to match the curvature of the inner diamater of the rotating test section C. A small slot was fabricated on the square section of the probe plug to provide space for the placement of the surface static pressure tap outlet located on the wall of the rotating test section C. Further discussion about this surface static pressure tap will be made in Section 2.3.1.2. Fig. 2.27 shows a picture of the probe plug with a 1/8 inch NPT mounting chuck while detailed dimensions of the probe plug can be found in Fig. H.3 in Appendix H.

A linear traverse was used to move the pressure probe radially into the test section and through the probe plug. This traverse system was attached to the rotating test section using a traverse mount. The traverse mount is a 3 inch by 5 inch plate with three holes measuring 5/16 inches drilled along the center axis of the plate for the attachment to the rotating test section. The traverse mount was first positioned on the curved surface of rotating test section via its "mounting legs" angled at 12°. It is then secured on the rotating test section through mating holes located 7 inches from the end of the axisymmetric piece. The linear traverse was positioned on the traverse mount through two 1/4-20 inch holes. Drawings of the traverse mount can be found in Fig. H.4 in Appendix H while details about the linear traverse can be found in Appendix I.

2.2.1.3 Gear Bearings

To rotate the test section, gear bearings were designed to fit on the ends of all the axisymmetric tunnel pieces. These bearings are comprised of two separate components; the fixed gear bearing and the gear housing. The fixed gear bearing is a ring-shaped component with an outer diameter of 14.195 inches designed to be attached to the end of tunnel sections A and B, respectively. Similarly, the gear housing is also a ring-shaped component, albeit with a cavity to serve as the insert for the fixed gear bearing. The gear housings are attached to both ends of the rotating test section C. The idea is to first mount the fixed gear bearing and gear housings to their respective axisymmetric sections before inserting the fixed gear bearing into the cavity of the gear housing. Since tunnel sections A and B are connected to the wind tunnel inlet and diffuser, respectively, the test section is able to freely rotate. At the same time, the inner surface of all the axisymmetric pieces is smoothly transitioned, therefore maintaining an circular axisymmetric profile within the test section to serve as the engine nacelle inner surface. An O-ring was fitted on the fixed gear bearing to prevent flow leakage on the rotating surfaces.

Both the fixed gear bearing and gear housing were fabricated out of Nylon. Dimensions of the gear bearing and gear housing is detailed in Appendix E. The two gear housings fitted on both ends of the rotating test section were named gear housing A and gear housing B, respectively. The reason for distinguishing the components from one another is because gear housing A contains screw holes for the addition of a ring gear. The ring gear is responsible for transmitting the torque provided by a stepper motor to the gear bearings. The ring gear is further desribed in Section 2.2.1.4.

2.2.1.4 Ring Gear

As mentioned in Section 2.2.1.3, the ring gear transmits the torque provided by a geared stepper motor to the gear housing in order to rotate the test section. The ring gear selected for this purpose is a Quality Transmission Components model KSSR2-200 ring gear with an inner diameter of 13.93 inches, outer diameter of 15.9 inches and a face width of 0.78 inches. It consists of 200 standard full depth teeth with a pressure angle of 20° and the entire ring

gear is made of S45c steel with black oxide surface treatment for corrision protection. To fully secure the ring gear on gear housing A to maximize the transmitted torque, 16 screw holes spaced circumferentially apart by 22.5° were drilled on the surface of the ring gear for a tight fit to the circular protruding section of gear housing A.

2.2.1.5 Gear Stepper Motor with Controller

Since the rotation of the test section must be controlled in a precise manner for an accurate circumferential mapping of the flow within the bypass annulus, a stepper motor was chosen to provide the necessary torque to rotate the test sections. The selected motor is an Anaheim Automation 34YSG series gear stepper motor. This device has a step angle of 1.8° powered by an actual gear ratio of 4.985:1 to generate a maximum torque of 3500oz-in. The 8 lead wires from the motor was then connected to an Anaheim Automation Programmable Controller model DPY50601 via a bipolar parellel arrangement. The controller can be controlled from a data acquisition computer with a RS-232 cable using the LabVIEW software. Further information about the control of the motor with LabVIEW can be found in Section 2.3.3. To effectively rotate the test section, the motor was set to rotate with an acceleration within the range of 600-800 steps/sec^2, and a base and maximum speed of 200 steps/sec.

A spur gear from Quality Transmission Components model MSGB2-35 was attached to the shaft of the gear stepper motor. The teeth from this spur gear is meshed with the teeth from the ring gear attached to gear housing A to form a link of torque tranmission from the stepper motor. The spur gear has an outer diameter of 2.91 inches and face diameter of 0.28 inches. It consists of 35 standard full depth teeth with a 20° pressure angle and the entire spur gear is made of SCM415 steel without any surface treatment. Since the bore diameter of the spur gear does not match the shaft diameter of the gear stepper motor, an aluminum key was fabricated to lock the spur gear in place on the motor shaft. The entire gear motor with the attached spur gear and aluminum key was positioned on a cross beam via a base plate and motor mount plate, while the cross beam will be in turn attached to the angle supports described in Section 2.2.1.6. The role of the base plate and motor mount plate is to assist in securing the gear stepper motor on the cross beam. Fig. 2.28 shows a

picture of the motor full assembly while Fig. H.5 in Appendix H shows the schematic of the assembly components.

2.2.1.6 Frames with Casters

The assembly of the square-to-round pieces with the axisymmetric test sections has to be structurally supported. Therefore, referring back to Fig. 2.21, three frames with angled supports were designed to hold the axisymmetric test section pieces in place with the rest of the wind tunnel facility. The three frames were all fitted with casters and hold each of the axisymmetric pieces, tunnel sections A, B and the rotating test section C independently as well as together as an assembly. The advantage of having the three sections sit on three seperate frames with casters is that the assembly and disassembly process for the entire bypass facility is simplified. The design of the frames with casters is detailed in Appendix F.

2.2.1.7 Existing Wind Tunnel Components

The wind tunnel inlet, diffuser and fan system used for this experimental simulation were from the existing 15 inch by 15 inch wind tunnel facility (Fig. 2.20a). These components will be briefy described in this section. Additional details about the components can be found in Jacobs.[23]

The wind tunnel inlet is composed of an inlet contraction section and an inlet settling section extension. The length of the entire wind tunnel inlet is approximately 86 inches with a contraction from a 80 inches by 80 inches square section to a 15 inches by 15 inches square section to form a contraction ratio of approximately 27. Within the inlet settling section extension is a honeycomb flow straigthener sandwiched between two turbulence reduction screens. An additional three turbulence reduction screens were located within the inlet. The honeycomb flow straightener consists of hexagonal cells approximately 1/4 inch in diameter and 4 inches thick while the turbulence screens were 24-mesh screens with a porosity of 0.67, spaced 3.25 inches apart. The inlet contraction section was fitted with casters in a tricycle configuration for the ease of assembly and disassembly. Eight surface static pressure taps were also installed on the inlet contraction section; four installed on each side of the wall

just aft of the inlet settling section extension and another four also on each side of the wall right before the 15 inches by 15 inches square section. The measurements from each set of these surface static pressure taps were averaged by connecting the four taps together using copper tubing for the determination of freestream conditions as well as dynamic pressure conditions at the bypass inlet using area ratios. Section 2.4 discusses the implentations of the wind tunnel inlet surface static pressure measurements for various pressure calculations.

The diffuser section of the wind tunnel consists of two sections, each 10 feet in length and was manufactured by Fox Valley Metal Tech. Similar to the square-to-round pieces discussed in Section 2.2.1.1, the two sections of the diffuser were also designed to diffuse from a square to a round end with a fan attached to the round end section of the diffuser. Although Rae & Pope[22] noted that a maximum diffusive angle of 7° (Full Angle) is desired to prevent boundary-layer flow seperation, a conservative diffusive angle was chosen for the design of the diffuser. This is because the diffuser area ratio was large at approximately eight to one, hence the chances of boundary-layer flow seperation occuring within the diffuser is high. Therefore, combined with factors such as limitations in facility space, the diffusive angle was set at approximately 3.7°.[23]

The fan used for the operation of the wind tunnel facility is a Joy Series axivane single-stage fan model 48-26-1750 capable of moving 63,000 CFM of air at 1750 rpm. It is 48 inches in diameter fitted with 16 blades and 13 vanes. The fan is powered by a General Electric AC electric motor model 5K405YK246 with a basic horsepower of 100 and controlled using an Eaton variable frequency AC drive (VFD). This means that the frequency of the electricty supplied to the electric motor can be controlled so that the RPM can be varied. The Eaton variable frequency drive is controlled using a VFD controller equipped with an on/off switch, LCD fan RPM display, fan status LEDs, RS-232 Interface, a potentiometer for the adjustment of fan RPM as well as an emergency shut-off switch. The VFD controller can also be accessed remotely via ANSI C commands through the RS-232 Interface using the LabWINDOWS software.

2.2.2 Bypass Facility Assembly

Once all of the wind tunnel components are assembled, the design of the facility does not provide an access area for the installation of the test model within the axisymmetric test sections. Therefore, the assembly of both the test model and the wind tunnel components is coupled and performed concurrently. The assembly process was simplified by permanently attaching the round flange and fixed gear bearing to both ends of tunnel section A and B while gear housing A and B with the ring gear were secured on the rotating test section C. Angled supports with either support pads or rollers were also installed on the frames. The sequence for the assembly process begins from the square-to-round piece at the downstream section and includes an alignment process for the three axisymmetric pieces. The step by step assembly process with a series of pictures highlighting the main assembly steps is detailed in Appendix G.

2.3 Data Acquisition

This section describes the methods and apparatus involved in acquiring flow data within the bypass annulus. Probes, taps and systems for obtaining the pressure measurements will be discussed as well as surface flow visualization methods. Finally, Section 2.3.3 will provide details about how all the data acquisition apparatus and methods are synchronized to create an automated system to map the flow for the entire bypass annulus.

2.3.1 Pressure Measurement System

2.3.1.1 Pressure Probes

The pressure probes used to obtain pressure measurements within the bypass annulus upstream and downstream section include a standard pitot-static probe and a total pressure probe. The pitot-static probe was fabricated by United Sensor Corporation and is 12 inches long with a tip length of 1.75 inches and 1/8 inches in diameter. Additional details and measurements of the pitot-static probe can be found in Fig. 2.25. In general, the pitot-static probe is a satisfatory device for the measurement of total and static pressure at a

fixed location in either the bypass annulus or an empty axisymmetric tunnel.

However, there are two disadvantages of using the pitot-static probe to map the bypass annulus flow in various radial and circumferential directions. First, the pitot-static probe contains a goose-neck design to connect the stem to the tip of the probe. The goose-neck design prevents the probe from being traversed to the inner wall of the axisymmetric test section. This means that the boundary layers near the bypass annulus nacelle wall will not be mapped. Secondly, the flow at the downstream section and behind the gearbox fairing is predicted to be separated. Using the pitot-static probe to acquire total pressure measurements at this region is undesirable. This is beacause the tip of the pitot-static probe which is also the location of the total pressure port is rounded. Therefore, the total pressure port will not be able to fully capture the separated flow approaching the tip at higher angles.

To help correct for the two issues concerning the usage of a pitot-static probe to map the bypass annulus flow, a modified total pressure probe manufactured by United Sensor Corporation was used. Instead of a goose-neck design, the stem of the total pressure probe was welded to the tip by a 90° miter joint. This allows the total pressure probe to be traversed next to the axisymmetric tunnel wall as well as the wall of the model. Therefore, the total pressure profile of the flow within the annulus can be mapped from the inner to the outer wall. To accomodate for the mapping of flow with higher flow angles, the tip of the total pressure probe was chamfered. The total pressure tube within the probe was then expanded at 30° to the extent of the chamfered tip. The diameter of the probe was also reduced to 1/16th of an inch to minimize flow disturbances propagating downstream due to the presence of the probe. For structural support purposes, the probe was reinforced to 1/8th of an inch at the center section of the probe stem. Detailed measurements for the total pressure probe can be found in Fig. 2.26.

2.3.1.2 Surface Static Taps

Although the modified total pressure probe is an excellent device to acquire total pressure data within the bypass annulus, it does not have the capability to acquire static pressures. Therefore, a surface static tap was drilled on the rotating test section at both the upstream

and downstream test locations. Precisely, the placement of the surface static tap corresponds to the tip location of the total pressure probe once the probe is mounted through the probe hole and within the bypass annulus. This is to ensure that the measurement of the total pressure and static pressure are acquired on the same plane. It is assumed the static pressure measurements across the annulus gap will be reasonably represented by the surface static measurement at the wall.

However, the position of the surface static tap at the upstream section of the rotating test section is obstructed by the rollers. To correct for this problem, a channel was drilled sideways from the inner surface of the probe hole until it meets the surface static tap. Next, a second tap positioned out of the way from the rollers was drilled from the outer surface of the test section vertically until it crosses path with the angled channel. The second tap is referred to as the surface static tap outlet while the surface static tap corresponding to the tip location of the total pressure probe is called surface static tap inlet (Fig. 2.23). The surface static tap inlet and the sideway probe hole was covered with epoxy to form a static pressure channel from the inlet tap to the outlet tap, respectively. The schematic showing the set-up of this pressure tap is shown in Fig. 2.24.

In addition to the two surface static taps at the upstream and downstream probe hole locations of the test section, 35 surface static taps spaced 1 inches apart from each other were placed along the axis of the rotating test section (Fig. 2.29). By rotating the test section in a circumferential manner, the surface static pressure of the inner nacelle wall can be fully mapped. Similar to the surface static tap inlet and oulets, the 35 surface static taps are fitted with a 0.042 inch alloy tubes before being connected to the Pressure Systems Inc. (PSI) pressure acquisition system (Section 2.3.1.3) using either vinyl or urethane pneumatic tubes. As described in Section 2.2.1.7, there are also two pairs of surface static taps located on the wind tunnel inlet. These surface static pressure measurements are used for the determination of freestream conditions as well as the dynamic pressure at the bypass inlet, referred to Q_{inlet}, respectively. This parameter is described in Section 2.4.

2.3.1.3 PSI system

The pressure from the probe devices and the static taps were measured using a Pressure Systems Inc. model PSI 8400 pressure data acquisition system consisting of a high- speed pressure scanning unit connected to various electronicially scanned pressure (ESP) modules. The PSI 8400 system is shown in Fig. 2.30. Each of the ESP modules contain various ports for different purposes; 32 ports for pressure measurements, 3 ports for calibration and either 1 or 2 ports to serve as the reference pressure (Fig. 2.31). The ESP modules currently available for pressure measurements at the Aerodynamics Research Lab consists of 0.35 psid, 1 psid and 5 psid modules. For the purpose of this experiment, all pressure measurements were sampled using 1 psid ESP modules. All the pressure measurements were referenced to atmospheric pressure obtained through a seperate barometric pressure transducer located in the control room in the Aerodynamics Research Lab and connected to the data acquisition computer via a National Instruments Corporation (NI) Analog to Digital (A/D) board.

Since the accuracy of the ESP modules will be affected by temperature fluctuations, the modules were calibrated before each run. The calibration procedure involves the three calibration ports on each of the ESP modules, called C1, C2 and Cal ports, respectively. The C1 and C2 ports are connected to a nitrogen tank using pneumatic tubes while the Cal port is connected to a vacuum pump. The process of calibration begins when the PSI 8400 system scanning unit switches the ESP modules from a run mode to calibration mode by supplying a burst nitrogen at 100 psi to both the C1 and C2 ports respectively. Next, the Pressure Calibration Unit (PCU) of the PSI 8400 system calibrates the 1 psid ESP modules used for this experiment through a vacuum pump. The ESP modules are then switched back to the run mode through the C1 and C2 ports again. The process of calibration results in three calibration coefficients for each port on the ESP modules. These calibration coefficients convert the voltages for each of the 32 pressure measurement ports to pressure units. The entire process of calibration to produce the calibration coeffients was automated through a computer program written in LabWINDOWS. A schematic of the pneumatic connections between the PSI 8400 scanning and calibration units to the respective ESP

modules for calibration and pressure acquisition purposes is shown in Fig. 2.32.

2.3.2 Surface Fluorescent Oil Flow Visualization

To provide additional flow diagnostics on the test model, the technique of surface fluorescent oil flow visualization was employed. This technique creates a visual representation of flow features such as separation and recirculation as well as flow transition on the test model. This method requires the test model to be first coated with a lubricant such as motor oil before a mixture of mineral oil and fluorescent dye is sprayed on the surface of the model. Once the wind tunnel is turned on, the forces exerted by the airflow will shear the fluorescent dye on the surface of the model. The streamlines of the flow is characterized by the path of the dye and is visible with flourescence from ultraviolet light illumination. By examining the shear stress levels of the dye on the surface of the model, flow characteristics such as transition and turbulence can be further identified.[24] For example, turbulent flows exert higher shear stresss than laminar flows. Therefore, dye within a turbulent region will move further than a dye subjected to laminar flow. At regions of flow separation, the shear stress from the flow is zero. Hence, the dye remains as spray specks.

The preparation of the model for the surface fluorescent oil flow visualization involves removing the wind tunnel inlet, tunnel section A and the rotating test section C to expose the cantilevered test model. The region of interest for the flow visualization was first thoroughly cleaned before a layer of black contact paper was applied on the surface of the model. The purpose of applying the contact paper on the model is to protect the surface of the model as well as providing a smooth surface for flow visualization. Scales were then labeled on strips of yellow electrical tape and placed on the edges of the contact paper. Next, a thin coat of motor oil was gently applied on the contact paper before a mixture of about one ounce of mineral oil and Kent-Moore 28431-1 flourescent dye was sprayed on top of the layer of motor oil. The spray was applied at approximately 30 psi. The rotating test section C, tunnel section A as well as the wind tunnel inlet was then reattached as quickly as possible to prevent the dye from flowing to the underside of the test model. The tunnel was then ramped to the desired speed for approximately 5 minutes before the tunnel sections are again removed for the inspection of the flow visualization. Under the illumination of

black lights placed around the test model, photos of the flow visualization were obtained using a Nikon D100 Digital SLR camera using various exposure times and F-stops.

2.3.3 Data Acquisition with LabVIEW

The data acquisition process for the bypass annulus involves synchronizing all the experimental apparatus to create an automated system for data acquisition. A schematic showing the setup of the data acquisition system is shown in Fig. 2.33. As shown in that figure, all the experimental instruments were connected to a data acquisition computer. With the exception of the wind tunnel fan and PSI system, a computer program written in LabVIEW was used to synchronize and control the instruments. Both the wind tunnel fan and PSI system were controlled using separate programs written in LabWINDOWS.

The procedure for obtaining a set of experimental measurements starts with the rotation of the test section C to the home configuration for the taring of the inclinometer. The home configuration is the position where the linear traverse and probe are at the 12 O'clock position. This position is further defined as 0° in the experiment. Further information about the inclinometer and linear traverse can be found in Appendix I. Next, the user will provide tunnel rotation and pressure probe traversing information such as the extent of circumferential and radial steps in degrees and millimeters to the LabVIEW program, respectively. The program provides the user with two options for traversing the pressure probe. The first option calls for the probe to traverse a certain amount of steps of equal distances within the bypass annulus. This amount of steps is determined by the user. The second option allows the user to provide the program with a text file containing the exact positions in which the probe will traverse to. Therefore, with this option, the user has the ability to acquire dense measurements at a region of interest such as areas close to the boundary layer.

After setting the circumferential and radial steps in the LabVIEW program, the tunnel fan was ramped to maximum speed. The data acquisition process begins through an automated process controlled by the computer program. The program first acquires the pressure measurements from the 35 axial surface static taps before the pressure probe traverses the bypass annulus from the test section inner wall to the test model wall. Simulatenously, the

static pressure and total pressure measurements from the static taps and pressure probe at that particular circumferential and radial position, respectively, were mapped in two 2-D color contour figures. The test section then rotates to the next circumferential step and the pressure measurement process with the static taps and pressure probe was repeated until the test section was rotated to the full extent of 360°. The 2-D color contour feature retains the color mapping from previous pressure measurements to provide the user with a general picture of the entire flow-field as the test section rotates through 360°.

2.3.4 Test Matrix

All the combinations of experiments performed with different model configurations are summarized in a test matrix shown in Table 2.1. The upstream and downstream locations in the column of measurement location column refer to the positions of bypass inlet and exit, respectively.

Table 2.1: Test Matrix

Test Configuration	**Measurement Location**	**Rotation Step (deg)**	**Angular Step (steps)**	**Traversed Distance (mm)**	**Probe Used**
Empty Tunnel	Upstream	5	21	130	Pitot-Static
Empty Tunnel	Downstream	5	21	130	Pitot-Static
Empty Tunnel	Upstream	5	22	139.7	Total
Empty Tunnel	Downstream	5	22	139.7	Total
Engine Baseline Model	Upstream	5	27	31	Total
Engine Baseline Model	Downstream	5	27	31	Total
Engine Baseline Model with Gearbox Close-Out Fairing Removed	Downstream	5	25	32	Total
Engine Baseline Model with Gearbox Fairing	Upstream	5	27	32	Total
Engine Baseline Model with Gearbox Fairing	Downstream	5	27	32	Total
Engine Baseline Model With Gearbox Fairing And Crane Beams	Downstream	5	25	32	Total
Engine Baseline Model with Gearbox Close-Out Fairing Removed	Surface Fluorescent Oil Flow Visualization				
Engine Baseline Model with Gearbox Fairing	Surface Fluorescent Oil Flow Visualization				

2.4 Flow Variables and Method of Nondimensionalization

Assuming that the flow is inviscid and incompressible, the pressures and velocity along a streamline can be related using Bernoulli's equation stated in Eq. 2.1.

$$P + \frac{1}{2}\rho U^2 = constant \tag{2.1}$$

Therefore, the velocity of the fluid at a point of measurement can be written as

$$U = \sqrt{\frac{2\left(P_t - P_s\right)}{\rho}} \tag{2.2}$$

Where $P_t - P_s$ is equal to the dynamic pressure at a point of measurement, Q. Hence the Mach number can be defined as

$$M = \frac{U}{\sqrt{\gamma RT}} \tag{2.3}$$

Where γ is the specific heat for air at 1.4, and R is the gas constant for air at $1716\frac{ft-lb}{slug-R}$. In all of the wind tunnel measurements, the temperature is assumed to be equal to the ambient temperature, T_{amb}.

All the pressure survey results are nondimensionalized by either Q_{tunnel} or Q_{inlet}. These parameters are reference dynamic pressures computed at the start of the 11.1 inch axisymmetric tunnel and at the start of the bypass annular region, respectively. To calculate these values, Bernoulli's equation and the equation for mass conservation were used.

For the case of an empty tunnel, the surface static pressure at the wind tunnel inlet and in the rotating test section, denoted as P_{s1} and P_s, respectively, were measured using pressure transducers. Nomenclature for the different pressure measurements with their measurement locations can be found in Fig. 2.34. Bernoulli's equation in Eq. 2.1 was used to correlate the pressures and velocities at these two sections, yielding an equation

$$P_{s1} + \frac{1}{2}\rho {U_1}^2 = P_s + \frac{1}{2}\rho {U_3}^2 \tag{2.4}$$

Where the subscripts 1 and 3 refers to the upstream section of the wind tunnel inlet and at

the start of the empty axisymmetric section, respectively. Since surface static taps were not installed at the start of the empty axisymmetric test section, the surface static measurement was instead taken at the upstream measurement station in the rotating test section. The surface static measurement at the upstream measurement station in the empty rotating test section is assumed to be representative of the surface static pressure measurement at the start of the empty axisymmetric test section. Therefore, as prescribed in the right hand side of the Bernoulli's equation in Eq. 2.4, the surface static pressure measurement in the rotating test section P_s is correlated with the velocity at the start of the axisymmetric tunnel section, U_3 or U_{tunnel}.

Using mass conservation and assuming constant density, velocites at location 1 and 3 were further related by

$$U_1 A_1 = U_3 A_3 \tag{2.5}$$

By substituting Eq. 2.5 into Eq. 2.4, the dynamic pressure at the start of the empty tunnel, also referenced as Q_{tunnel} is derived as Eq. 2.6.

$$Q_{tunnel} = \frac{P_{s1} - P_s}{1 - \left(\frac{A_3}{A_1}\right)^2} \tag{2.6}$$

Similarly, once the test model is installed within the bypass facility, the reference dynamic pressure for the test model cases, Q_{inlet} can be calculated in the same manner as Q_{tunnel}. The surface static pressures at the upstream and downstream locations of the wind tunnel inlet, P_{s1} and P_{s2} were measured using the pressure transducers and correlated using Bernoulli's equation. Using mass conservation, the dynamic pressure at the wind tunnel inlet downstream location can be calculated. As shown in Fig. 2.34, this location is denoted as subscript 2. The velocity at the wind tunnel inlet downstream section is then determined using the calculated dynamic pressure with the upstream and downstream area ratios. This yields an equation for Q_{inlet} shown in Eq. 2.7.

$$Q_{inlet} = \frac{1}{2}\rho {U_4}^2 \quad or \quad Q_{inlet} = \frac{1}{2}\rho \left[U_3 \left(\frac{A_3}{A_4}\right)\right]^2 \tag{2.7}$$

Therefore, the parameters Q_{tunnel} and Q_{inlet}, can be used to nondimensionalize changes in total pressure and surface static pressure measurements for an empty tunnel or for a particular test model configuration. For example, the loss in total pressure can be nondimensionalized as below

$$\Delta P_{t,non-dim} = \frac{P_t - P_{amb}}{Q_{tunnel}} \tag{2.8}$$

Since the total pressure loss through the flow-straightening and turbulence-reduction screens in the wind tunnel inlet is small due to the large contraction ratio, the ambient pressure P_{amb} is approximately the total pressure in the wind tunnel freestream. Therefore, the nondimensionalized changes in total pressure $\Delta P_{t,non-dim}$ describes the total pressure loss within the tunnel from the freestream total pressure with respect to the dynamic pressure of the empty tunnel, Q_{tunnel}. Hence, $\Delta P_{t,non-dim}$ is essentially a pressure coefficient using a measured and referenced total pressure. The nondimensionalized total pressure for a test model configuration is prescribed in a similar fashion as Eq. 2.8. However, since a test model configuration is installed within the axisymmetric tunnel sections, the difference between a total pressure measurement with the freestream total pressure is nondimensionalized with the parameter Q_{inlet}. This is shown in Eq. 2.9.

$$\Delta P_{t,non-dim} = \frac{P_t - P_{amb}}{Q_{inlet}} \tag{2.9}$$

A surface static pressure coefficient C_p is defined for the axial surface static pressure measurements located on the rotating test section. C_p is described as the difference between a surface static pressure measurement and the surface static pressure measurement from the first surface tap with respect to dynamic pressure at the bypass inlet (Eq. 2.10). The first surface static tap is located approximately in the same plane as the upstream measurement location and denoted as $P_{s,tap1}$. In this case, the measurement of the first surface static tap is used as an approximation to the static pressure in the wind tunnel freestream. Since Q_{inlet} was not acquired during the data acquisition for the 35 axial surface static pressure taps, the value for Q_{inlet} measured during the probe measurement at the tunnel wall was used to calculate the surface static pressure coefficients C_p. This is because the acquisition

of radial pressures at the tunnel wall occurs immediately after the measurement of the axial surface static pressures. The value for the bypass inlet dynamic pressure acquired at this instance is denoted as $Q_{inlet}\prime$.

$$C_p = \frac{P_s - P_{s,tap1}}{Q_{inlet}\prime} \tag{2.10}$$

To quantify the behavior of the measured dynamic pressure for a test model configuration with respect to the dynamic pressure calculated at the bypass inlet, an equation for a nondimensionalized dynamic presure, $Q_{non-dim}$ is described as Eq. 2.11. Therefore, $Q_{non-dim}$ with value greater and less than one represents an increase and decrease in dynamic pressure from Q_{inlet}, respectively.

$$Q_{non-dim} = \frac{Q}{Q_{inlet}} \tag{2.11}$$

To further quantify the flow condition of a certain experimental configuration, the nondimensionalized dynamic pressures are compared to other flow variables and written in percentage form. This is denoted as the flow variable $\Delta Q_{non-dim}(\%)$. For an empty tunnel, this parameter is defined as Eq. 2.12.

$$\Delta Q_{non-dim}(\%) = \frac{Q_{non-dim} - Q_{core,avg,non-dim}}{Q_{core,avg,non-dim}} \tag{2.12}$$

Where the parameter $Q_{core,avg,non-dim}$ refers to the average value for all nondimensionalized dynamic pressures at the center of the empty tunnel excluding boundary-layer regions. This is mathematically defined as Eq. 2.13.

$$Q_{core,avg,non-dim} = \left(\sum_{i=1}^{N} Q_{i,non-dim,core} \right) /N \tag{2.13}$$

Where N refers to the number of measurements acquired at the core of the empty tunnel. Therefore, the defintion of $\Delta Q_{non-dim}(\%)$ for an empty tunnel stated in Eq. 2.12 describes the difference in percentage form of a point measurement of nondimensionalized dynamic pressure within an empty tunnel to the average value of all the nondimensionalized dynamic pressures at the core of the tunnel .

For a test configuration of an engine baseline model with an attached blockage component, $\Delta Q_{non-dim}(\%)$ is described mathematically as

$$\Delta Q_{non-dim}(\%) = \frac{Q_{non-dim,model} - Q_{non-dim,baseline}}{Q_{non-dim,baseline}} \tag{2.14}$$

$$Q_{non-dim,model} = \frac{Q_{model}}{Q_{inlet,model}} \qquad Q_{non-dim,baseline} = \frac{Q_{baseline}}{Q_{inlet,baseline}} \tag{2.15}$$

Where the subscripts *baseline* and *model* refer to the test configuration of engine baseline model and engine baseline model with blockage components, respectively. Therefore, $\Delta Q_{non-dim}(\%)$ in this case describes the percentage difference of a point measurement of the nondimensional dynamic pressure within the bypass annulus for a blockage configuration to the nondimensional dynamic pressure for the baseline model configuration. The pressure coefficients and nondimensionalized variables used in the pressure survey results are summarized in Table 2.2.

Table 2.2: Summary of Nondimensionalized Equations for Pressure Survey Results

Test Configuration	$\Delta P_{t,non-dim}$	C_p	$Q_{non-dim}$	$\Delta Q_{non-dim}$ (%)
Empty Tunnel	$\frac{P_T - P_{amb}}{Q_{tunnel}}$	N/A	$\frac{Q}{Q_{tunnel}}$	$\frac{Q_{non-dim} - Q_{core,avg,non-dim}}{Q_{core,avg,non-dim}}$
Engine Baseline Model	$\frac{P_T - P_{amb}}{Q_{inlet}}$	$\frac{P_s - P_{s,tap1}}{Q_{inlet}'}$	$\frac{Q}{Q_{inlet}}$	N/A
All Other Bypass Configurations	$\frac{P_T - P_{amb}}{Q_{inlet}}$	$\frac{P_s - P_{s,tap1}}{Q_{inlet}'}$	$\frac{Q}{Q_{inlet}}$	$\frac{(Q_{non-dim,\ model}) - (Q_{non-dim,\ baseline})}{(Q_{non-dim,\ baseline})}$

2.5 Uncertainty Analysis

This section describes the uncertainty in the experimental measurements that were performed. A procedure for the calculation of the propagation of uncertainties is outlined before a sample calculation of the uncertainties associated with each related variable is presented.

The experimental uncertainty can be contributed by two kinds of errors; bias errors and precision errors. The sum of the bias and precision errors will give the total error. The bias error is a fixed, systematic or constant component of the total error while the precision error is the random component of the total error or referred to as the repeatability error.[25] As described by Jacobs,[23] examples of the bias and precision error include poor calibration of the electronically scanned pressure transducers and quantization effects associated with A/D processes, respectively.

The approach used to calculate the uncertainties associated with this experiment is a general uncertainty analysis. This analysis focuses on determining the propagation of uncertainties in individual variables through a data reduction equation as opposed to examining the details of the bias and precision components.[25] For a general case with a result r as a function of measured experimental variables X_i (Eq. 2.16), the equation for the calculation of the general uncertainty for r is given in Eq. 2.17.

$$r = r(X_1, X_2, ...X_n) \tag{2.16}$$

$$W_r = \sqrt{\left(\frac{\partial r}{\partial X_1} W_{X_1}\right)^2 + \left(\frac{\partial r}{\partial X_2} W_{X_2}\right)^2 + \left(\frac{\partial r}{\partial X_3} W_{X_3}\right)^2} \tag{2.17}$$

Where W_{X_i} are the uncertainties in the measured experimental variables X_i. The assumption for this method of uncertainty analysis is that Eq. 2.16 be a continuous function with continuous derivatives. The measured experimental variables X_i are also assumed to be independent from one another.

2.5.1 Uncertainty of Variables Describing Flow Conditions

To compute the uncertainty of the variables through data reduction equations to describe the flow conditions, certain factory uncertainties were used. For example, the barometric pressure transducer used for the measurement of atmospheric pressure P_{amb} had an uncertainty of 0.008 psi while the thermocouple used for the measurement of ambient temperature had an uncertainty of 1°F. In addition, the uncertainties in measurements from the electronically scanned pressure transducers are summarized in Table 2.3. The 1 psid pressure transducers were the only transducers used for this experiment.

Table 2.3: ESP Module Uncertainties as Estimated by the Manufacturuer

Module	Module Uncertainty	Calibration Uncertainty	Total Uncertainty
5 psid	±0.0035 psid	±0.0010 psid	±0.0036 psid
1 psid	±0.0010 psid	±0.0010 psid	±0.0014 psid
0.35 psid	±0.00035 psid	±0.0002 psid	±0.0004 psid

2.5.1.1 Density

The density ρ refers to the density in either an empty tunnel or bypass annulus at a specific point of measurement. The density was determined using the ideal gas law $\rho = \frac{P_s+P_{amb}}{RT_{amb}}$ where P_s refers to the static pressure at a specific point of measurement referenced to the atmospheric pressure, while R is the gas constant for air at a constant of $1716\frac{ft-lb}{slug-R}$. Hence, the uncertainty for the measurement of density ρ is described in Eq. 2.18.

$$W_\rho = \sqrt{\left(\frac{\partial \rho}{\partial P_s} W_{P_s}\right)^2 + \left(\frac{\partial \rho}{\partial P_{amb}} W_{P_{amb}}\right)^2 + \left(\frac{\partial \rho}{\partial T_{amb}} W_{T_{amb}}\right)^2} \tag{2.18}$$

where

$$\frac{\partial \rho}{\partial P_s} = \frac{1}{RT_{amb}} \tag{2.19}$$

$$\frac{\partial \rho}{\partial T_{amb}} = -\frac{P_s + P_{amb}}{RT_{amb}{}^2} \tag{2.20}$$

$$\frac{\partial \rho}{\partial P_{amb}} = \frac{1}{RT_{amb}} \tag{2.21}$$

2.5.1.2 Dynamic Pressure

The dynamic pressure Q, is a point measurement of dynamic pressure in either an empty tunnel or bypass annulus. This parameter is the difference between the total pressure P_t, and static pressure P_s. Since the total pressure and static pressure are measured by two separate ports on the 1 psid pressure transducer, the uncertainty for Q is stated in Eq. 2.22.

$$W_Q = \sqrt{\left(\frac{\partial Q}{\partial P_t} W_{P_t}\right)^2 + \left(\frac{\partial Q}{\partial P_s} W_{P_s}\right)^2} \tag{2.22}$$

Where

$$\frac{\partial Q}{\partial P_t} = 1 \qquad \frac{\partial Q}{\partial P_s} = -1 \tag{2.23}$$

2.5.1.3 Velocity

The point measurement of velocity in the bypass annulus is based upon incompressible theory using dynamic pressure, Q and is shown in Eq. 2.2 in Section 2.4. The uncertainty in velocity is shown in Eq.2.24.

$$W_U = \sqrt{\left(\frac{\partial U}{\partial Q} W_Q\right)^2 + \left(\frac{\partial U}{\partial \rho} W_\rho\right)^2} \tag{2.24}$$

Where

$$\frac{\partial U}{\partial Q} = \frac{1}{\sqrt{2Q\rho}} \tag{2.25}$$

$$\frac{\partial U}{\partial \rho} = -\frac{\sqrt{Q}}{\sqrt{2\rho^3}} \tag{2.26}$$

2.5.1.4 Mach Number

The uncertainty for Mach Number at point of measurement (Eq. 2.3) is shown in Eq. 2.27. The constants for this equation include the ratio of specific heat for air,γ at 1.4 and the gas constant for air, R at $1716 \frac{ft-lb}{slug-R}$.

$$W_M = \sqrt{\left(\frac{\partial M}{\partial U} W_U\right)^2 + \left(\frac{\partial M}{\partial T_{amb}} W_{T_{amb}}\right)^2} \tag{2.27}$$

Where

$$\frac{\partial M}{\partial U} = \frac{1}{\sqrt{\gamma R T_{amb}}} \tag{2.28}$$

$$\frac{\partial M}{\partial T_{amb}} = -\frac{U}{2\sqrt{\gamma R {T_{amb}}^3}} \tag{2.29}$$

2.5.1.5 Nondimensionalization Parameter, Q_{inlet}

Q_{inlet} is a dynamic pressure computed at the start of the annular region corresponding to the engine inlet splitter and is used for nondimensionalization purposes. Further information about this parameter can be obtained in Section 2.4. Since this parameter is a function of variables such as Q_2 (Dynamic pressure at the downstream section of the wind tunnel inlet) and U_2 (Velocity at the downstream section of the wind tunnel inlet), the uncertainty for Q_2 and U_2 has to be first determined. The uncertainty for Q_2 and U_2 is shown in Eq. 2.30 and Eq. 2.32, respectively.

$$W_{Q_2} = \sqrt{\left(\frac{\partial Q_2}{\partial P_{s,1}} W_{P_{s,1}}\right)^2 + \left(\frac{\partial Q_2}{\partial P_{s,2}} W_{P_{s,2}}\right)^2} \tag{2.30}$$

Where

$$\frac{\partial Q_2}{\partial P_{s,1}} = \frac{1}{1 - \left(\frac{A_2}{A_1}\right)^2} \qquad \frac{\partial Q_2}{\partial P_{s,2}} = -\frac{1}{1 - \left(\frac{A_2}{A_1}\right)^2} \tag{2.31}$$

$$W_{U_2} = \sqrt{\left(\frac{\partial U_2}{\partial Q_2} W_{Q_2}\right)^2 + \left(\frac{\partial U_2}{\partial \rho_2} W_{\rho_2}\right)^2} \tag{2.32}$$

Where

$$\frac{\partial U_2}{\partial Q_2} = \frac{1}{\sqrt{2 Q_2 \rho_2}} \tag{2.33}$$

$$\frac{\partial U_2}{\partial \rho_2} = -\frac{\sqrt{Q_2}}{\sqrt{2 {\rho_2}^3}} \tag{2.34}$$

Therefore, the uncertainty of Q_{inlet} is shown in Eq. 2.35

$$W_{Q_{inlet}} = \sqrt{\left(\frac{\partial Q_{inlet}}{\partial U_2} W_{U_2}\right)^2 + \left(\frac{\partial Q_{inlet}}{\partial \rho_{inlet}} W_{\rho_{inlet}}\right)^2} \tag{2.35}$$

Where

$$\frac{\partial Q_{inlet}}{\partial U_2} = \rho U_2 \left(\frac{A_2}{A_4}\right)^2 \tag{2.36}$$

$$\frac{\partial Q_{inlet}}{\partial \rho_{inlet}} = \frac{{U_2}^2}{2} \left(\frac{A_2}{A_4}\right)^2 \tag{2.37}$$

2.5.1.6 Nondimensionalization Parameter, Q_{tunnel}

Similar to Q_{inlet}, Q_{tunnel} is a dynamic pressure nondimensionalization parameter (Eq. 2.6). However, this parameter is calculated for an empty 11.1 inch axisymmetric tunnel. The uncertainty for this parameter is shown in Eq. 2.38.

$$W_{Q_{tunnel}} = \sqrt{\left(\frac{\partial Q_{tunnel}}{\partial P_{s,1}} W_{P_{s,1}}\right)^2 + \left(\frac{\partial Q_{tunnel}}{\partial P_s} W_{Ps}\right)^2} \tag{2.38}$$

Where

$$\frac{\partial Q_{tunnel}}{\partial P_{s,1}} = \frac{1}{1 - \left(\frac{A_3}{A_1}\right)^2} \qquad \frac{\partial Q_{tunnel}}{\partial P_s} = -\frac{1}{1 - \left(\frac{A_3}{A_1}\right)^2} \tag{2.39}$$

2.5.1.7 Nondimensionalized Variables

Flow variables such as dynamic, total and static pressure are nondimensionalized with either Q_{tunnel} or Q_{inlet}. A summary of the nondimensionalized flow variables for the pressure survey is shown in Table 2.2. The uncertainty for the nondimensionalized total pressure, $\Delta P_{t,non-dim}$ of an empty wind tunnel is shown in Eq. 2.40.

$$W_{\Delta P_{t,non-dim}} = \sqrt{\left(\frac{\partial(\Delta P_{t,non-dim})}{\partial\left(P_t - P_{amb}\right)} W_{P_t - P_{amb}}\right)^2 + \left(\frac{\partial(\Delta P_{t,non-dim})}{\partial\left(Q_{tunnel}\right)} W_{Q_{tunnel}}\right)^2} \tag{2.40}$$

Where

$$\frac{\partial(\Delta P_{t,non-dim})}{\partial\left(P_t - P_{amb}\right)} = \frac{1}{Q_{tunnel}} \qquad \frac{\partial(\Delta P_{t,non-dim})}{\partial\left(Q_{tunnel}\right)} = P_t - P_{amb} \tag{2.41}$$

The uncertainty for the nondimensionalized total pressure for a test model configuration is

$$W_{\Delta P_{t,non-dim}} = \sqrt{\left(\frac{\partial(\Delta P_{t,non-dim})}{\partial\left(P_t - P_{amb}\right)} W_{P_t - P_{amb}}\right)^2 + \left(\frac{\partial(\Delta P_{t,non-dim})}{\partial\left(Q_{inlet}\right)} W_{Q_{inlet}}\right)^2} \tag{2.42}$$

Where

$$\frac{\partial(\Delta P_{t,non-dim})}{\partial\left(P_t - P_{amb}\right)} = \frac{1}{Q_{inlet}} \qquad \frac{\partial(\Delta P_{t,non-dim})}{\partial\left(Q_{inlet}\right)} = P_t - P_{amb} \tag{2.43}$$

The uncertainty for a nondimensionalized dynamic pressure measurement of an empty tunnel is shown in Eq. 2.44.

$$W_{Q_{non-dim}} = \sqrt{\begin{array}{c}\left(\frac{\partial Q_{non-dim}}{\partial P_t} W_{P_t}\right)^2 + \\ \left(\frac{\partial Q_{non-dim}}{\partial P_s} W_{Ps}\right)^2 + \left(\frac{\partial Q_{non-dim}}{\partial Q_{tunnel}} W_{Q_{tunnel}}\right)^2\end{array}} \tag{2.44}$$

Where

$$\frac{\partial Q_{non-dim}}{\partial P_t} = \frac{1}{Q_{tunnel}} \qquad \frac{\partial Q_{non-dim}}{\partial P_s} = -\frac{1}{Q_{tunnel}} \qquad \frac{\partial Q_{non-dim}}{\partial Q_{tunnel}} = P_t - P_s \tag{2.45}$$

The uncertainty for a nondimensionalized dynamic pressure measurement for a test model configuration is

$$W_{Q_{non-dim}} = \sqrt{\begin{array}{c}\left(\frac{\partial Q_{non-dim}}{\partial P_t} W_{P_t}\right)^2 + \\ \left(\frac{\partial Q_{non-dim}}{\partial P_s} W_{Ps}\right)^2 + \left(\frac{\partial Q_{non-dim}}{\partial Q_{inlet}} W_{Q_{inlet}}\right)^2\end{array}} \tag{2.46}$$

Where

$$\frac{\partial Q_{non-dim}}{\partial P_t} = \frac{1}{Q_{inlet}} \qquad \frac{\partial Q_{non-dim}}{\partial P_s} = -\frac{1}{Q_{inlet}} \qquad \frac{\partial Q_{non-dim}}{\partial Q_{inlet}} = P_t - P_s \tag{2.47}$$

The variable C_p is described as the difference between a surface static pressure measure-

ment and the surface static pressure measurement from the first surface tap with respect to dynamic pressure at the bypass inlet (Eq. 2.10). The dynamic pressure at the bypass inlet was acquired during the probe measurements at the tunnel wall and denoted as $Q_{inlet}{}'$. The uncertainty of $Q_{inlet}{}'$ is calculated using a similar expression from Eq. 2.35. Therefore, the uncertainty for C_p is defined as Eq. 2.48.

$$W_{C_p} = \sqrt{\left(\frac{\partial C_p}{\partial P_s} W_{P_s}\right)^2 + \left(\frac{\partial C_p}{\partial P_{s,tap1}} W_{P_{s,tap1}}\right)^2 + \left(\frac{\partial C_p}{\partial Q_{inlet}{}'} W_{Q_{inlet}{}'}\right)^2} \tag{2.48}$$

Where

$$\frac{\partial C_p}{\partial P_s} = \frac{1}{Q_{inlet}{}'} \qquad \frac{\partial C_p}{\partial P_{s,tap1}} = -\frac{1}{Q_{inlet}{}'} \qquad \frac{\partial C_p}{\partial Q_{inlet}{}'} = P_s - P_{s,tap1} \tag{2.49}$$

2.5.1.8 Nondimensionalized Dynamic Pressure (Percentage)

The nondimensionalized dynamic pressure is further expressed in percentage differences from other flow variables. The equations for a nondimensionalized dynamic pressure in percentage form for an empty wind tunnel and with a model configuration are found in Table 2.2. Their uncertainties are listed in Eq. 2.52 and Eq. 2.55, respectively.

For the uncertainty in nondimensionalized dynamic pressure in percentage form for an empty wind tunnel, the equation contains a variable referred to as $Q_{core,avg,non-dim}$. This variable is defined in Eq. 2.13 with its uncertainty stated in Eq 2.50.

$$W_{Q_{core,avg,non-dim}} = \sqrt{\begin{array}{c}\left(\frac{\partial Q_{core,avg,non-dim}}{\partial Q_1} W_{Q_1}\right)^2 + \\ \left(\frac{\partial Q_{core,avg,non-dim}}{\partial Q_2} W_{Q_2}\right)^2 + ... + \left(\frac{\partial Q_{core,avg,non-dim}}{\partial Q_N} W_{Q_N}\right)^2\end{array}} \tag{2.50}$$

Hence,

$$W_{Q_{core,avg,non-dim}} = \frac{\sqrt{N}}{N} W_Q \tag{2.51}$$

Where N refers to the number of measurements acquired at the core of the empty wind tunnel.

Therefore, the uncertainty for the nondimensionalized dynamic pressure in percentage form for an empty wind tunnel is

$$W_{\Delta Q_{non-dim}(\%)} = \sqrt{\left(\frac{\partial(\Delta Q_{non-dim}(\%))}{\partial Q_{core,avg,non-dim}} W_{Q_{core,avg,non-dim}}\right)^2 + \left(\frac{\partial(\Delta Q_{non-dim}(\%))}{\partial Q_{non-dim}} W_{Q_{non-dim}}\right)^2} \tag{2.52}$$

Where

$$\frac{\partial(\Delta Q_{non-dim}(\%))}{\partial Q_{non-dim}} = \frac{1}{Q_{core,avg,non-dim}} \tag{2.53}$$

$$\frac{\partial(\Delta Q_{non-dim}(\%))}{\partial Q_{core,avg,non-dim}} = -\frac{Q_{non-dim}}{{Q_{core,avg,non-dim}}^2} \tag{2.54}$$

The uncertainty for the nondimensionalized dynamic pressure in percentage form for a model configuration is

$$W_{\Delta Q_{non-dim}(\%)} = \sqrt{\left(\frac{\partial(\Delta Q_{non-dim}(\%))}{\partial Q_{non-dim,model}} W_{Q_{non-dim,model}}\right)^2 + \left(\frac{\partial(\Delta Q_{non-dim}(\%))}{\partial Q_{non-dim,baseline}} W_{Qnon-dim,baseline}\right)^2} \tag{2.55}$$

Where

$$\frac{\partial(\Delta Q_{non-dim}(\%))}{\partial Q_{non-dim,model}} = \frac{1}{Q_{non-dim,baseline}} \tag{2.56}$$

$$\frac{\partial(\Delta Q_{non-dim}(\%))}{\partial Q_{non-dim,baseline}} = -\frac{Q_{non-dim,model}}{{Q_{non-dim,baseline}}^2} \tag{2.57}$$

The variables of $Q_{non-dim,model}$ and $Q_{non-dim,baseline}$ have uncertainties similar to the definition in Section 2.5.1.7.

2.5.2 Sample Uncertainties

The following tables provide a sample of the uncertainties for the numerous flow variables in the experiment calculated using the equations described from Section 2.5.1.1 to Section 2.5.1.8.

Table 2.4: Sample Uncertainties of Flow Variables for a Test Configuration of Baseline Model with Gearbox Fairing at 0° and at R^*=1, Upstream Condition

Parameter	Reference Value	Absolute Uncertainty	Relative Uncertainty (%)
ρ	2.25x10^{-3} $\frac{slug}{ft^3}$	± 1.38x10^{-5} $\frac{slug}{ft^3}$	±0.61
Q	0.2223 psi	±0.0019 in.	±0.89
U	168.44 $\frac{ft}{s}$	± 0.5168 $\frac{ft}{s}$	±0.30
M	0.2759	± 0.0664	±0.24
Q_{inlet}	0.2742 psi	± 0.0042 psi	±1.55
$Q_{non-dim}$	0.8106	± 0.00728	±0.89
$\Delta P_{t,non-dim}$	-0.2841	±0.0072	±2.54

Table 2.5: Sample Uncertainties of Flow Variables for an Empty Tunnel at 0° and at R^*=1

Parameter	Reference Value	Absolute Uncertainty	Relative Uncertainty (%)
Q_{tunnel}	0.9699 psi	± 0.0019 psi	±0.20
$Q_{non-dim}$	0.7279	±0.0024	±0.33
$\Delta P_{t,non-dim}$	-0.2752	± 0.0014	±0.52
$\Delta Q_{non-dim}(\%)$	27.19%	± 0.2864%	±2.86

Table 2.6: Sample Uncertainty for $\Delta Q_{non-dim}(\%)$ for a Test Configuration of Engine Baseline Model with Gearbox Fairing at 0° and at R^*=1, Downstream Condition

Parameter	Reference Value	Absolute Uncertainty	Relative Uncertainty (%)
$\Delta Q_{non-dim}(\%)$	89.84%	± 2.57%	±2.86

Table 2.7: Sample Uncertainty for C_p for a Test Configuration of Engine Baseline Model at 0° and at Axial Distance of 35 inches

Parameter	Reference Value	Absolute Uncertainty	Relative Uncertainty (%)
C_p	-0.2171	± 0.0029	±0.013

Table 2.8: Sample Uncertainty for C_p for a Test Configuration of Engine Baseline Model with Gearbox Fairing and Crane Beams at 0° and at Axial Distance of 35 inches

Parameter	Reference Value	Absolute Uncertainty	Relative Uncertainty (%)
C_p	-0.6198	± 0.0083	±0.013

Chapter 3

Results and Discussion

In this chapter, complete pressure survey results for an empty axisymmetric tunnel as well as different bypass test model configurations are presented, compared and discussed. First, the characteristics of an empty tunnel flow is described in Section 3.1. Pressure survey results for different bypass model configurations of increasing complexity are then presented from Section 3.2 to Section 3.5.

The High Flow Nacelle Bypass Concept developed by Gulfstream Aerospace is expected to result in Mach numbers in the range of 0.4 at the bypass inlet section corresponding to the inlet splitter. However, since the fan of the facility was optimized for a previous application in a 15 inch x 15 inch test section, it is not capable of reaching the Mach number range prescribed at the inlet section on the constant diameter cylinder/engine baseline model. For an empty wind tunnel under normal atmospheric conditions, the Mach number at the upstream section was found to be 0.315. Under similar operating conditions and fan RPM as before and with the installation of just the engine baseline model in the test facility, the Mach number at the inlet section was found to be reduced to 0.285. The Mach number at the inlet section was further decreased to 0.18 with the installation of the gearbox fairing on the underside of the engine baseline model. Therefore, the experiments performed on all the test configurations were conducted at the maximum fan RPM of 1750.

3.1 Empty Wind Tunnel

Since the bypass flow facility was modified from a 15 inch x 15 inch square test section to an 11.1 inch diameter axisymmetric tunnel, while retaining the existing wind tunnel inlet and diffuser design, pressure surveys were conducted to fully map the flow in the empty tunnel

at both the upstream and downstream locations to detect any flow uniformity issues. The upstream and downstream measurement stations correspond to the bypass inlet and exit measurement stations, respectively.

The total pressure measurements within the empty tunnel were obtained using the 90°-miter-joint total-pressure probe described in Section 2.3.1.1. The total-pressure probe was traversed from the wall to the center of the empty axisymmetric tunnel for a total of 22 radial steps under user-specified traverse distances and with a circumferential step of 5° between radial surveys. The process of data acquisition starts from 0° which corresponds to the 12 O'clock position in a counter clock-wise manner for a full 360°. To accurately capture the boundary layers, the number of traverse points near the wall of the axisymmetric test section was increased. The nondimensionalized total pressure profiles at the upstream and downstream locations for an empty tunnel at 0° were plotted in Fig. 3.1a. The normalized radius in the figure is expressed as

$$R^* = \frac{R_m - R_{inner}}{R_{outer} - R_{inner}} \tag{3.1}$$

Where R_{outer} and R_{inner} represent the radius of the inner tunnel wall and bypass model wall, respectively, while R_m refers to the probe radial location for a point measurement m. For the empty tunnel case, $R_{inner} = 0$. The difference between R_{outer} and R_{inner} was physically measured using the total pressure probe with the aid of the feedback capability of the Zaber linear traverse system described in Appendix I. With the prescribed radius normalization in Eq. 3.1 for an empty wind tunnel, a value of $R^* = 0$ corresponds to the center of the empty axisymmetric tunnel while a value of $R^* = 1$ corresponds to the inner surface of the tunnel wall. It can be observed in Fig. 3.1a that the total pressure losses are concentrated at areas close to the tunnel wall. This was expected due to the presence of boundary layers near the tunnel wall. The total pressure losses were seen at locations of approximately 90% of the radius and greater for the tunnel for the upstream case while for the downstream case, the total pressure losses were seen at locations of approximately 80% of the radius of the tunnel or greater. This was also expected since the flow is subjected to greater viscous losses near the tunnel wall as it develops from the upstream to the downstream

measurement location. There was no loss of total pressure at locations in the core of the empty axisymmetric test section. The thickness of the boundary layer at the upstream and downstream measurement locations is approximately 15% and 25% of the radius of the axisymmetric test section, respectively. The velocity measurements in Fig. 3.1b are normalized by the maximum velocity of the velocity profile, U_{max}.

The velocity profile in Fig. 3.1b was acquired using a total-pressure probe and the surface static tap installed on the test section wall. For more accurate mapping of the static pressures within the core section of the empty wind tunnel, the pitot-static probe was used to obtain pressure measurements. However, the goose-bend design on the pitot-static probe prevented the probe from reaching locations next to the wall. Therefore, measurements were only taken to 93% of the radius of the tunnel. Even with the limited range of traversing distance with the pitot-static probe, the survey still managed to capture the boundary layers of the rotating test section. The growth of boundary-layer thickness from the upstream section to the downstream section can be observed qualitatively in the nondimensionalized dynamic pressure, $\Delta Q_{non-dim}(\%)$ contour map shown in Fig. 3.2. It can be observed that the measured nondimensionalized dynamic pressures within the boundary layers are approximately 38% less than the average of all nondimensionalized dynamic pressures at the core of the test section at the downstream section. The flow at the core of the empty tunnel was found to be very uniform. With the exclusion of the boundary layers, the average value in percentage difference in nondimensionalized dynamic pressure at each measurement point to the averaged core was 0.015%. The same level of uniformity and accuracy was also achieved at the downstream section. The average percentage difference for the downstream section was 0.02%.

Fig. 3.3 shows the Mach number contour maps for the empty axisymmetric test section at the upstream and downstream measurement locations with identical scales. These contour maps were obtained at a maximum fan RPM of 1750. It can be observed that the maximum Mach number achieved at the upstream and downstream measurement section were approximately 0.315 and 0.33, respectively. The slight increase in Mach number at the downstream section is due to the increase in boundary-layer thickness at the downstream location as compared to the upstream section.

3.2 Engine Baseline Model

The test configuration of the engine baseline model consisted of the constant diameter cylinder on the tunnel centerline with the contraction cone and aft-body diffuser attached upstream and downstream of the cylinder, respectively. When assembled within the axisymmetric tunnel, the annular bypass duct is created. Data acquistion for this model configuration was obtained with the use of a total-pressure probe and the surface static tap installed on the test section wall as described in Section 2.3.1.2.

The total-pressure surveys conducted at the upstream and downstream locations of the annular bypass yield the nondimensionalized total pressure profile as shown in Fig. 3.4a. The diameter of the bypass duct has been normalized according to Eq. 3.1 with a value of $R^* = 0$ representing the bypass model wall and a value of $R^* = 1$ corresponding to the inner tunnel wall. Not surprisingly, it was found that the boundary layers at the downstream section of the bypass duct are significantly thicker than the boundary layers at the upstream location. This is shown in Fig. 3.4b.

The shape of the boundary layer at the upstream section was found to be asymmetric. The boundary-layer at the tunnel wall was thicker than the boundary layer at the model wall. This is because at regions close to a value of $R^* = 0$, the wall extends forward for only about 14 inches and converges at the tip of the contraction cone. Therefore, the boundary layer is just starting to develop. The boundary-layer thickness at this wall at the upstream measurement station is approximately 10% of the normalized radius of the bypass duct. Comparatively, at values close to $R^* = 1$, or at the tunnel wall, the boundary layer has been developing over the length of wind tunnel inlet, across the square to round section before entering the bypass annulus. Therefore, the boundary-layer thickness at the tunnel wall is over 40% of the normalized radius of the bypass duct.

Fig. 3.5 shows the nondimensionalized total pressure mapping of the engine baseline model at the upstream section. The flow was mapped from the 12 O'clock position, which was defined as 0° in the experiment, and in a counter clock-wise manner for 360°. The contour map represents the mapped flow in the bypass duct with the outer and inner radius of the ring representing the inner wall of the circular tunnel section and the wall of the

engine baseline model, respectively. The bypass duct encloses the bypass baseline model and is included in the figure as a filled white circle at the center. Since the test configuration for this case is just the engine baseline model, there are no engine components which will restrict and block the annular flow path, therefore the flow features in the contour map should be almost axisymmetric. An interesting flow feature in this contour map is that the four narrow sections of total-pressure loss across the annular flow path are all set 90° apart from each other with the first at a location of 45° away from the 12 O'clock position. This flow disturbance is a result of the placement of four struts with NACA 0012 airfoil cross sections and measuring 0.24 inches thick which creates a small wake propagating downstream. The struts are located 11 inches ahead of the upstream measurement station and on the contraction cone. The function of the struts is to provide essential structural support and positioning of the engine baseline model. The total pressure losses due to the struts were observed to be small.

A further analysis on the effect of the support struts on the bypass annulus flow is shown in Fig. 3.6. The figure shows the nondimensionalized total pressure profiles for 40°, 45° and 50°. The locations of these profiles are indicated on a nondimensionalized total pressure contour map shown previously in Fig. 3.5. It can be observed that at 40°, the nondimensionalized total pressure profile is asymmetric. This is due to higher viscous losses sustained by the flow on the tunnel wall as compared to the model wall. By stepping to a circumferential angle of 45°, which corresponds to the circumferential position of the strut, it can be observed that the nondimensionalized total pressure profile has been distorted. The total pressure losses were recorded not only on the tunnel and model wall but also in the core of the flow. The total pressure losses in the core are in the range of 2.5-5% of the inlet dynamic pressure, Q_{inlet}. At 50°, the nondimensionalized total pressure profile is similar to the one at 40°.

Fig. 3.7 and Fig. 3.8 shows the nondimensionalized total and dynamic pressure mapping of the bypass baseline model at the downstream section. As observed in Fig. 3.7, with the exception of the boundary layers, no significant total pressure losses were observed in the core. The nondimensionalized dynamic pressure contour plot in Fig. 3.8 shows that the velocity of the flow has increased at the core of the annular duct. The boundary layers have

also grown thicker; this corresponds with the boundary-layer profiles plotted in Fig. 3.4b. There were no visible thin sections of significant pressure loss due to the strut wakes like the ones observed in Fig. 3.5. However, the disturbance is still observable. The angular locations downstream corresponding to the angular position of the upstream struts show that the boundary layer close to the tunnel wall is thickened and seen as a bump in the contour plot of the annulus core flow. However, with the exception of the strut flow disturbances, the flow of the entire annulus downstream section appears to be circumferentially uniform.

Fig. 3.9 shows the Mach number contours for this configuration at the upstream and downstream locations. It was found that the Mach number at the core of the flow at the upstream section is approximately 0.285. This number is lower than the Mach number achieved with an empty wind tunnel. This is because the engine baseline model has blocked 75% of the axisymmetric test section, creating a larger total pressure loss compared to an empty wind tunnel. Since the fan was not optimized to recover this magnitude of total pressure loss, the Mach numbers within the bypass annulus decreased. As flow develops across the bypass annulus from the upstream to the downstream section, the velocity of the flow increases. Therefore, the Mach number at the core of the flow at the downstream section is approximately 0.31.

In addition to the traverse measurements, the surface static pressures for this test configuration were also recorded and plotted in a contour map in Fig. 3.10. This contour map represents the change in surface static pressure measurement with respect to the measurement from the first static tap and nondimensionalized by $Q_{inlet}{}'$ as described in Eq. 2.10. The contour map represents the surface static pressure coefficients for the entire circumferential extent of 360° for the test section inner wall. The Y-axis of this 2-D contour plot represents the axial distances in inches and the X-axis as the circumferential angle. The axial distances of 1 inch and 35 inches correspond approximately to the planes at the upstream and downstream measurement stations, respectively. As expected, the contour plot shows that the surface static pressure coefficients decrease along the axial length of the axisymmetric test section. At areas close to the downstream locations, the surface static pressure coefficient is approximately 18 - 20% lower than the surface static pressure coefficients at the upstream locations. This is due to the growth of the boundary layer which increases

the velocity in the core flow which results in a drop the static pressure measurments.

3.3 Engine Baseline Model with Gearbox Fairing

The complexity of the test configurations was increased by adding the gearbox fairing to the underside of the engine baseline model, 180° degrees away from the 12 O'clock position. The same flow survey procedure was followed as with the engine baseline model with flow mapping from the 12 O'clock position around the model for 360°.

Fig. 3.11 and Fig. 3.12 depicts the nondimensionalized dynamic and total pressure mapping of the test configuration for the downstream measurement location, respectively. It was found that the introduction of the gearbox fairing significantly alters the annular flow features at the downstream section. The flow remains circumferentially uniform with almost equal boundary-layer thickness on both sides of the tunnel and bypass wall for over 90°. However, at angular locations of 125° and greater, the flow was heavily distorted, with significant losses sustained as the angular position increases. The pressures continue to significantly decrease before gradually recovering after 235° before again reaching a state of circumferential uniform flow with equal boundary-layer thickness on both walls. The region of heavily distorted flow at the underside of the bypass baseline model is due to the presence of the gearbox fairing. The circumferential span of the gearbox fairing is 110° and was depicted in Fig. 3.11 as two lines, each 55° from the 180° position. This sector represents the physical location of the gearbox fairing whose aft surface is attached 1.7 inches ahead of the tip of the total-pressure probe. Therefore, it is clear that the gearbox fairing significantly alters the annular flow features.

Further analysis of the nondimensionalized dynamic pressure contour plot in Fig. 3.11 reveals that the dynamic pressure losses sustained at the downstream section of the gearbox is above 80% of Q_{inlet}. The raw data obtained from the survey (later confirmed by surface oil flow visualization) suggests highly separated flow at the downstream section behind the gearbox fairing. At angular positions close to 180°, it was discovered that numerous radial measurement points of total pressure were recorded to be lower than the surface static tap measurement at the tunnel wall, P_s. Although the total pressure probe used in the survey

has a 30° degree chamfered tip to accommodate a modest range of flow angles, the device is not equipped to correctly capture the physics of highly separated flows. Therefore, the measurement points of negative dynamic pressures in the annular duct have been set to a value of zero for the test configuration of the engine baseline model with the gearbox fairing at the downstream section. Total pressure measurements with values that were lower than the surface static tap measurement were set to be equal the surface static tap measurement value.

Since the edge of the gearbox fairing corresponds to an angle of 125°, the downstream nondimenensonalized total pressure and velocity profiles from 85° to 135° were plotted to examine the behavior of the flow around the edge of the gearbox fairing. This is shown in Fig. 3.13 and Fig. 3.14. $R^* = 1$ refers to the inner surface of the tunnel while $R^* = 0$ corresponds to the bypass model wall. It can be observed that at 85°, the boundary-layer thickness was about 35% of the normalized radius of the bypass duct. The boundary layers were approximately the same thickness on both sides of the wall. By further stepping through the angular positions until 120°, the shape of the boundary layers change. While the boundary layer close to the bypass wall seems to be relatively similar in all the angular positions before 120°, the boundary layer close to the tunnel wall starts to get thicker. This is shown in Fig. 3.14. Total pressure losses in the core flow for the nondimensionalized total pressure profile at 120° in the range of 5 - 10% from Q_{inlet} were also observed in Fig. 3.13. A further increase in angular position to 125° and 135° which corresponds to the edge of the gearbox fairing and into the region behind the fairing results in highly distorted boundary-layer profiles with significant total-pressure loss. The behavior of the profiles indicates that the presence of the gearbox fairing causes flow distortion starting at least 15° before the edge of the fairing. Within the 15°, the core of the flow shifts away from the tunnel wall and closer to the bypass wall. The shift continues as the angular position gets closer to the edge of the gearbox fairing. Once the angular position is at the edge or behind the gearbox fairing, the flow becomes distorted with high total pressure losses.

Fig. 3.15 compares the nondimensional dynamic pressure profiles at 0° for the engine baseline model/constant diameter cylinder and with an engine baseline model fitted with the gearbox fairing. It is clear from Fig. 3.15 that by installing the gearbox fairing, the

flow at 0° increases in speed. The increase in nondimensionalized dynamic pressure at this location for a gearbox fairing compared to the case without a gearbox fairing is almost 100%. The reason for this effect can be explained by mass conservation. As flow approaches the inflow diverter section of the gearbox fairing, the gearbox with the 110° circumferential span blocks over 30% of the annular flow path. Therefore the effective area of the annular flow path has been further reduced from the bypass inlet section of 41.05 in^2 to approximately 28 in^2. The mass flow has to be conserved, thus it is "pushed" upwards from the underside of the annular duct to the upper side close to 0°, causing the flow at that position to increase in velocity.

The nondimensional dynamic pressure for the engine baseline model with gearbox fairing at the upstream section is shown in Fig. 3.16. The survey was conducted at approximately 4.5 inches upstream of the tip of the flow diverter section of the gearbox fairing. Even at this distance upstream of the article, it can be shown that the flow features at the bypass inlet section is influenced by the presence of the gearbox fairing. Due to the blockage presented by the fairing, flow velocity at the underside of the annular duct decreases; the nondimensionalized dynamic pressure at this region is reduced by 5 - 10% of the inlet dynamic pressure, Q_{inlet}. Conversely, flow velocity increases at the upper side of the bypass by as much as 25% of Q_{inlet}. The blockage from the gearbox fairing also reduces the Mach number at the upperside of the bypass annulus to approximately 0.18. This is shown in Fig. 3.17.

Fig. 3.18 provides a comparison of nondimensionalized dynamic pressure at the downstream section for an engine baseline model with and without gearbox fairing. The parameter used to generate this plot can be found in Table 2.2. As shown in Fig. 3.18, the difference between the nondimensionalized dynamic pressure at the upper side of the annular duct for a model with and without fairing is 60 - 100%, with the highest percentage difference originating from the sections close to the boundary layer edge. As described in the previous sections, this is due to the increase in flow velocity caused by the reduced effective area "seen" by the flow. As described previously, negative values of dynamic pressure in the region behind the fairing were set to zero which yields percentage differences in normalized dynamic pressure of -100%.

3.4 Engine Baseline Model with Gearbox Close-Out Fairing Removed

This test configuration involves removing the gearbox close-out fairing from the test model, leaving only the in-flow diverter and the main gearbox fairing attached to the engine baseline model. Since it was observed in Section 3.3 that the flow behind the gearbox fairing is separated with significant pressure losses, this test configuration will provide the oppurtunity to further understand the fundamental behavior of the flow behind the gearbox fairing so that more effective fairings can be designed in the future. The flow survey procedure was followed as with the engine baseline model with gearbox fairing test configuration with flow mapping from the 12 O'clock position around the model for 360°.

Since it was expected that the flow behind the main gearbox fairing will be highly separated, the method of correction for negative dynamic pressures described in Section 3.3 was followed; negative dynamic pressures will be set to zero while total pressure measurements with values that are lower than the surface static tap measurements were set to be equal the surface static tap measurement value. Fig. 3.19 shows the nondimensionalized total pressure contour plot for this test configuration as well as the nondimensionalized total pressure profiles at various circumferential angles before and after the edge of the main gearbox fairing. The circumferential span of this article at 110° was also depicted in Fig. 3.19 as two lines, each 55° away from the 180° position.

It was observed that the general flow behavior of this test configuration is similar to the test configuration with the full gearbox fairing. Stepping in angular positions from the 12 O'clock position, the flow remains circumferentially uniform with viscous losses occuring only at the tunnel wall and model wall for over 90°. The flow starts to distort at circumferential angles close to the gearbox before sustaining significant pressure losses at areas behind the main gearbox fairing. The flow improves when it is out of the region behind the main gearbox fairing and recovers to the initial state of circumferential uniformity after 270°.

As observed in Fig. 3.19, the nondimensionalized total pressure profile at 85° is almost symmetric with approximately equal amount of total pressure loss on both sides of the

wall. At 100° and 110°, the nondimensionalized total pressure profiles have started to distort. However, there is still no total pressure loss in the core of the flow at these angles. Nevertheless, once at 115°, the losses of the flow is now significant with a complete distortion of the flow at angles of 120° and above. Compared to the full gearbox fairing configuration, flow did not fully distort until 125° which corresponds to the edge of the gearbox fairing (Fig. 3.13). Therefore, it can be concluded that for this test configuration, the complete distortion of the flow occurs at least 5° earlier than compared to the configuration of the engine baseline model with a full gearbox fairing.

Fig. 3.20 plots the boundary-layer profiles at 0° for the cases of engine baseline model, engine baseline model with full gearbox fairing and engine baseline model with close-out gearbox fairing removed on the same figure. It can be observed that with the close-out gearbox fairing removed, the flow at 0° further increases in speed as compared to the other two test cases. The increase in nondimensionalized dynamic pressure for this configuration at 0° compared to the full gearbox fairing case is approximately 40%. The increase in velocity of the flow on the upperside of the engine baseline model is induced by flow separation behind the main gearbox fairing. As confirmed in the oil flow visualization results in Fig. 3.29 and Fig. 3.30 described in Section 3.6, a portion of flow gets "pushed" upwards due to favorable pressure gradients at the upperside of the engine baseline model while the second portion of the flow separates downwards and recirculates towards the upstream direction. Therefore, the nondimensionalized dynamic pressures at the upperside of the engine baseline model increases.

3.5 Engine Baseline Model with Gearbox Fairing and Crane Beams

The final model geometry change for the bypass baseline model with gearbox fairing is a pair of crane beams. The crane beams were attached to the upper side of the bypass baseline model. Details about this component and its attachment to the bypass baseline model are described in Section 2.1.1.3. Fig. 3.21 and Fig. 3.22 shows the nondimensionalized dynamic pressure and the nondimensionalized total pressure contour maps for this configuration.

Since the configuration includes the gearbox fairing, certain flow features were found to be similar to the previous test configuration described in Section 3.3. Significant pressure losses of up to 80% of Q_{inlet} in the nondimensionalized dynamic pressure compared to the Q_{inlet} were still detected at the regions behind the gearbox fairing. The flow disturbances from the crane beams are in the regions from 0° to 90° and are clearly shown in the nondimensionalized dynamic pressure and the nondimensionalized total pressure contour maps. Regions with increased nondimensionalized dynamic pressures and low total pressure losses represent the open webbing area between two beams. The percentage difference between the maximum and minimum nondimensionalized dynamic pressure at the crane beam section is 40 to 60%. In addition to the gearbox fairing, the introduction of the crane beams has further increased the blockage area in the annular duct and reduced the effective area of the annular flow path. Therefore, the maximum nondimensionalized dynamic pressure at the core flow has increased from 2.18 in the bypass baseline model with gearbox fairing to 2.4 for this case.

Fig. 3.23 shows the surface static pressure coefficient contour map of the inner tunnel wall for this configuration. The surface static pressure coefficient is defined in Eq. 2.10. Since certain engine model components are positioned either flush or within close proximity to the inner tunnel wall, the effects of these components on the surface static pressures were observed. For example, the gearbox fairing is attached flushed to the tunnel inner wall surface. Therefore, no surface static pressure measurements were recorded in that region. This area is represented by a model of the gearbox fairing superimposed on the surface static pressure coefficient contour map. In addition, the sudden drop in surface static pressure coefficients from 340° to 100° at approximately axial distances of 22 inches and 31 inches is due to the placement of crane beams on the engine baseline model. It can also be observed that at areas close to the tip of the in-flow diverter component of the gearbox fairing, the surface static pressure coefficient increases to approximately 0.5. This is due to the decrease in velocity of the flow when approaching the tip of the in-flow diverter. Theoretically, the flow will stagnate at the tip of the in-flow diverter. However, since there was not a surface static tap that was positioned exactly at the tip of the in-flow diverter, the effect of the stagnation point on the surface static pressure coefficients was

not observed. As the flow follows the contours of the in-flow diverter, a favorable pressure gradient was observed with static pressure coefficient measurements decreasing from 0.4 to -1.6. The coefficients continue to decrease around the main gearbox fairing until it reaches approximately -2 at areas behind the close-out gearbox fairing.

3.6 Surface Oil Flow Visualization

To provide additional flow diagnostics, surface fluorescent oil flow visualization was performed. The area of interest for the application of this technique is the surface area on the engine baseline model in which the close-out fairing for the gearbox is attached. This region is highlighted with black hash marks in a schematic of a partially assembled bypass CAD model in Fig. 3.24. This region wraps around the underside of the bypass baseline model for approximately 180° to extend to the opposite side of the view in Fig. 3.24. Scales in units of inches were attached to the surface of the bypass baseline model both longitudinally and circumferentially to provide length scale information.

Fig. 3.25 to Fig. 3.27 shows the result of this technique for the case of the full gearbox fairing in three views. The first picture (Fig. 3.25) is captured at a rotated view of 45° from the bottom of the engine baseline model, corresponding approximately to the 4 O'clock position with flow direction from left to right. The second picture (Fig. 3.26) is taken at approximately the same rotated angle as the first picture but on the opposite side of the bypass test models. The flow direction in this picture is from right to left. The third picture (Fig. 3.27) is taken at a 90° angle beneath the close-out fairing. Results show a large flow recirculation zone behind the close-out fairing of the gearbox. The flow initially stays attached on the close out fairing for approximately 2 inches before separating and then the streamlines wrap downwards to the underside of the bypass baseline model and flowing backwards in the upstream direction.

The second area of interest includes the surface area behind the main gearbox fairing with the close-out fairing removed. This region is highlighted with black hash marks in the schematic shown in Fig. 3.28. Fig. 3.29 and Fig. 3.30 show the results of this flow visualization technique for the case where the close-out fairing was removed. As observed

in these two pictures, once the flow leaves the edge of the main gearbox fairing, it divides into two portions separated by a shear layer. Due to favorable pressure gradients at the upperside of the engine baseline model, the first portion of the flow gets "pushed" upwards towards that direction while the second portion of the flow separates downwards and recirculates towards the upstream direction. The shear layer also gets thicker as the flow progresses downstream. Since the flow is fully separated at areas right behind the main gearbox fairing, there are no shear forces on the surface of the engine baseline model. Hence, the fluorescent oil remain as spray speckles on the model.

Chapter 4

Summary, Conclusions and Recommendations

4.1 Summary

A High-Flow Nacelle Bypass concept was introduced as a potential method to reduce sonic boom effects for a civilian aircraft operating at supersonic flight conditions. The concept employs an outer nacelle surface to encircle the asymmetric external engine protuberances of a traditional turbine engine to create a bypass flow path. However, the engine protuberances create a highly complex 3-D flow within the bypass annular flow region. Hence, the objective of this study was to experimentally investigate the flow features in a partially blocked annular duct which is representative of a High-Flow Nacelle Bypass concept with asymmetric engine protuberances.

The experiments were conducted in a newly-designed 11.1 inch diameter axisymmetric test section of a subsonic wind tunnel at the University of Illinois. An engine test model with front and aft flow components was installed within the test section to simulate the bypass flow path. The test section was rotated and pressure measurements were taken over a range of circumferential and radial positions at a maximum fan RPM of 1750 to create planar maps of nondimensionalized total and dynamic pressures. An empty wind tunnel was first tested to detect any flow uniformity issues before the different test configurations were investigated.

4.2 Conclusions

Key results from the experiments for the different test configurations are concluded in this section:

1. Empty Wind Tunnel

   (a) Excellent flow uniformity within the empty wind tunnel with the average difference in nondimensional dynamic pressure at each measurement point to the averaged core at 0.015% and 0.02% for the upstream and downstream measurents, respectively.

   (b) Mach number of 0.315 and 0.33 was reached at the upstream and downstream measurement locations, respectively.

2. Engine Baseline Model

   (a) The boundary layer near the tunnel wall is thicker than the boundary layer on the model wall within the bypass annulus at the upstream measurement location. This is due to the difference in boundary-layer development on both walls.

   (b) The loss due to the struts at the downstream locations have largely dissipated but is still visible as a "bump" in the annulus core flow.

3. Engine Baseline Model with Gearbox Fairing

   (a) Nondimensional dynamic pressure losses behind the gearbox fairing as compared to Q_{inlet} at the downstream section was above 80%.

   (b) Distortion of total pressure and velocity profiles begin at least 25° before the edge of the gearbox fairing.

   (c) Due to the blockage created by the gearbox fairing, the nondimensional dynamic pressure of flow at 0° increases to 2.18. The nondimensional dynamic pressure of flow for a baseline model was 1.2 at this location.

   (d) The presence of the gearbox fairing causes the flow velocity to reduce by 5-10% of the *Qinlet* at the underside of the annular duct at the upstream measurement location.

   (e) Flow visualization shows that the flow behind the gearbox fairing separates, wraps downwards to the underside of the baseline model and recirculates backwards in the upstream direction.

4. Engine Baseline Model witout Close-Out Fairing

   (a) Large pressure loss was observed behind the gearbox fairing. The distortion of the nondimensional total pressure profiles at regions around the edge of the fairing starts at least 5° earlier than for a full gearbox fairing case.

   (b) The nondimensional dynamic pressure of flow at 0° (12 O'Clock Position) increases to 2.4.

5. Engine Baseline Model with Gearbox Fairing and Crane Beams

   (a) Significant pressure loss was still detected at regions behind the gearbox fairing.

   (b) The increase in nondimensional dynamic pressures at regions from 0° to 90° represent the open webbing area between the two crane beams.

   (c) The installation of crane beams further increases the blockage in the annular duct. Therefore, the nondimensional dynamic pressure at the core flow increases to approximately 2.4.

4.3 Recommendations

Recommendations for the improvement of this experiment can be divided into three categories. The categories are facility, data acquisition and analysis improvements as well as the improvement of the geometry of the bypass duct.

1. Facility Improvements

   (a) The current fan for the facility was optimized for a previous application. Therefore, the fan was not able to drive the flow at the bypass inlet section to the desired Mach number of 0.4. Hence, to reach the prescribed Mach number, it is recommended that a new fan system be considered for this experiment. This fan should possess characteristics such as the capability to recover the high total pressure loss within the facility at a low volumetric flow rate.

   (b) Even though the accuracy of the alignment for the three axisymmetric tunnel sections was increased by using a laser pointer, the process can be improved. A

misalignment of the axisymmetric tunel section can disrupt the tunnel rotation system. Therefore, it is recommended that in addition to using the laser pointer, tracks should be installed on the ground to guide the axisymmetric pieces into position. This not only simplifies the facility assembly and disassembly process but increases the accuracy of the alignment process as well.

(c) The gear stepper motor used in this experiment is more suitable for high speed applications. Hence, it is recommended that the current gear stepper motor be replaced with a similar type of motor but for lower speed applications with a higher step angle accuracy. This will improve the accuracy of the circumferential angle.

(d) It was discovered that there was a minor leak between the surface connections of the fixed gear bearing and gear housing. At a fan RPM of 1750, this causes the fixed gear bearing to pull apart from the gear housing. The current solution to the problem is to attach a pair of tabs to physically maintain the connection between the fixed gear bearing and housing. However, to solve the problem, it is recommended that the choice of O-ring within the gear bearings be reconsidered. Time and cost permitting, the gear housing and fixed bearing should also be re-fabricated for a tighter fit.

2. Data Acquisition and Analysis Improvements

(a) The process of data acquisition for the bypass annulus (Pressure probe traversing at 25 radial steps with a circumferential step of 5°) takes approximately 3 hours. Therefore, the freestream dynamic pressure conditions at the end of the experiment differs from the conditions at the start of the experiment. The jump in the freestream conditions can be observed at areas close to 0° in the pressure contour maps. It is recommended that correction methods using the surface static measurements of the wind tunnel inlet be introduced to mitigate the effects of this problem.

(b) Although the 35 axial surface static taps proved to be satisfactory in providing surface static measurements of the tunnel inner wall, the resolution of the sur-

face static contour map can be improved. This can be achieved by installing additional axial surface static taps on the rotating test section C.

3. Improvements for the Bypass Duct Geometry

   (a) Since results show significant pressure losses at regions behind the close-out fairing with a large flow recirculation zone, it is recommended that the close-out fairing be re-designed. The quality of flow in the bypass can be further controlled by introducing vanes within the duct.

References

[1] Committee on Aeronautical Technologies, N. R. C., *Aeronautical Technology for the Twenty-First Century*, National Academies Press, 1992.

[2] Henne, P. A., *A Gulfstream Perspective on the DARPA QSP Program and Future Civil Supersonic Initiatives*, Nov. 2003.

[3] "The TU-144LL: A Supersonic Flying Laboratory," NASA Dryden Flight Research Center.

[4] Macdonald, D., "Concorde - Fifteen Years on the Front Line," *Society of Automative Engineers (SAE)*, 912193, 1991.

[5] Eames, J. D., "Concorde Operations," *Society of Automative Engineers (SAE)*, 912161, 1991.

[6] "An Explanation of Sonic Fronts in Supersonic Conditions," Schematic Drawn By Dwight Looi, Jan 2007.

[7] Sparrow, V. and Coulouvrat, F., "Status of Sonic Boom Knowledge," *International Civil Aviation Organization(ICAO)*, Paper CAEP/7-IP/18, 2007.

[8] Seebass, A. R. and George, A. R., "Design and Operation of Aircraft to Minimize Their Sonic Boom," *Journal of Aircraft*, Vol. 11, No. 9, September 1974, pp. 509–517.

[9] Plotkin, K. J., Page, J. A., Graham, D. H., Pawlowski, J. W., Schein, D. B., Coen, P. G., McCurdy, D. A., HaeringJr, E. A., Murray, J. E., Ehernberger, L. J., Maglieri, D. J., Bobbitt, P. J., Pillon, A., and Salamone, J., "Ground Measurements of a Shaped Sonic Boom," AIAA 2004-2923, *10^{th} AIAA/CEAS Aeroacoustics Conference*, May 2004.

[10] Howe, D. C., SimmonsIII, F., and Freund, D., "Development of the Gulfstream Quiet Spike for Sonic Boom Minimization," AIAA 2008-0124, *46^{th} Aerospace Sciences Meeting*, Reno, NV, January 2008.

[11] Cowart, R. and Grindle, T., "An Overview of the Gulfstream/NASA Quiet Spike Flight Test Program," AIAA 2008-0123, *46^{th} Aerospace Sciences Meeting*, Reno, NV, January 2008.

[12] Conners, T. R., Howe, D. C., Whurr, J. R., and Smith, C. F., "Conceptual Design, Integration and Development Plan for an Efficient Low Sonic Boom Propulsion System Employing Advanced Supersonic Engine Cycles," *NASA Contract NNC04CA29C Final Report-Public Distribution*, 2008.

[13] Conners, T. R., Howe, D. C., and Henne, P. A., "Isentropic Compression Inlet for Supersonic Aircraft," U.S. Patent Application, Application No.11/639,339; Filed 15 Dec. 2006.

[14] Conners, T. R. and Howe, D. C., "Supersonic Inlet Shaping for Dramatic Reductions in Drag and Sonic Boom Strength," AIAA 2006-0030, *44th Aerospace Sciences Meeting*, Reno, NV, January 2006.

[15] Conners, T. R., Merret, J. M., Howe, D. C., Tacina, K. M., and Hirt, S. M., "Wind Tunnel Testing of an Axisymmetric Isentropic Relaxed External Compression Inlet at Mach 1.97 Design Speed," AIAA 2007-5066, *43rd AIAA/ASME/SAE/ASEE Joint Propulsion Conference and Exhibit*, Cincinnati, OH, July 2007.

[16] Conners, T. R., "Low Shock Strength Inlet," U.S. Patent Application, Application No.12/000,066; Filed 7 Dec. 2007.

[17] Conners, T. R., "Low Shock Strength Propulsion System," U.S. Patent Application, Application No.12/257,982; Filed 24 Oct. 2008.

[18] Yeong, Y. H., Chiles, I. M., Bragg, M. B., Elliott, G. S., Loth, E., and Conners, T. R., "Wind Tunnel Testing of a Nacelle Bypass Concept for a Quiet Supersonic Aircraft," AIAA 2009-4207, *39th AIAA Fluid Dynamics Conference*, San Antonio, TX, June 2009.

[19] Gebhardt, A., *Rapid Prototyping*, Handser Gardner Publications, 2003.

[20] Morel, T., "Comprehensive Design of Axisymmetric Wind Tunnel Contactions," *Journal of Fluids Engineering*, Vol. 97, June 1975, pp. 225–233.

[21] Blevins, R. D., *Applied Fluid Dynamics Handbook*, Van Nostrand Reinhold Company Inc., New York, 1984.

[22] Rae, W. H. and Pope, A., *Low Speed Wind Tunnel Testing*, John Wiley & Sons Inc., 2nd ed., 1984.

[23] Jacobs, J. J., *Ice Airfoil Seperation Buble Measurements by Particle Image Velocimetry*, Ph.D. thesis, University of Illinois, Urbana-Champaign, 2007.

[24] Busch, G. T., *Ice Accretion Aerodynamic Simulation on a Subscale Model*, Master's thesis, University of Illinois, Urbana Champaign, 2006.

[25] Coleman, H. W. and Steele, W. G., *Experimentation and Uncertainty Analysis for Engineers*, John Wiley & Sons Inc., 1989.

[26] Pope, S. B., *Turbulent Flows*, Cambridge University Press, 2000.

[27] Anderson, J. D., *Fundamentals of Aerodynamics*, McGraw-Hill, 3rd ed., 2001.

Figures

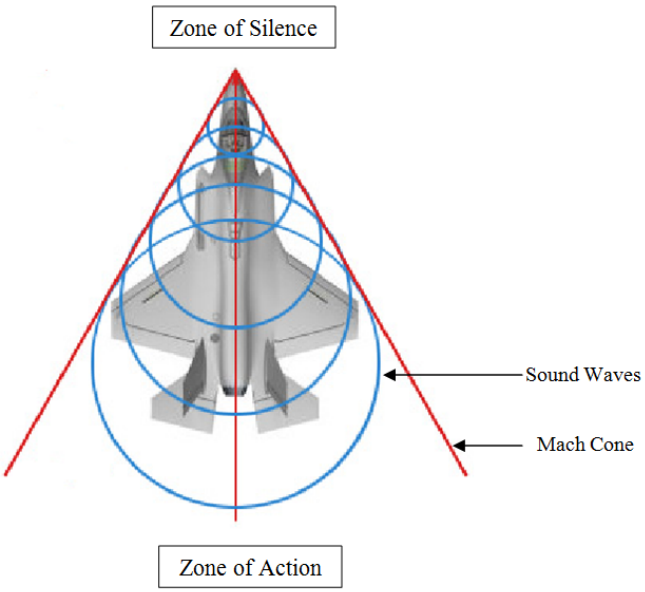

Fig. 1.1: Mach Cone of a Supersonic Aircraft[6]

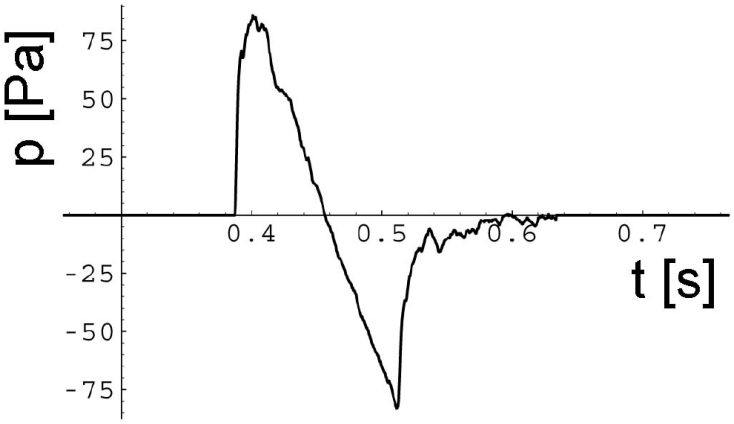

Fig. 1.2: Measured N-Waveform of an F-15 Aircraft[7]

(a)

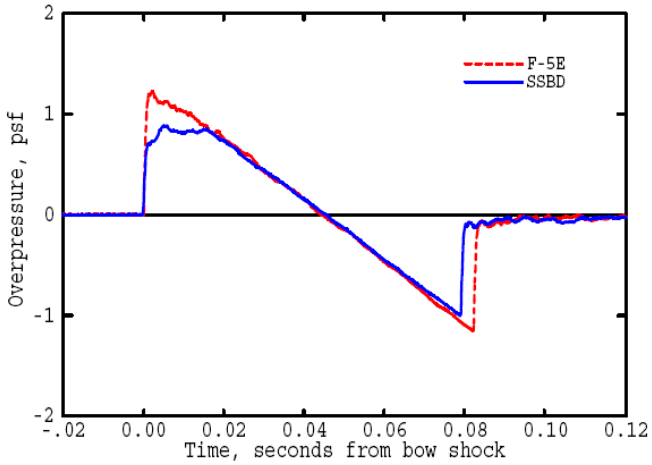

(b)

Fig. 1.3: Shaped Sonic Boom Demonstator(SSBD) Program (a) Modified F5-E Aircraft (b) Comparison of Boom Siganture between the SSBD Aircraft and the F5-E Aircraft[9]

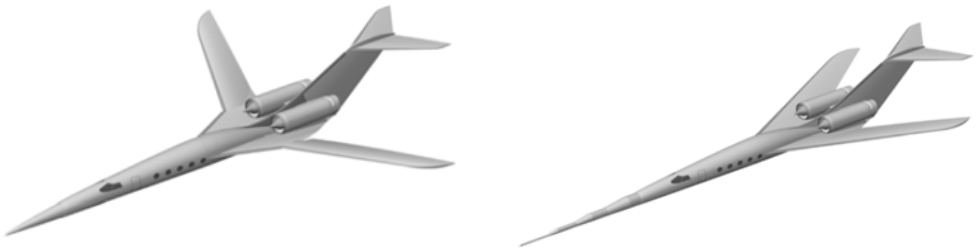

(a) (b)

Fig. 1.4: Quiet Spike on a Supersonic Aircraft (a) Aircraft with Stowed Quiet Spike (b) Morphing of Nose Cone of Aircraft with Extension of Quiet Spike[10]

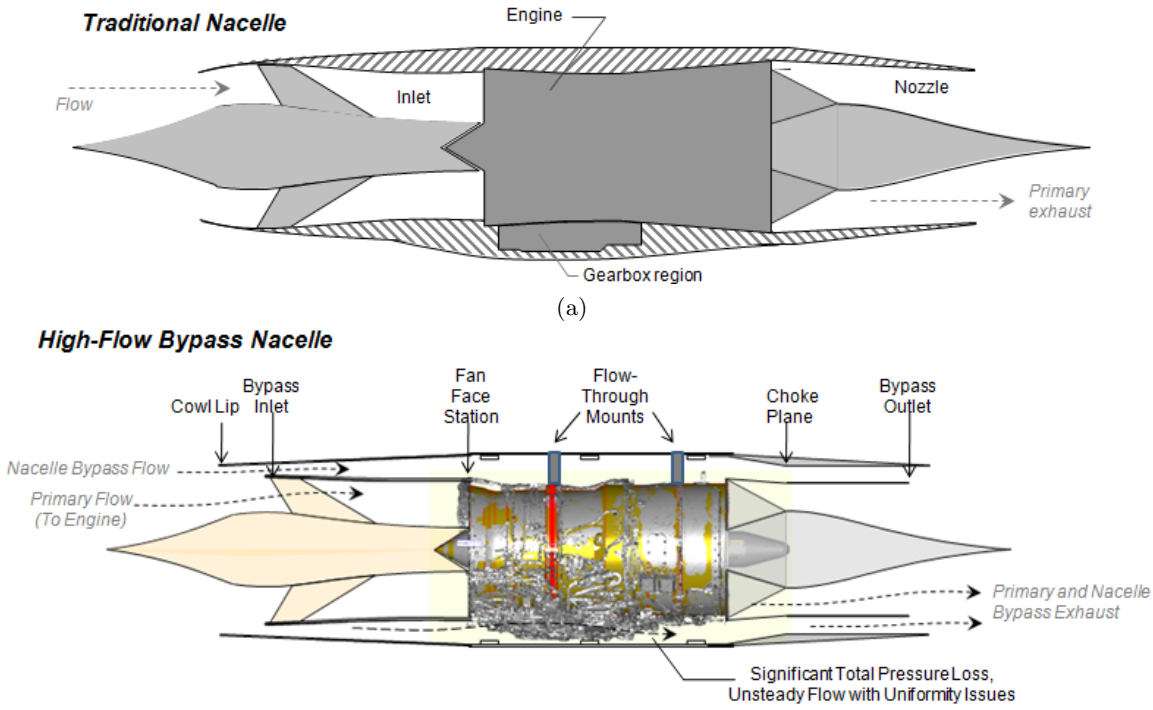

Fig. 1.5: Key Features of a High Flow Nacelle Bypass Nacelle Compared to a Traditional Nacelle (a) Traditional Nacelle (b) Nacelle Bypass Concept[18]

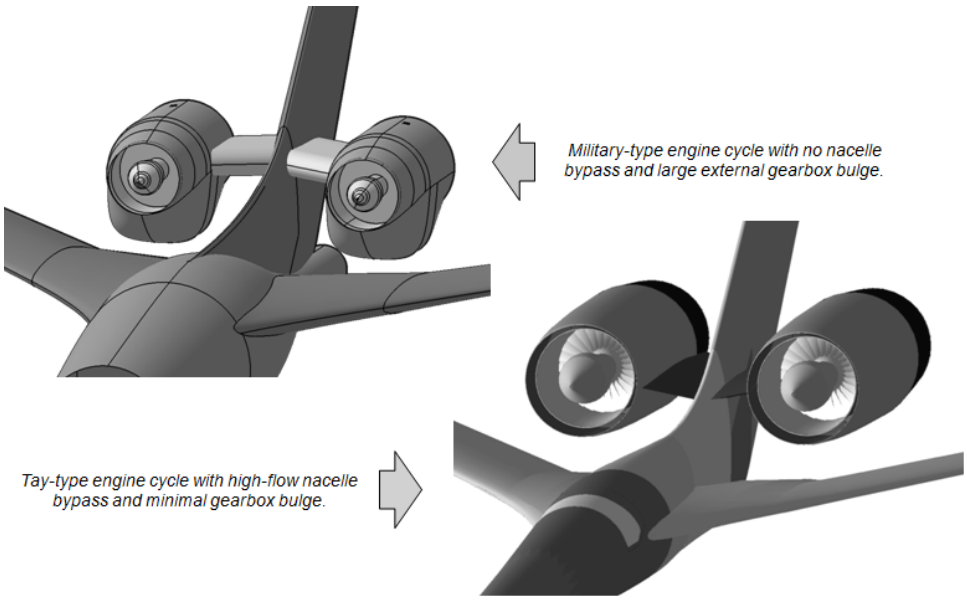

Fig. 1.6: Role of High-Flow Nacelle Bypass in Reducing Surface Bulging Associated with the Gearbox[18]

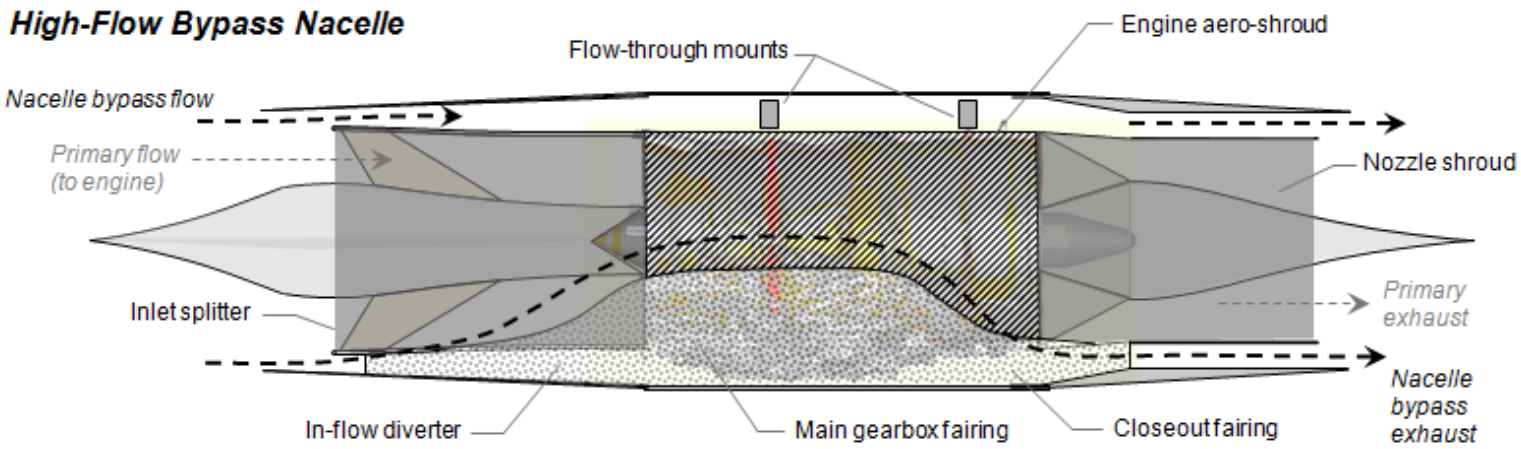

Fig. 1.7: Engine and Nozzle Shrouding with Gearbox Fairing for the High-Flow Nacelle Bypass Concept[18]

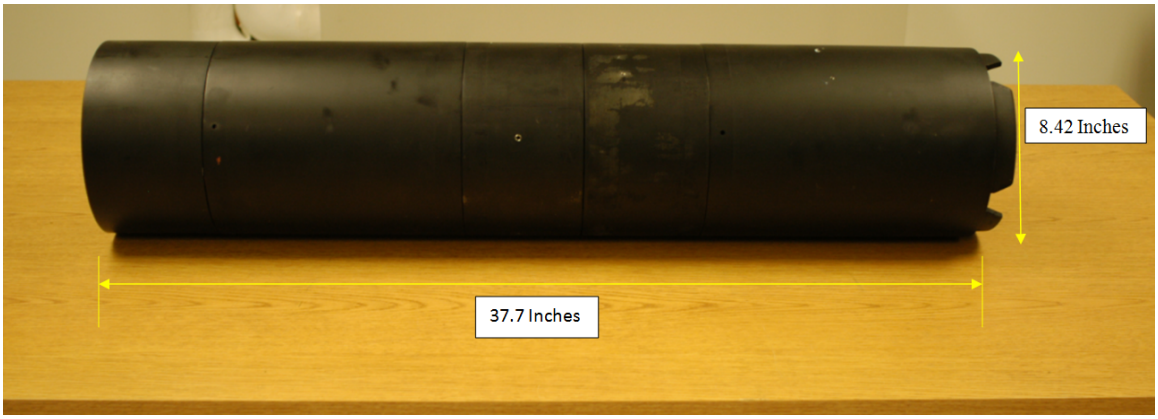

Fig. 2.1: Assembled Bypass Baseline Model

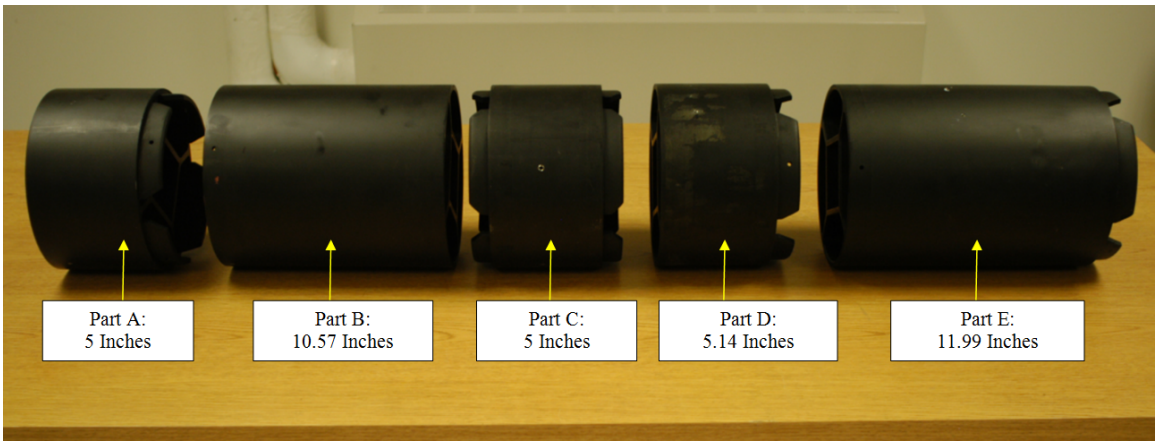

Fig. 2.2: Different Segments of the Bypass Baseline Model

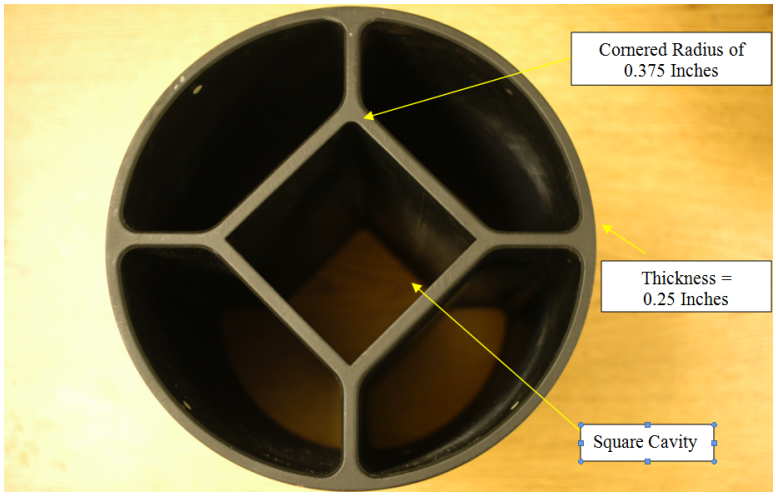

Fig. 2.3: Square Cavity Design Within Bypass Baseline Model

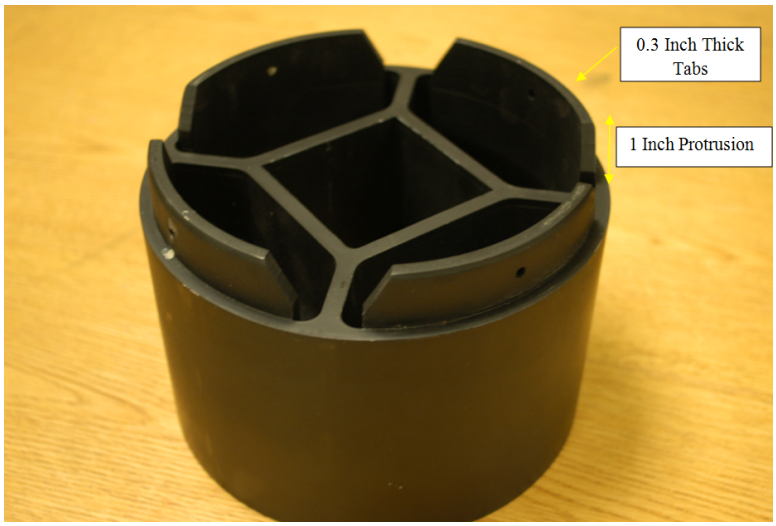

Fig. 2.4: Tabs on Bypass Baseline Model

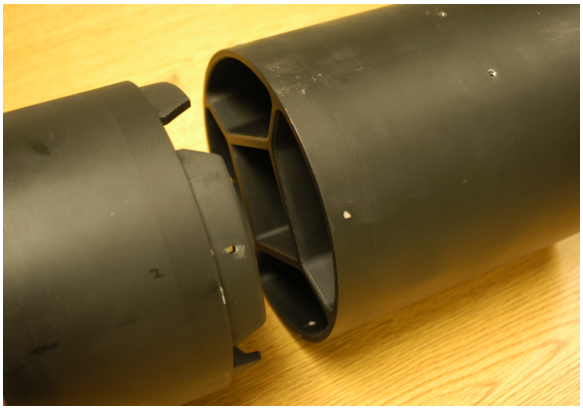

(a)

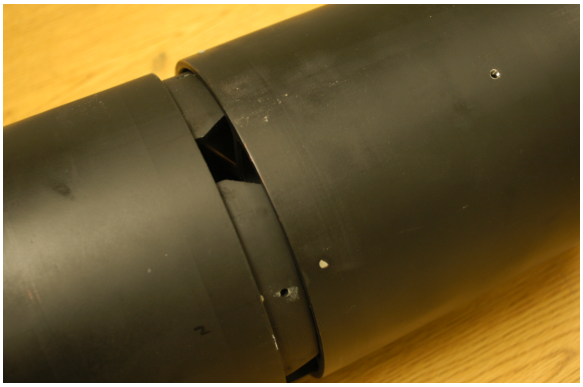

(b)

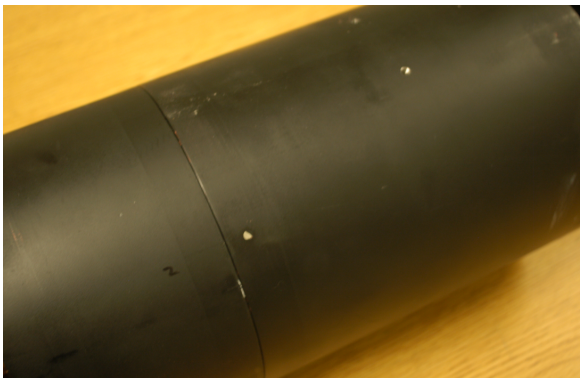

(c)

Fig. 2.5: Connecting the Different Segments of Bypass Baseline Models using Tabs

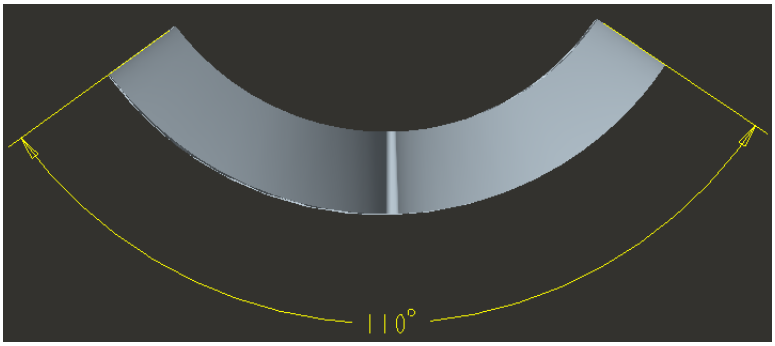

(a)

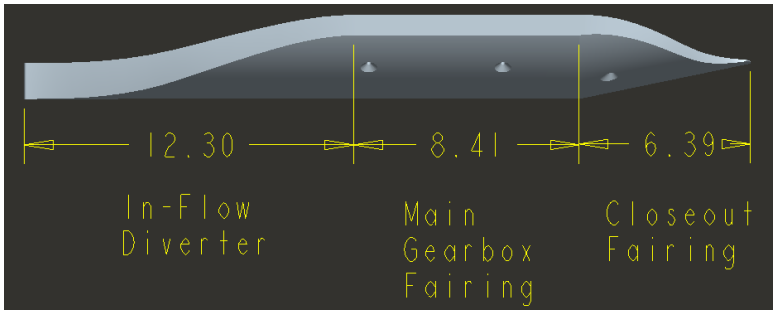

(b)

Fig. 2.6: CAD Model and Dimensions of the Gearbox Fairing (a) Front View (b) Side View

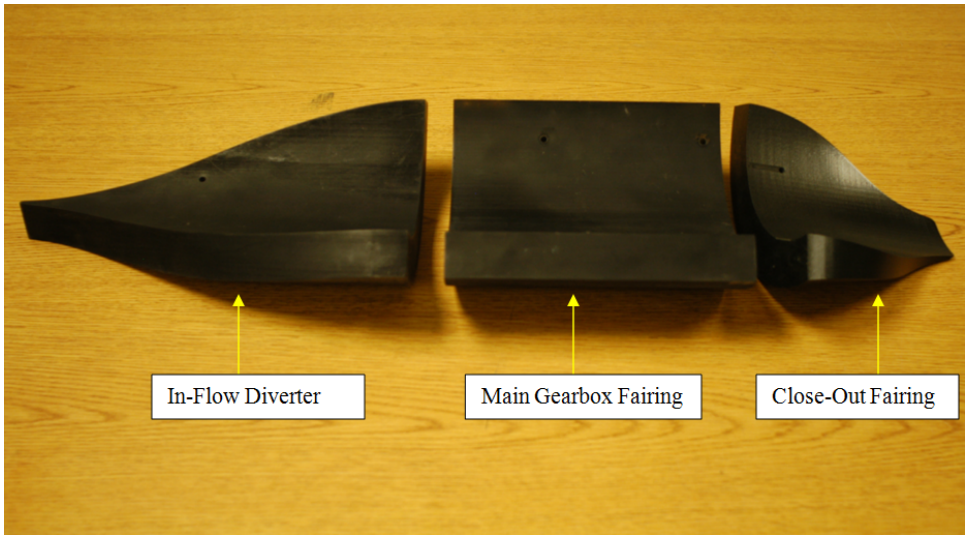

Fig. 2.7: SLA Model of the Gearbox Fairing

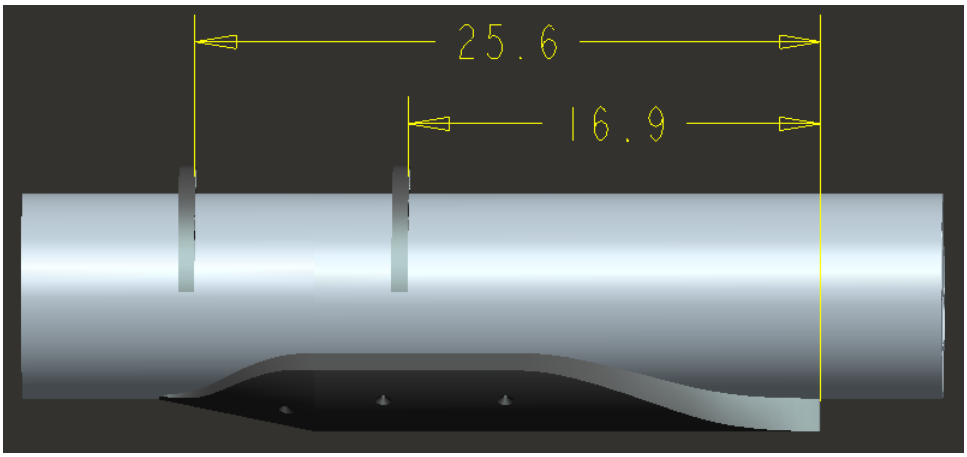

(a)

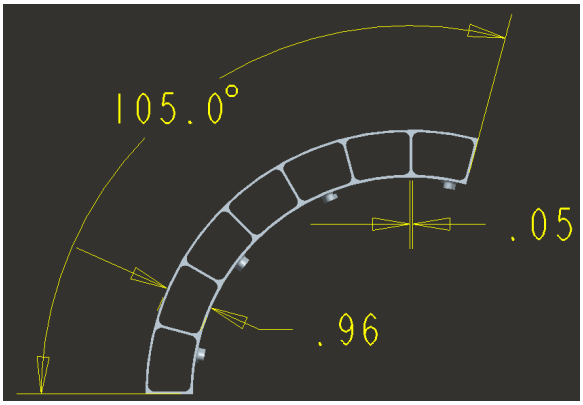

(b)

Fig. 2.8: Key Dimensions of the Crane Beams (a) Position of Crane Beams with Respect to Gearbox Fairing on the Engine Baseline Model (b) Front View of the Crane Beam

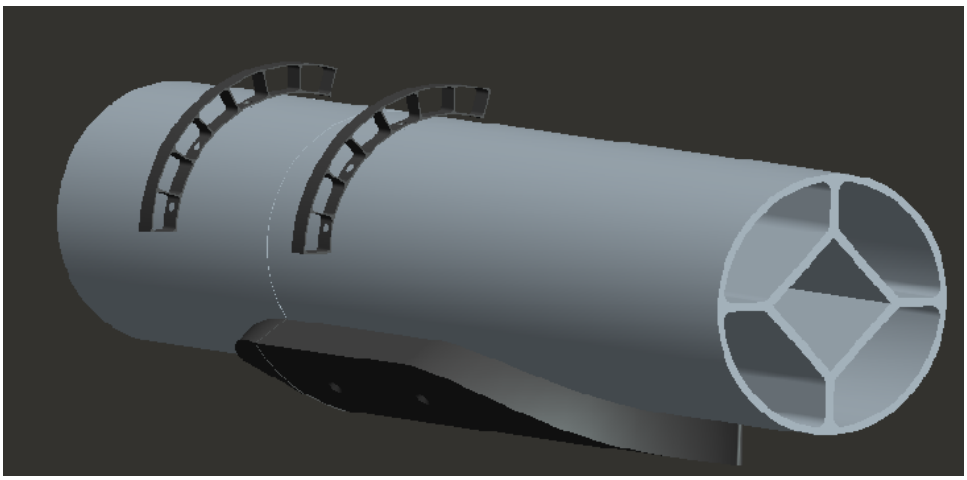

Fig. 2.9: Oblique CAD view of the Attachment of Crane Beams to the Engine Baseline Model

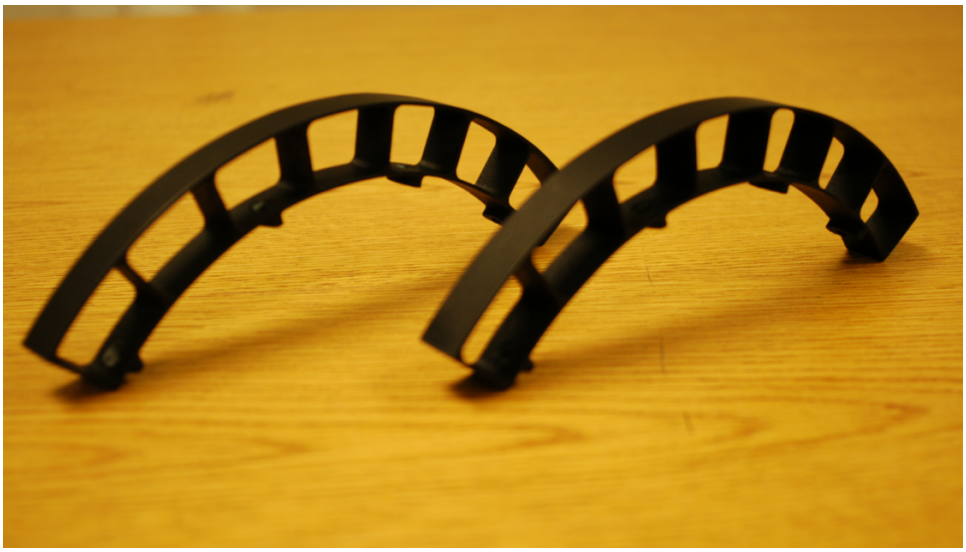

Fig. 2.10: SLA Model of the Crane Beams

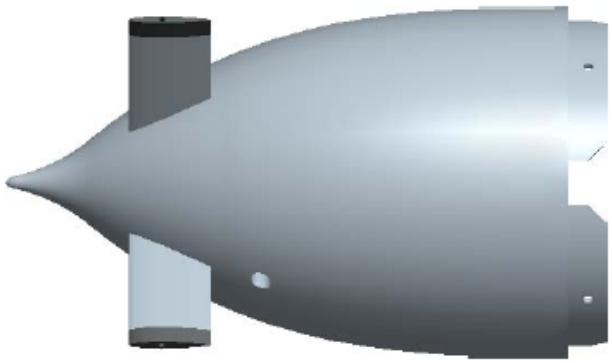

(a)

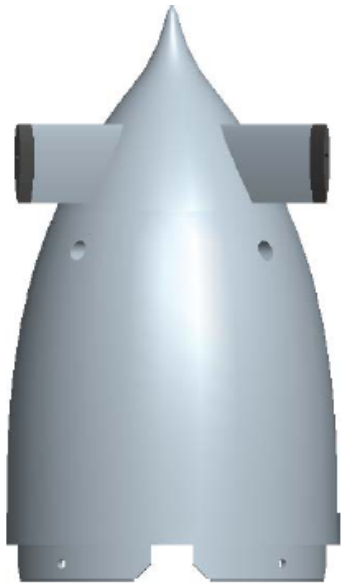

(b)

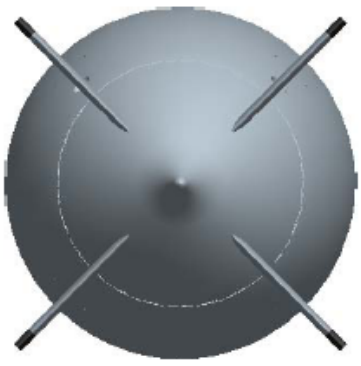

(c)

(d)

Fig. 2.11: CAD Rendering of Contraction Cone (a) Side View (b) Bottom View (c) Front View (d) Back View

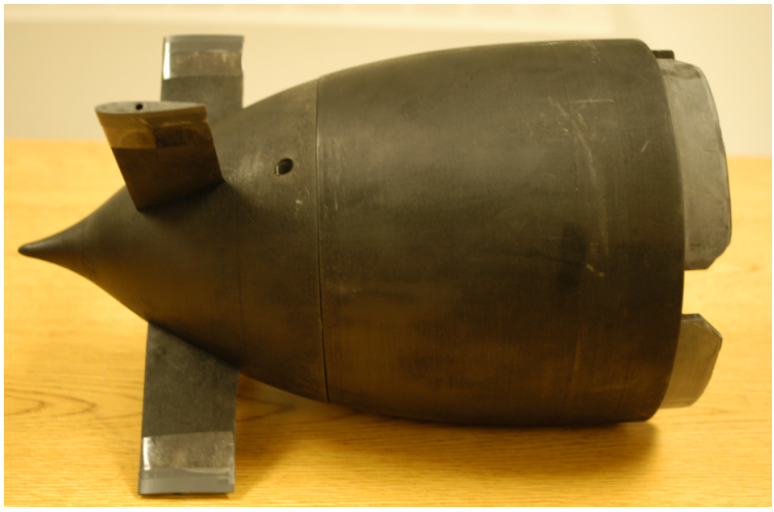

Fig. 2.12: 3-D Printing Model of the Contraction Cone

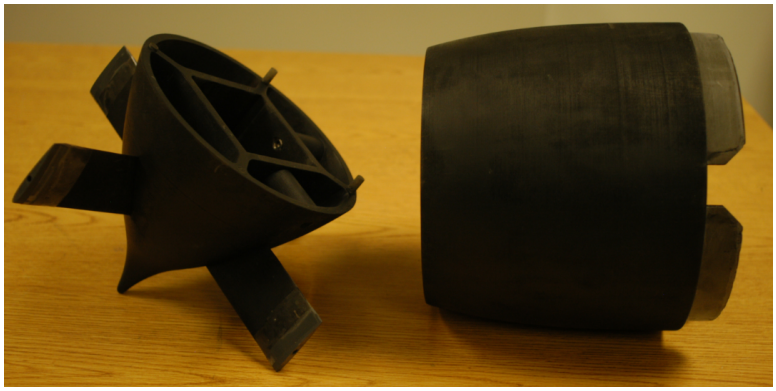

Fig. 2.13: Segmented Contraction Cone Model

Fig. 2.14: Design of the Square Cavity and Set Screw Channel Within the Contraction Cone

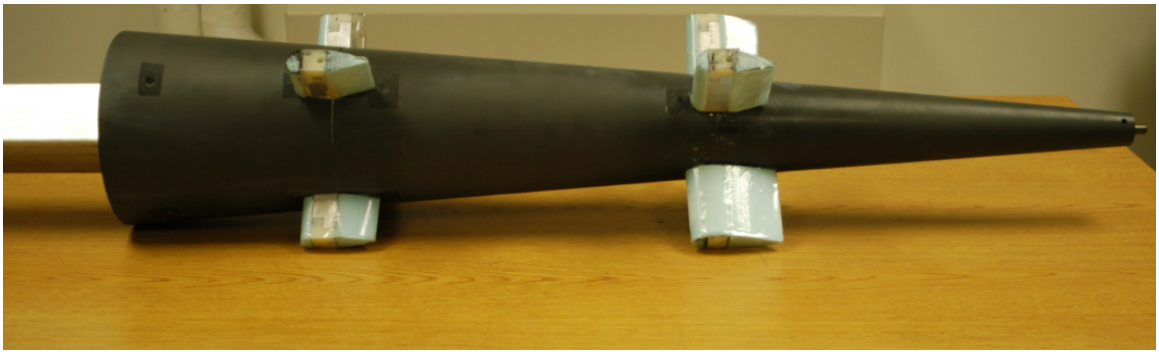

Fig. 2.15: PVC Aft-Body Diffuser with Streamlined Struts

Fig. 2.16: Aft-Body Diffuser Attached with a 3 inch x 3 inch Square Beam

Fig. 2.17: Strut Design on the Aft-Body Diffuser

Fig. 2.18: A Streamlined Strut on the Aft-Body Diffuser

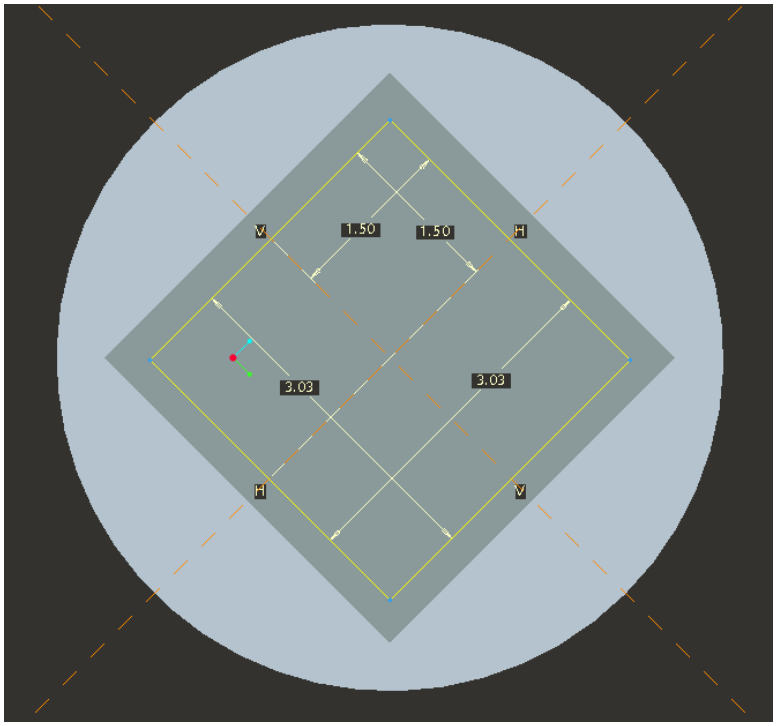

Fig. 2.19: Measurement and Position of the Square Cavity Design in CAD

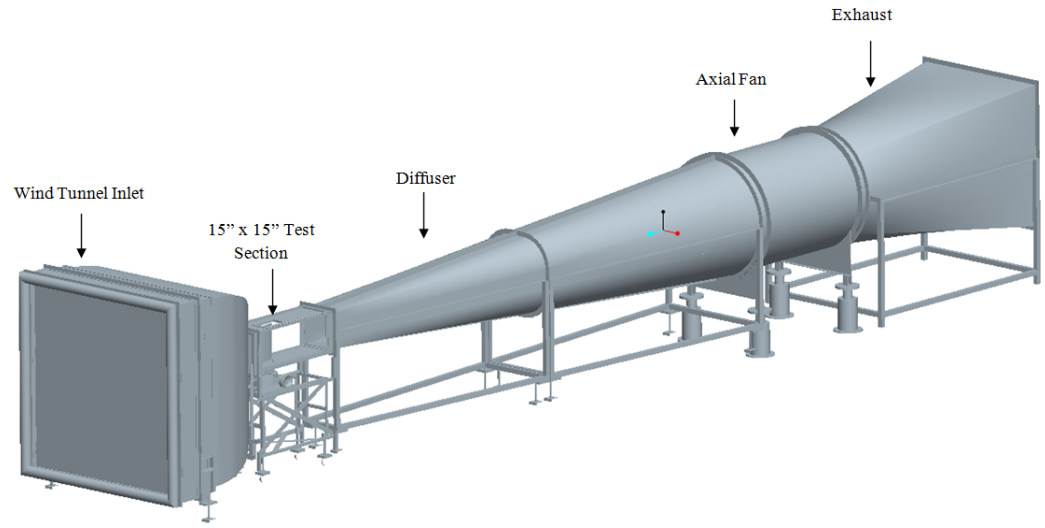

(a)

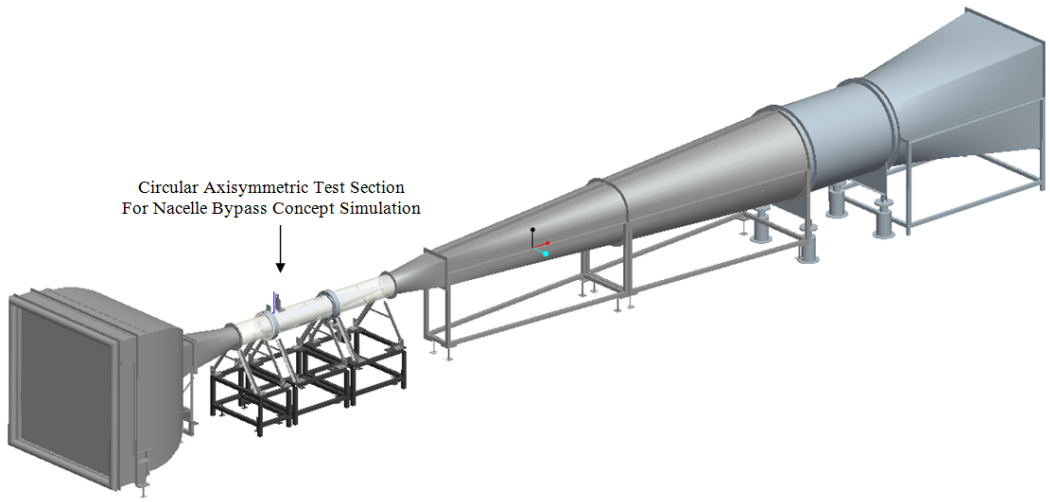

(b)

Fig. 2.20: Modification of a 15 inch by 15 inch Wind Tunnel Facility into a Nacelle Bypass Simulation Facility (a) 15 inch by 15 inch Test Section (b) Circular Axisymmetric Test Section

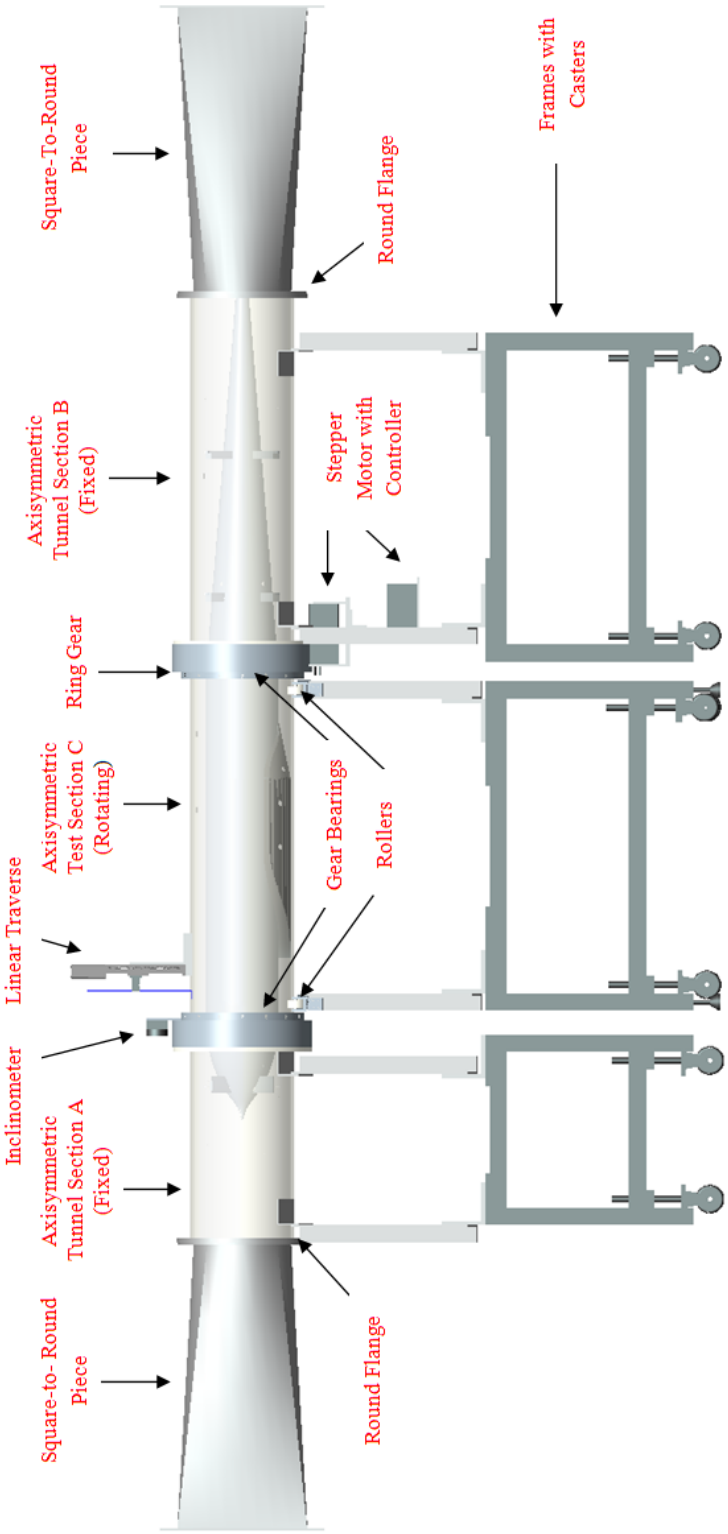

Fig. 2.21: New Axisymmetric Test Section Schematic and Components

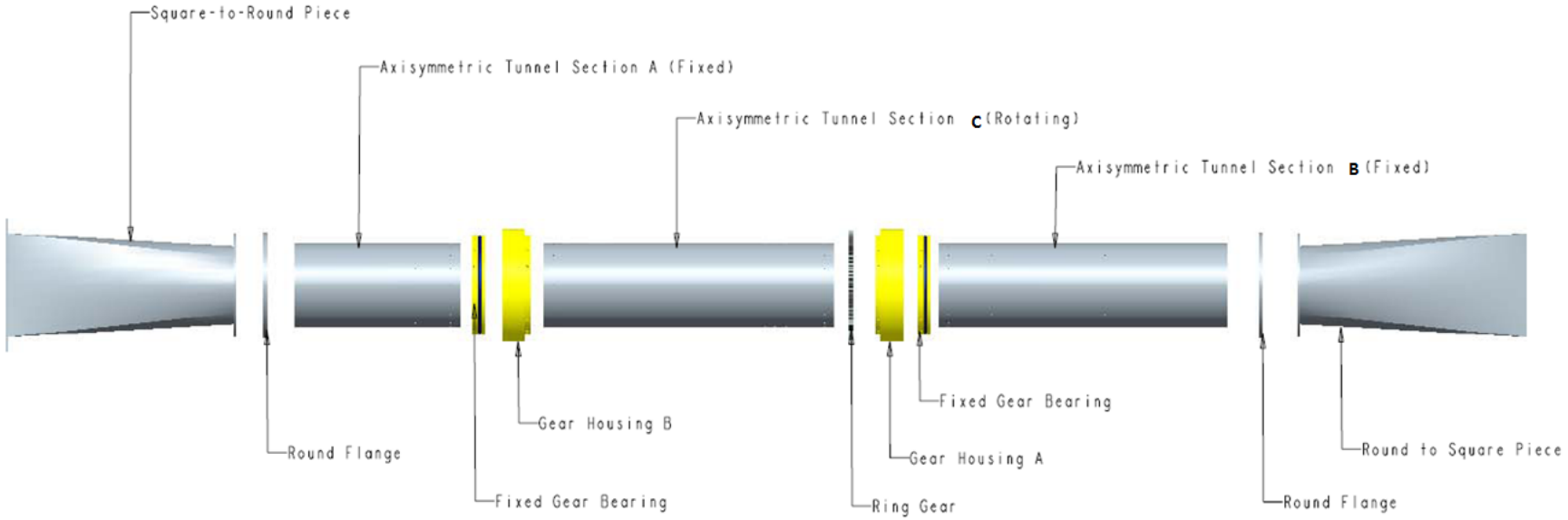

Fig. 2.22: Exploded View of Key Components of the Axisymmetric Test Section

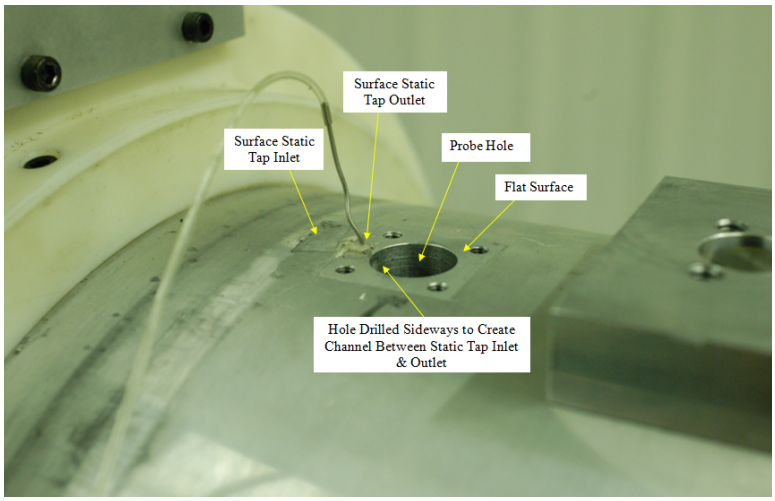

Fig. 2.23: Probe Hole with Machined Flat Outer Surface

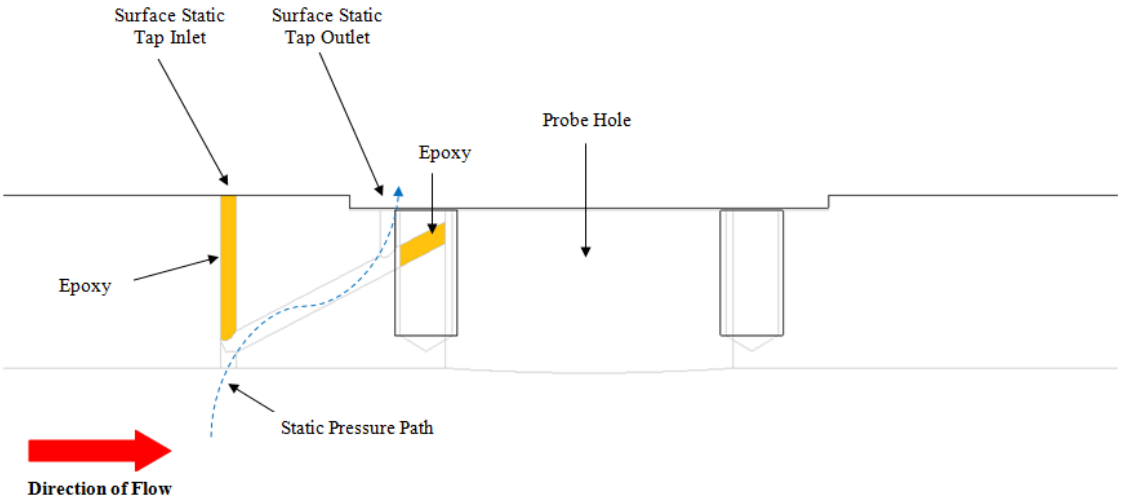

Fig. 2.24: Close Up View of the Rotating Test Section C with Details of the Surface Static Tap Set-Up

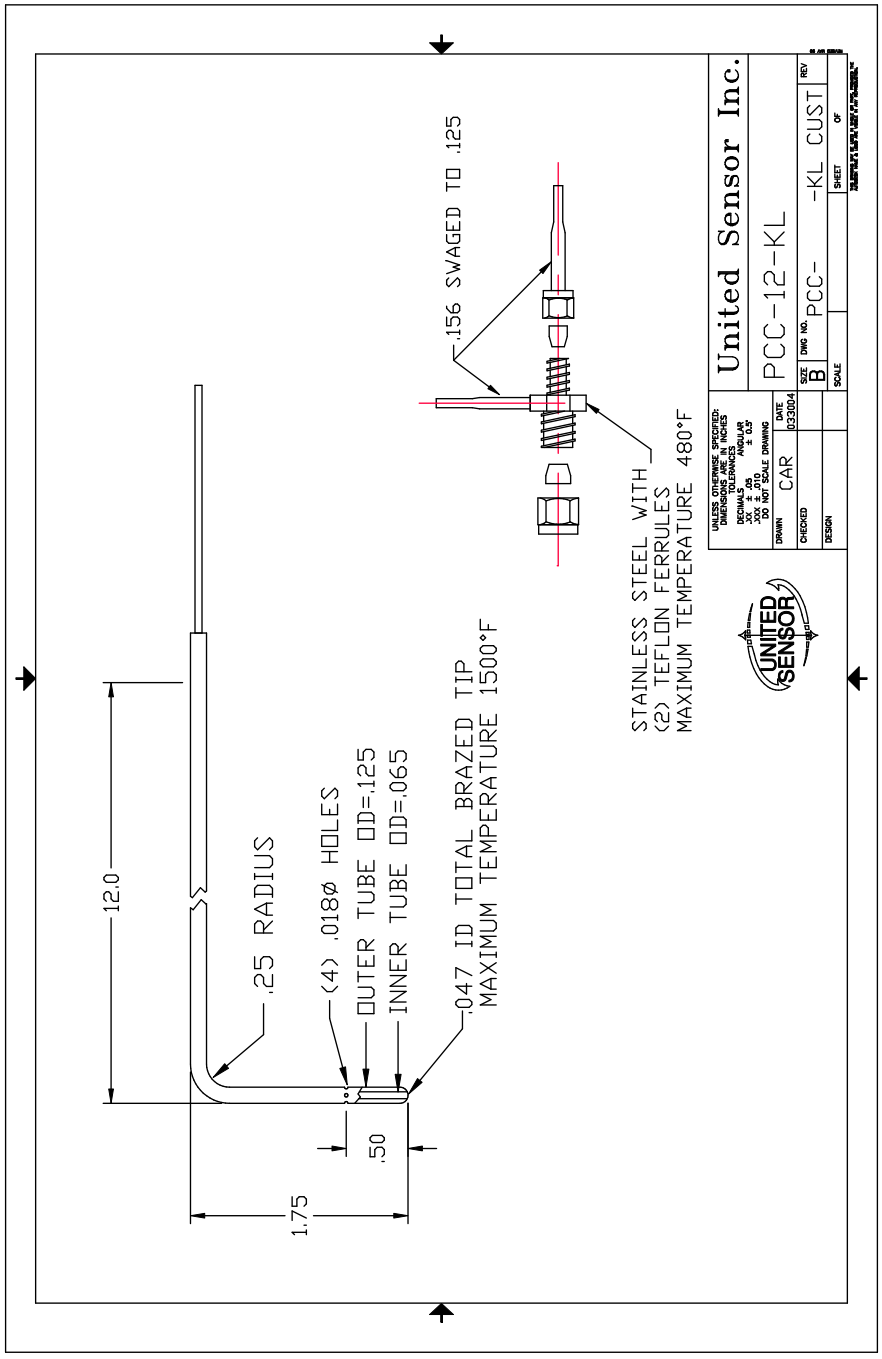

Fig. 2.25: Pitot-Static Probe Used for Pressure Acquisition

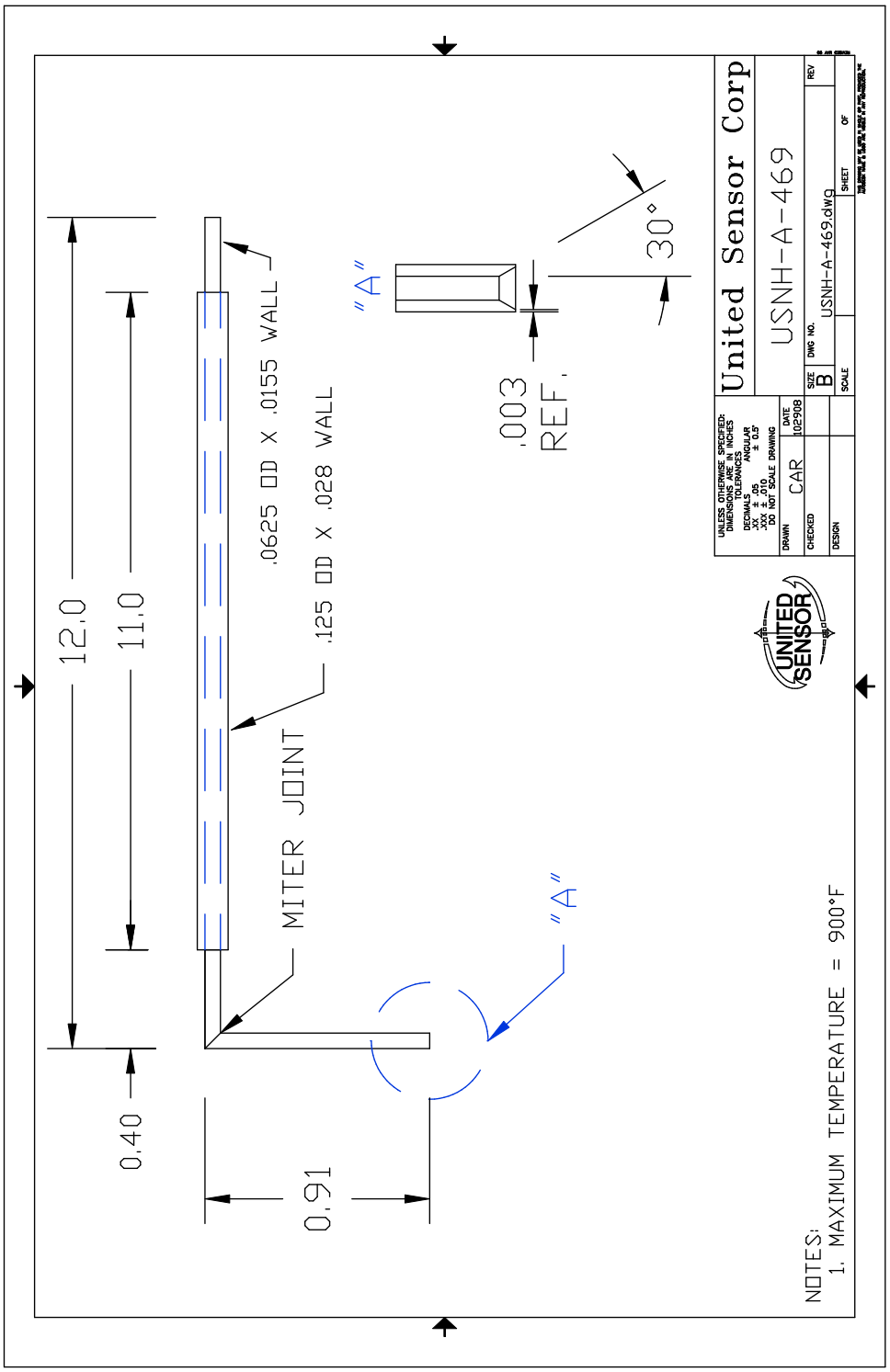

Fig. 2.26: Total-Pressure Probe Used for Pressure Acquisition

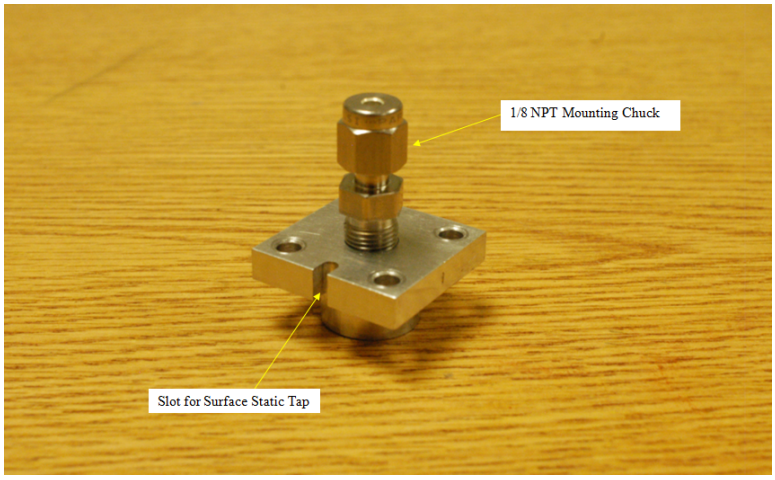

Fig. 2.27: Probe Plug with Slot and 1/8 NPT Mounting Chuck

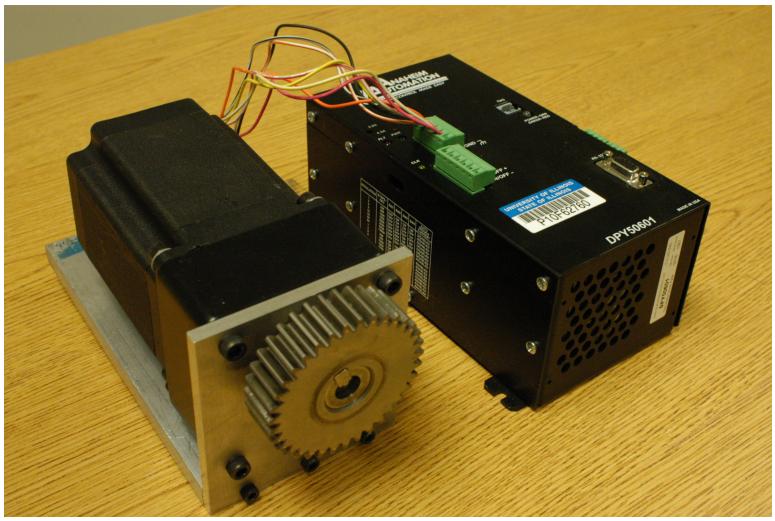

Fig. 2.28: Gear Stepper Motor with Controller

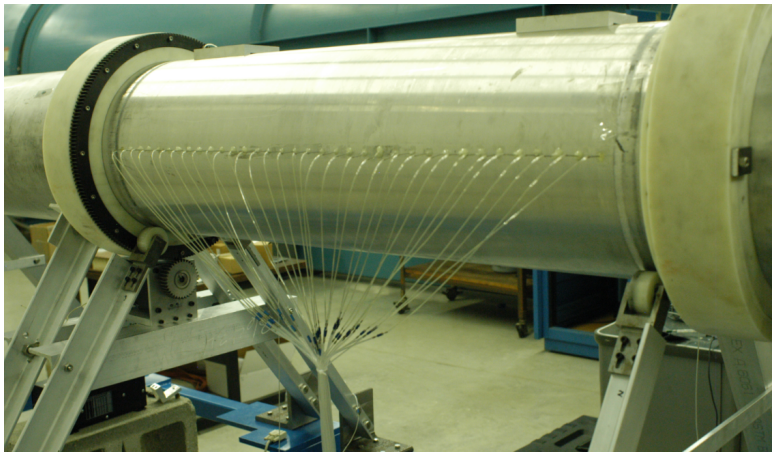

Fig. 2.29: Position of 35 Axial Surface Static Taps on the Rotating Test Section C

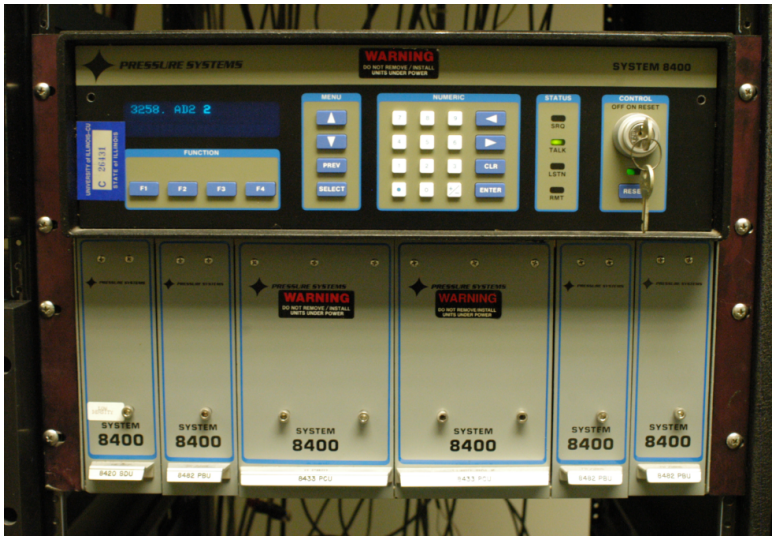

Fig. 2.30: PSI 8400 Pressure Data Acquisition System

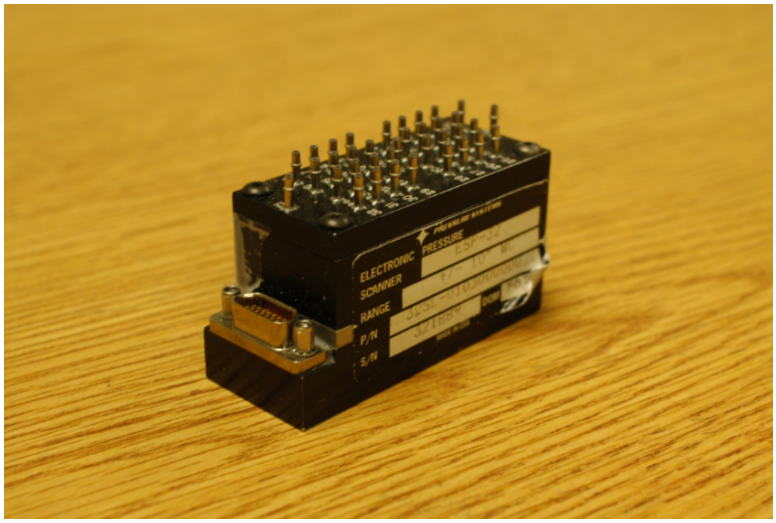

Fig. 2.31: 1 psid Electronically Scanned Module (ESP)

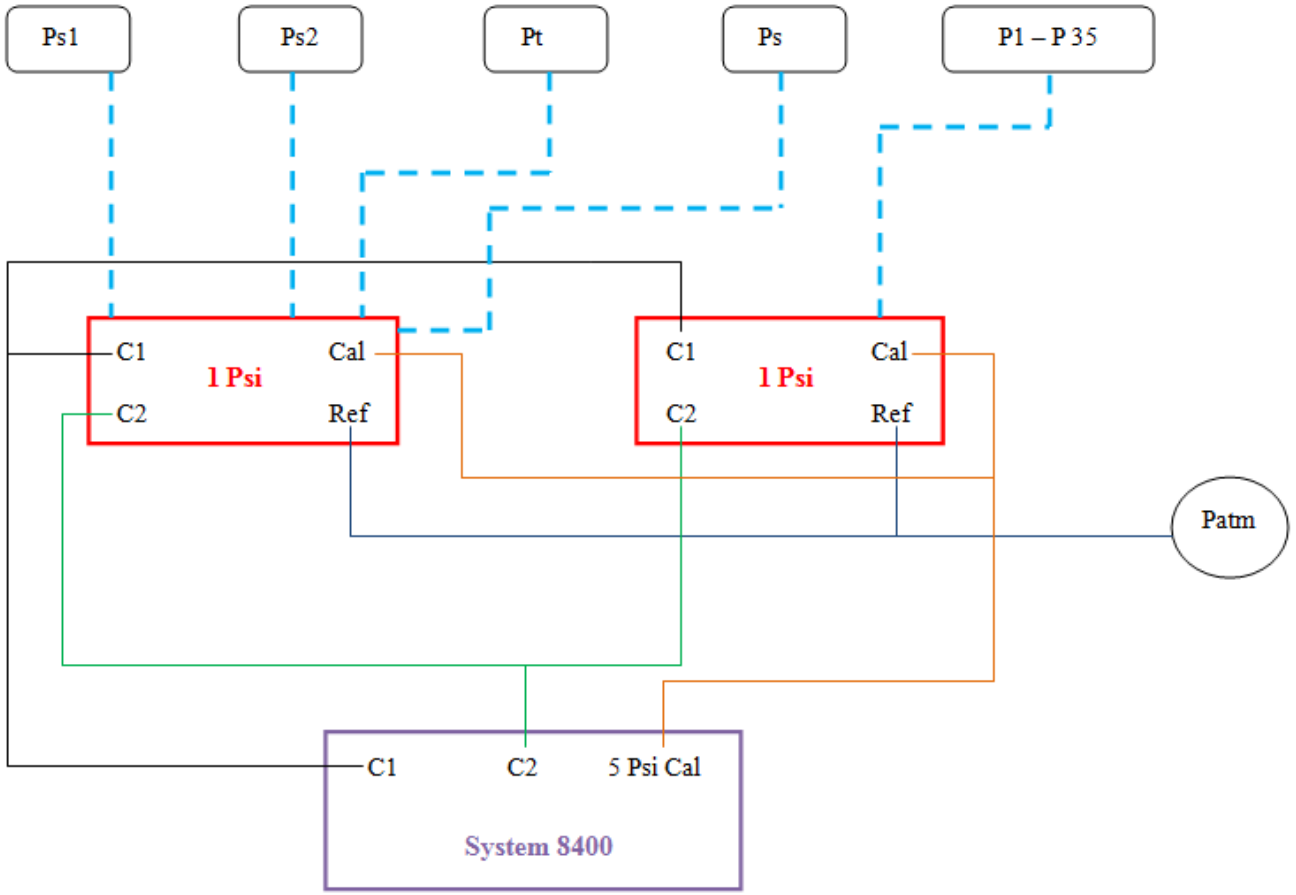

Fig. 2.32: Schematic of the Pneumatic System to Obtain Pressure Measurements

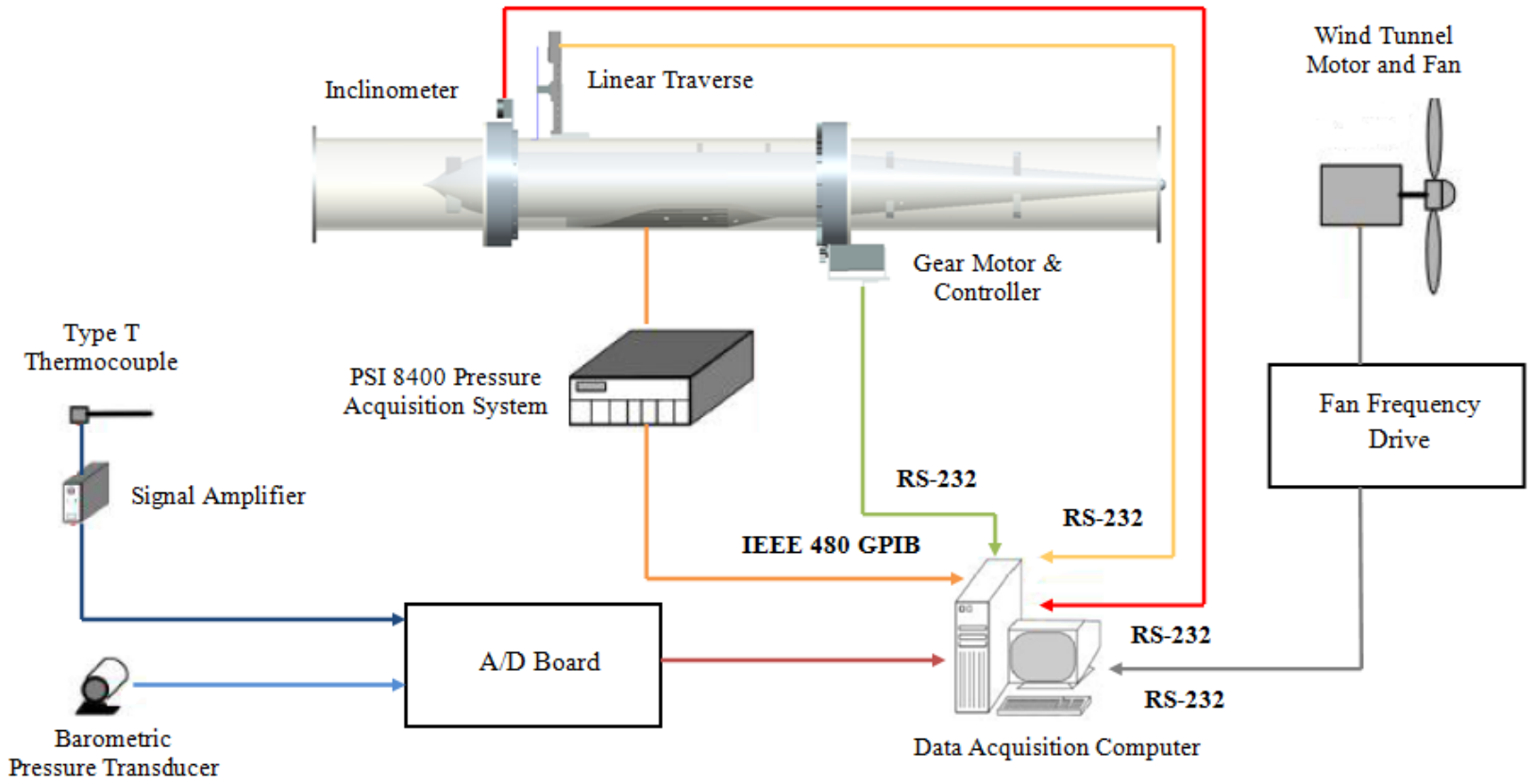

Fig. 2.33: Setup of the Data Acquisition System

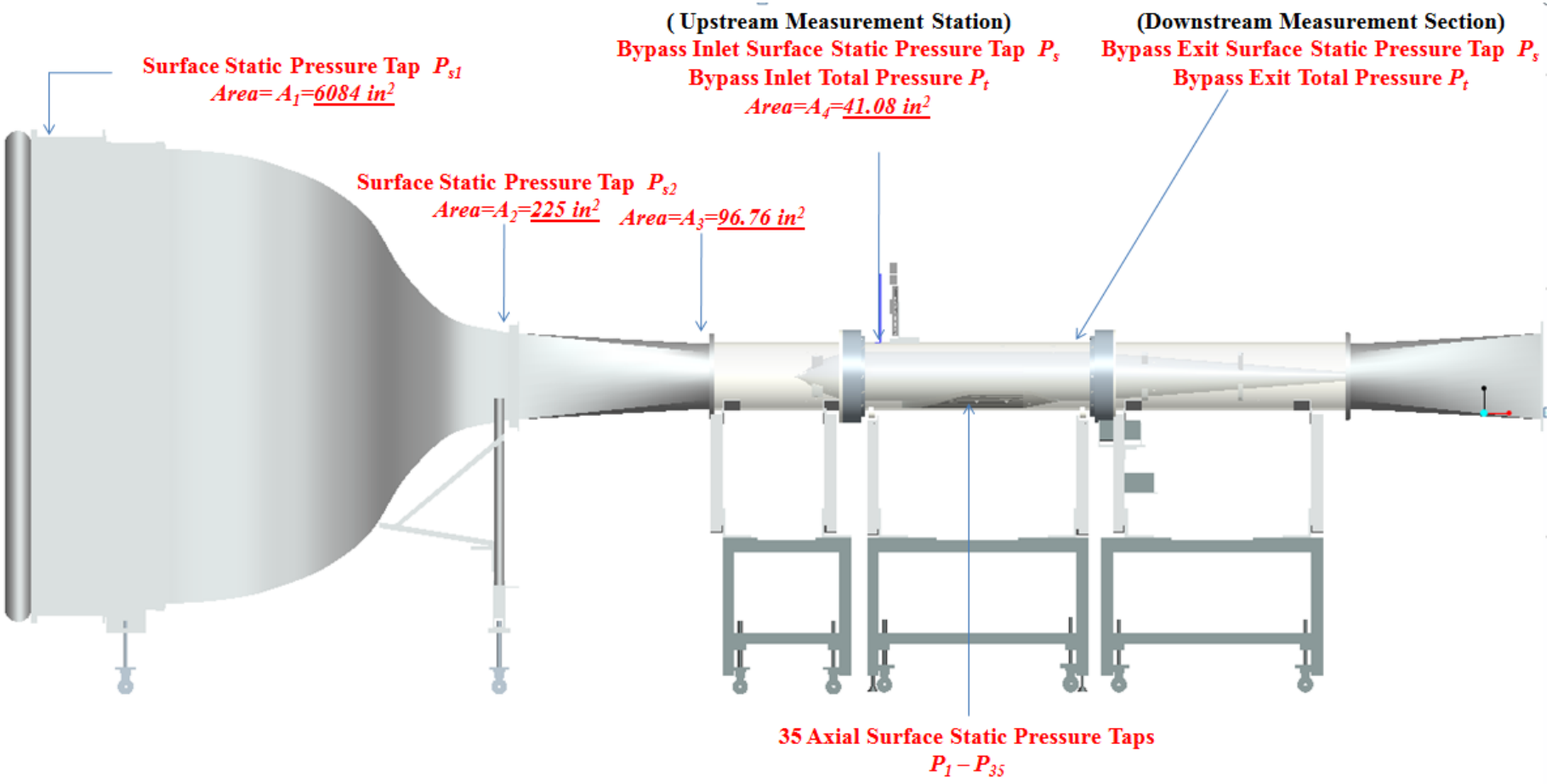

Fig. 2.34: Position and Nomenclature for the Measurement of Pressures on the Bypass Facility

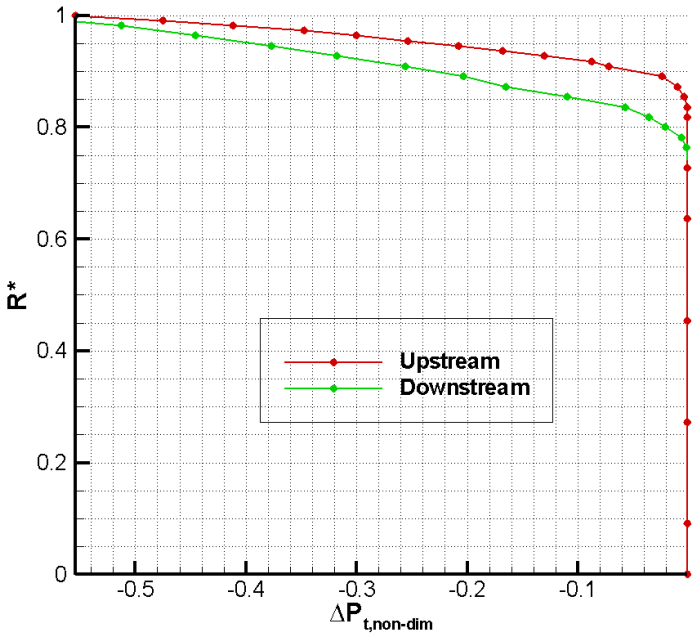

(a)

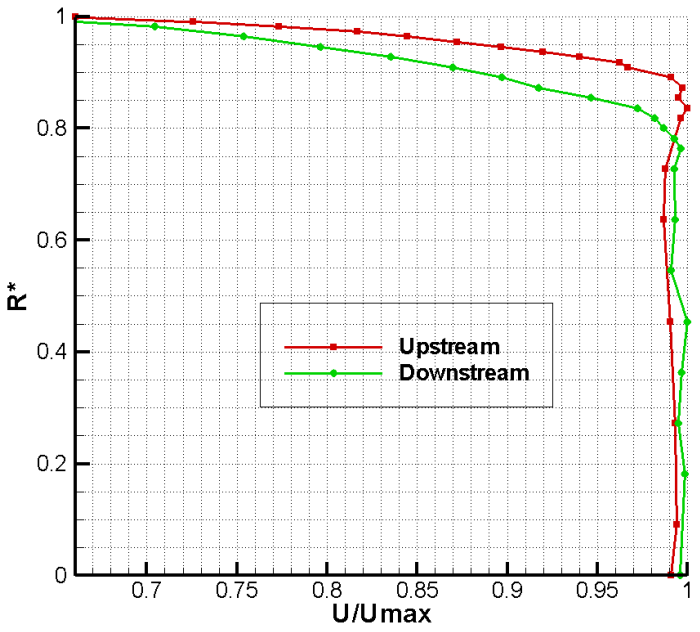

(b)

Fig. 3.1: Comparison of Upstream and Downstream Profiles at 0° for an Empty Wind Tunnel (a) Nondimensional Total Pressure Profile (b) Velocity Profile

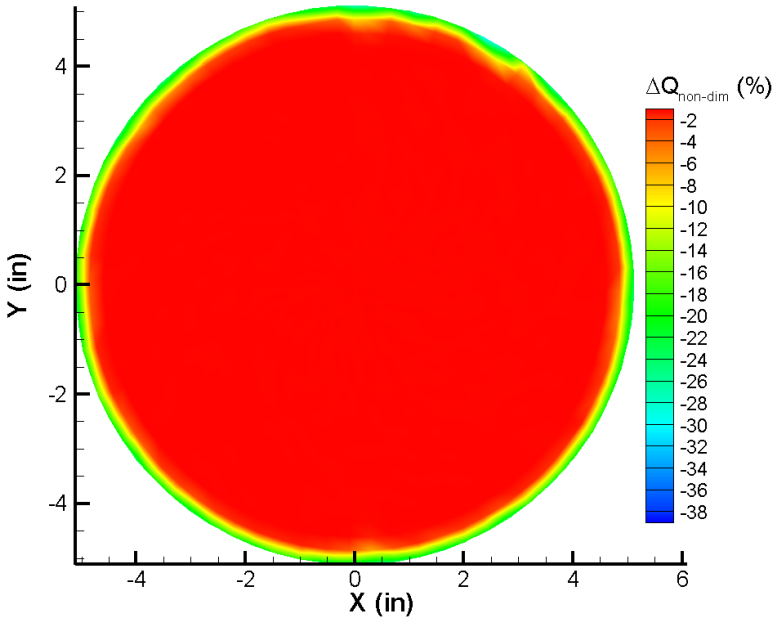

(a)

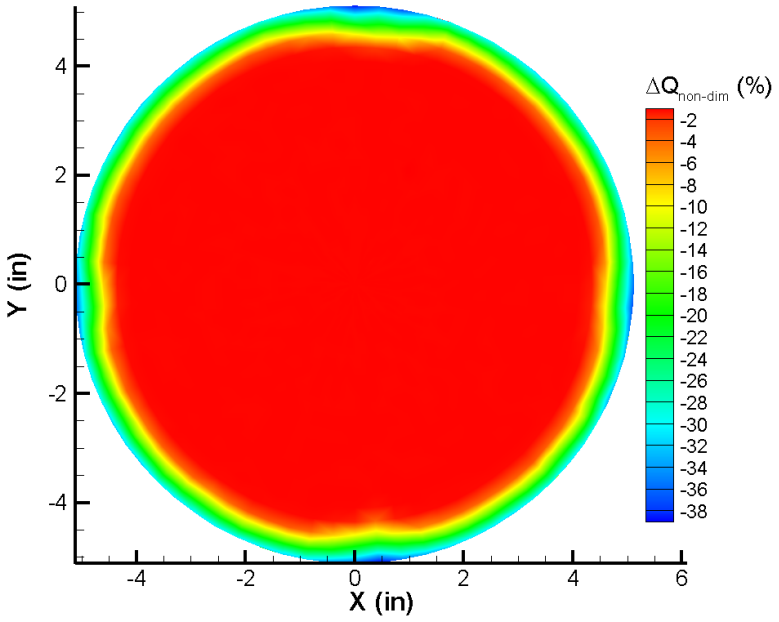

(b)

Fig. 3.2: Percentage Difference in Nondimensionalized Dynamic Pressure(%), between an Empty Wind Tunnel and the Averaged Nondimensionalized Dynamic Pressure at the Core with Identical Scales (a) Upstream Location (b) Downstream Location

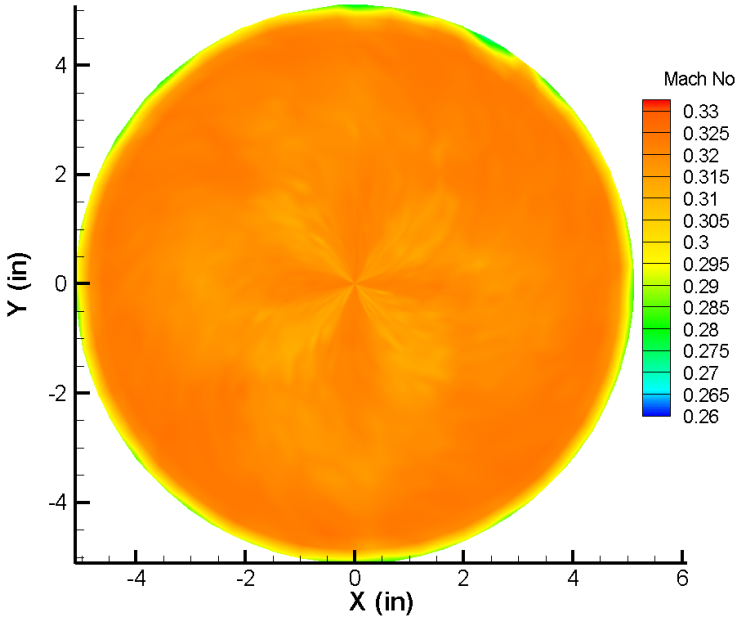

(a)

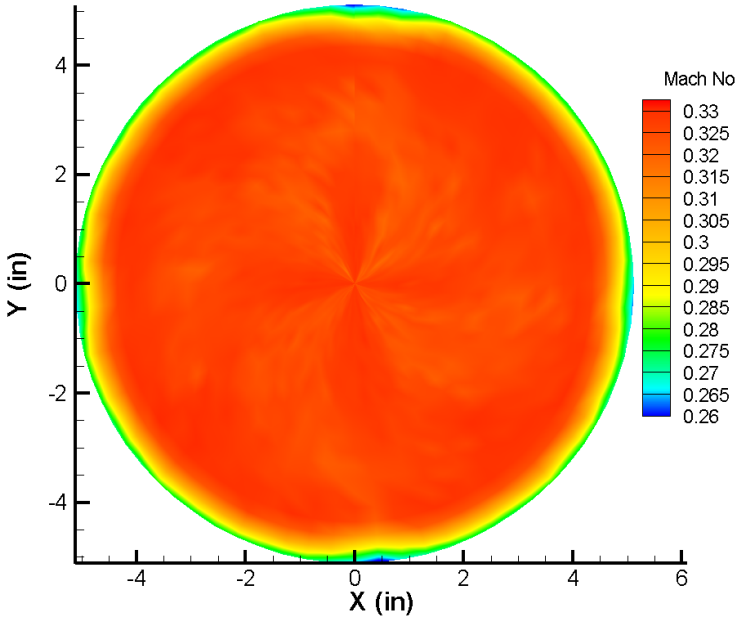

(b)

Fig. 3.3: Mach Number Contour Map of Empty Wind Tunnel with Identical Scales (a) Upstream Location (b) Downstream Location

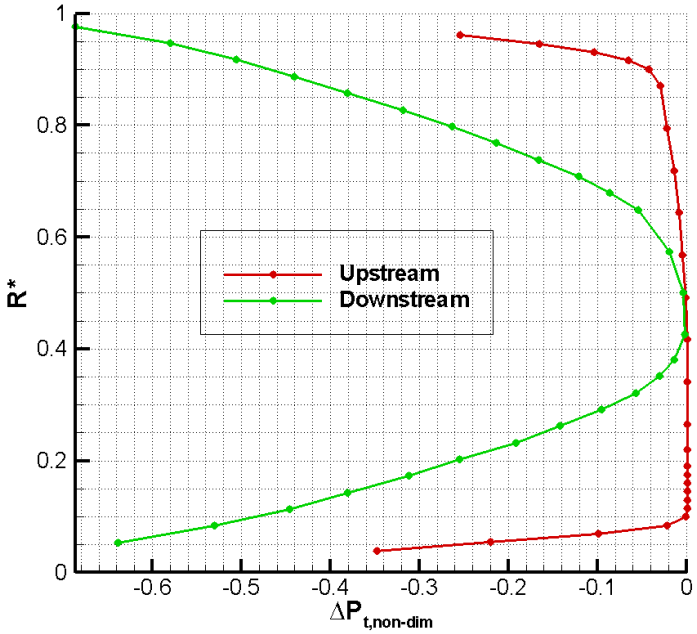

(a)

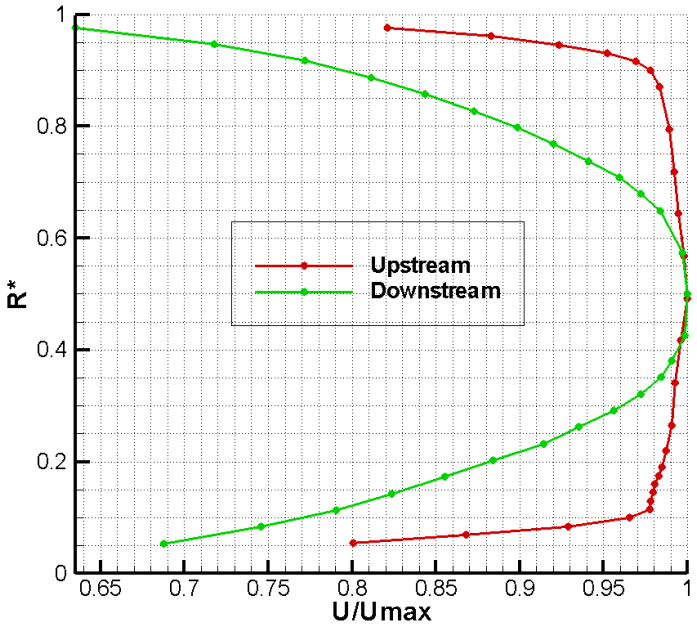

(b)

Fig. 3.4: Upstream and Downstream Profiles at 180° for an Engine Baseline Model (a) Nondimensional Total Pressure Profile (b) Velocity Profile

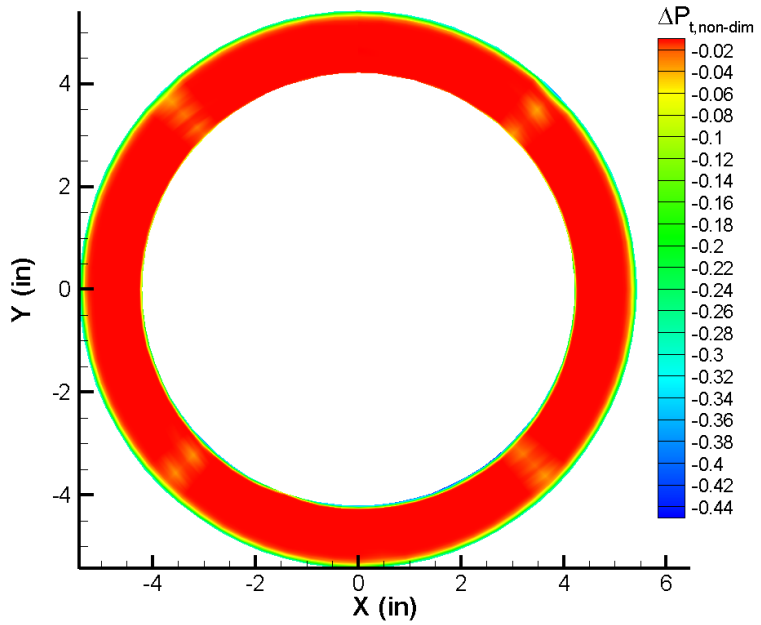

Fig. 3.5: Nondimensional Total Pressure Contour Map for Engine Baseline Model at Upstream Location

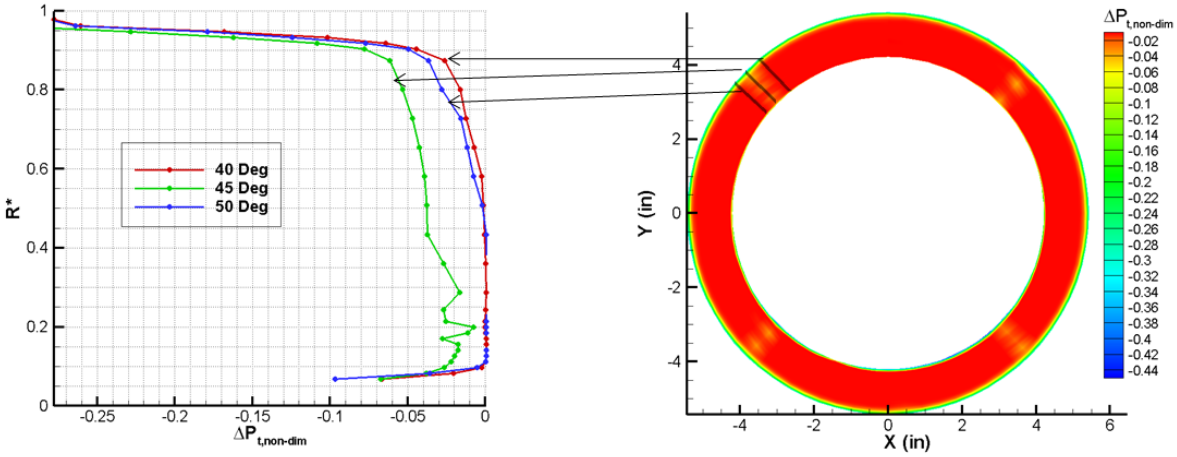

Fig. 3.6: Analysis of Nondimensional Total Pressure Profiles at Regions Close to Support Struts

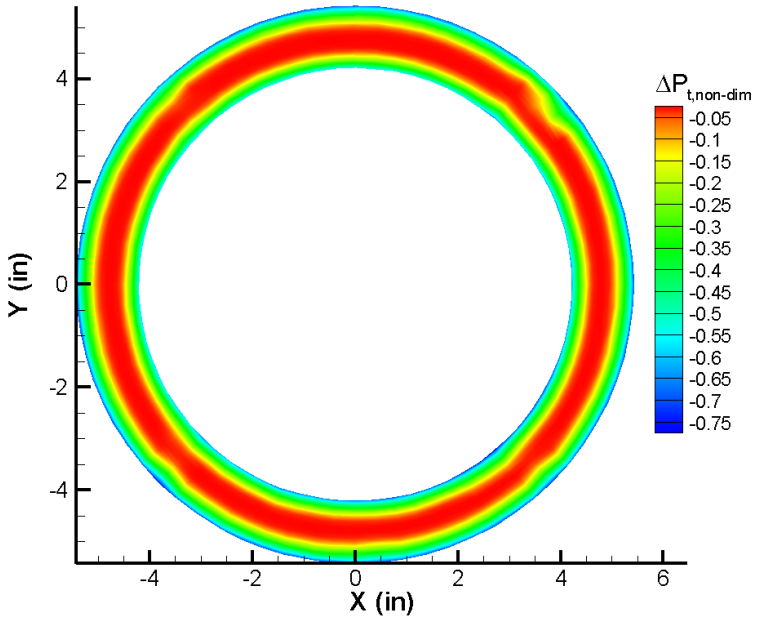

Fig. 3.7: Nondimensional Total Pressure Mapping of Engine Baseline Model at Downstream Location

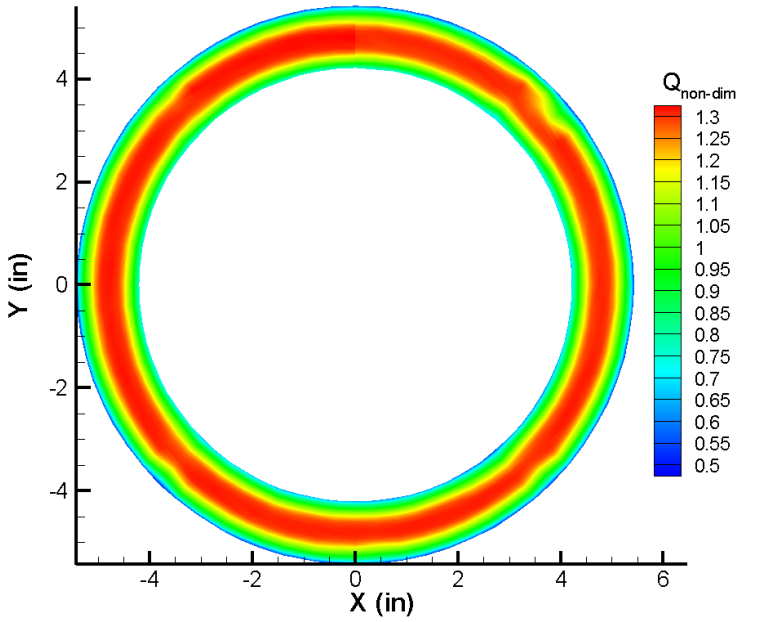

Fig. 3.8: Nondimensionalized Dynamic Pressure Mapping of Engine Baseline Model at Downstream Location

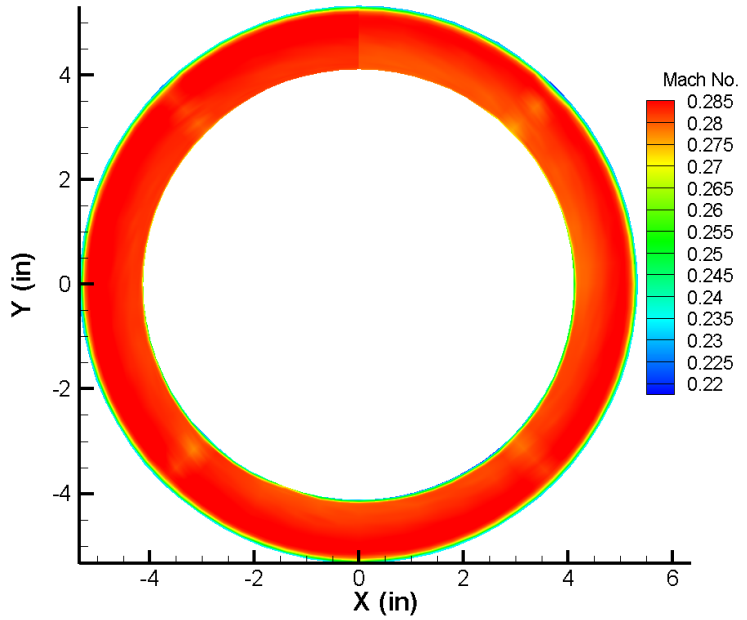

(a)

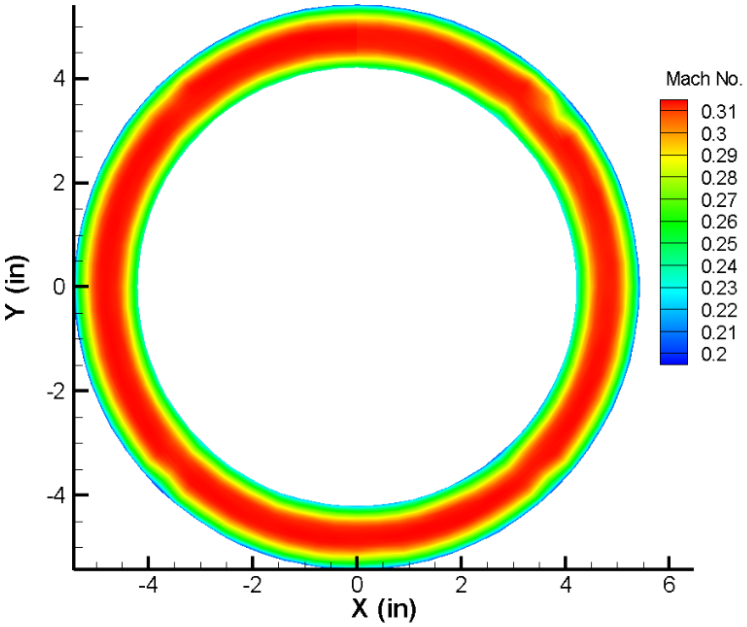

(b)

Fig. 3.9: Mach Number Contour Map of Engine Baseline Model (a) Upstream Location (b) Downstream Location

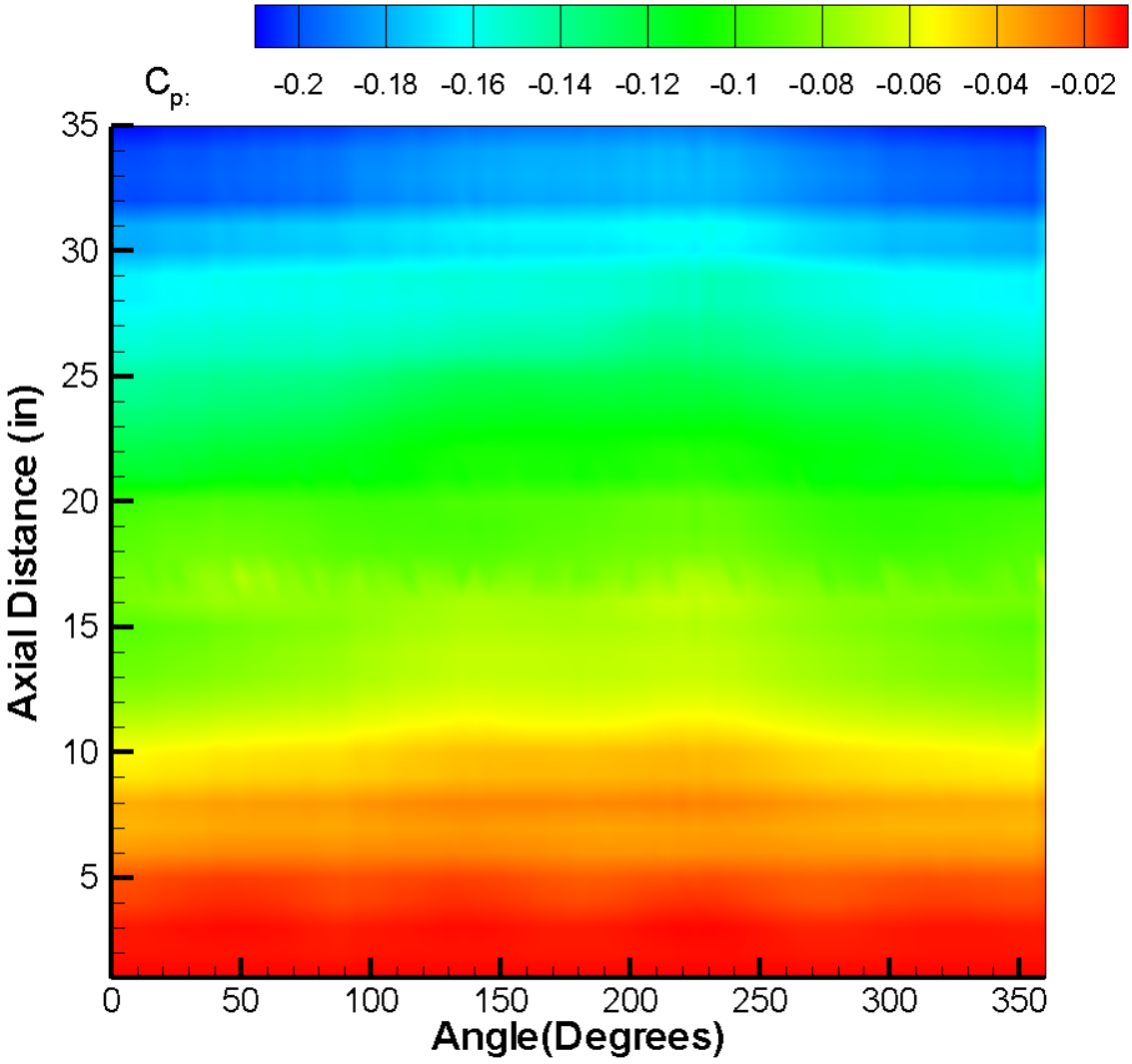

Fig. 3.10: Surface Static Pressure Coefficient Mapping of Inner Tunnel Wall for Engine Baseline Model Configuration

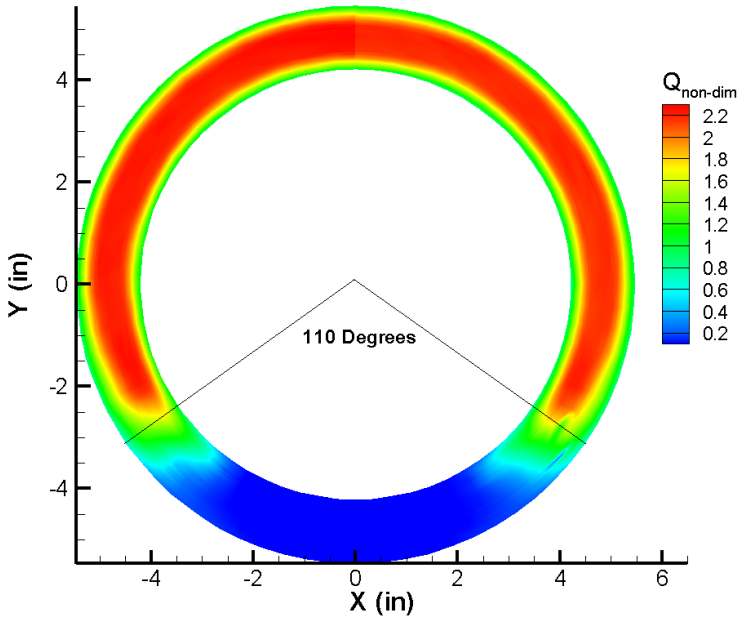

Fig. 3.11: Nondimensionalized Dynamic Pressure Mapping of Engine Baseline Model with Gearbox Fairing at Downstream Location

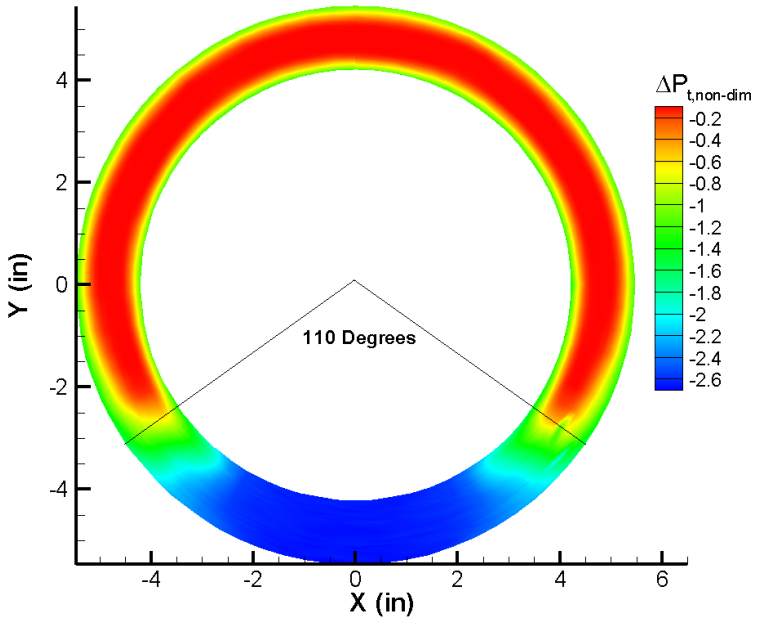

Fig. 3.12: Nondimensional Total Pressure Mapping of Engine Baseline Model with Gearbox Fairing at Downstream Location

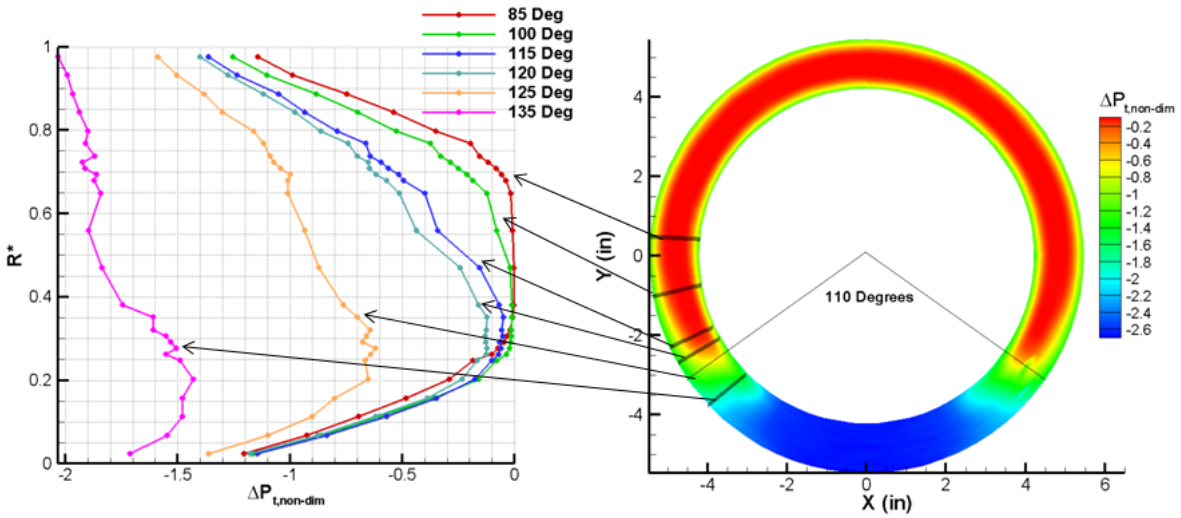

Fig. 3.13: Analysis of Nondimensional Total Pressure Profiles at Regions Close to Gearbox Fairing for Engine Baseline Model with Gearbox Fairing at Downstream Location

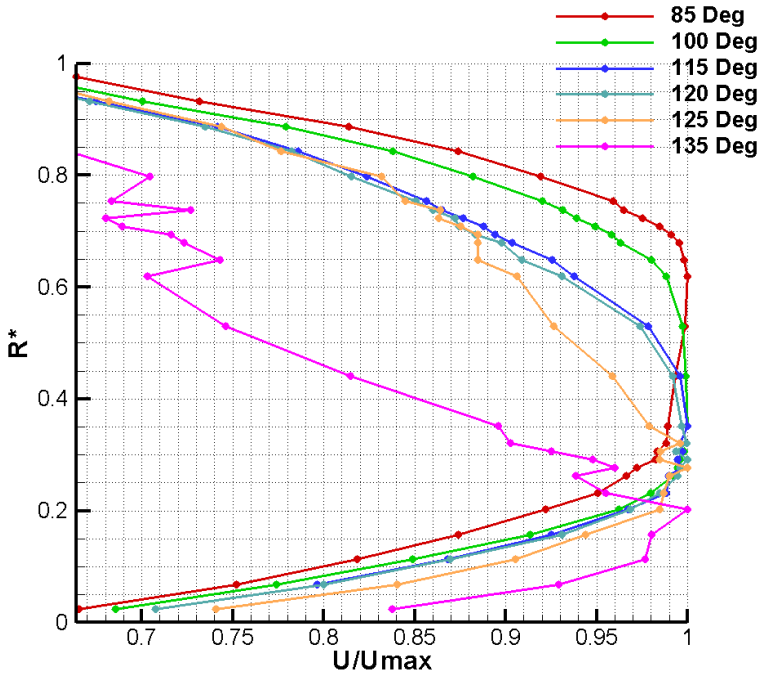

Fig. 3.14: Velocity Profiles for Engine Baseline Model with Gearbox Fairing at Downstream Location

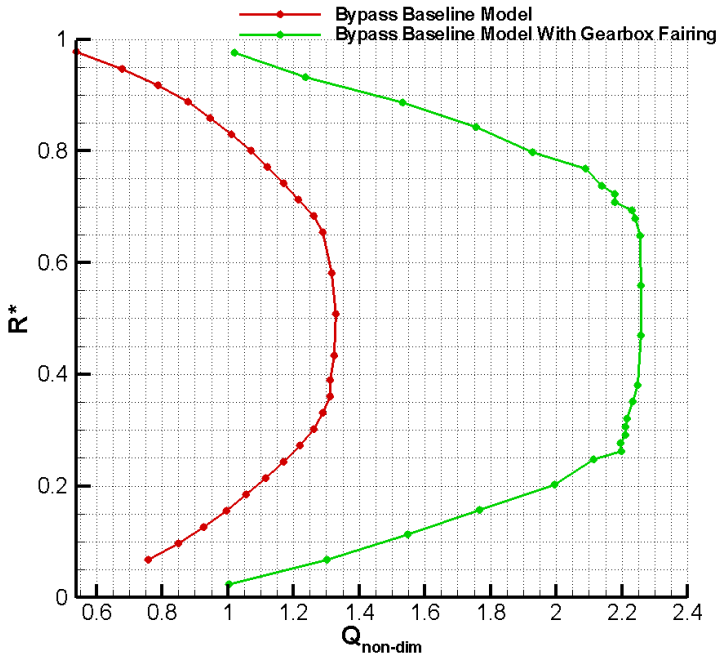

Fig. 3.15: Comparison of Boundary-Layer Profiles for the Cases of Engine Baseline Model With Gearbox Fairing and Without Gearbox Fairing at 0° at Downstream Location

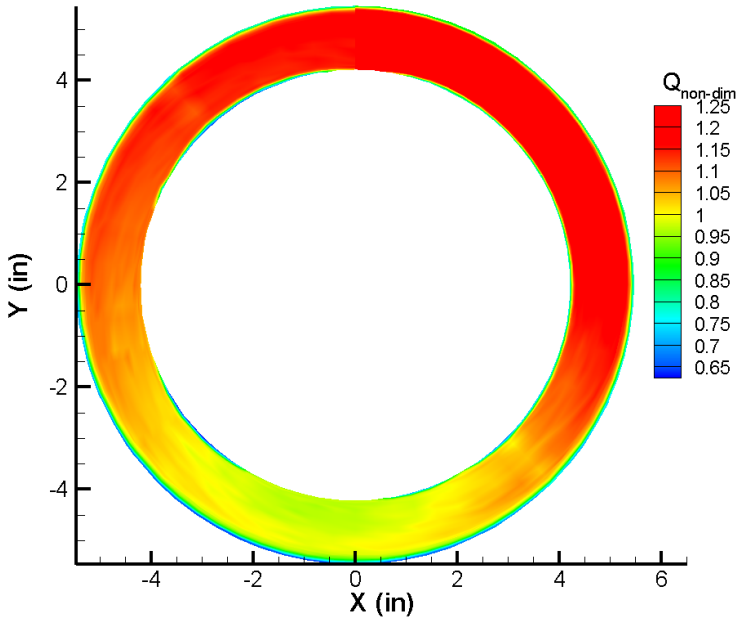

Fig. 3.16: Nondimensionalized Dynamic Pressure Mapping for Engine Baseline Model with Gearbox Fairing at Upstream Location

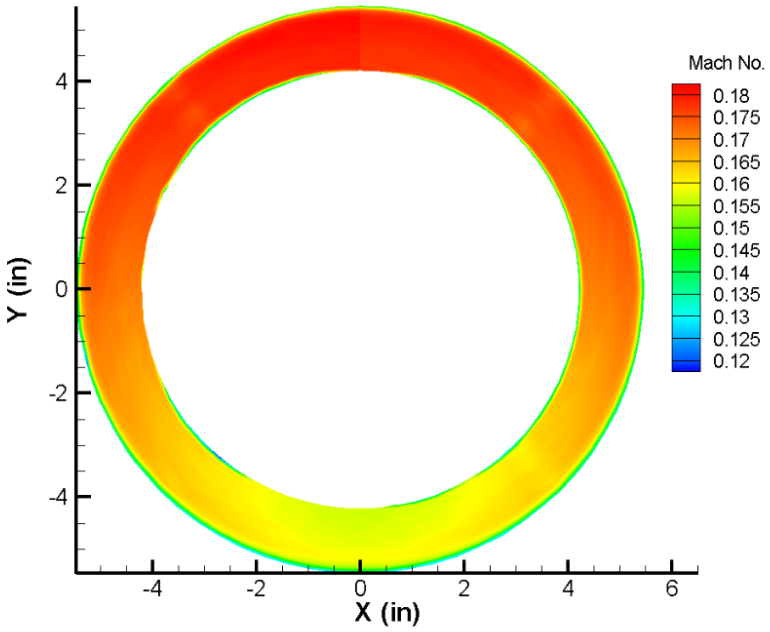

Fig. 3.17: Mach Number Contour Map for Engine Baseline Model with Gearbox Fairing at Upstream Location

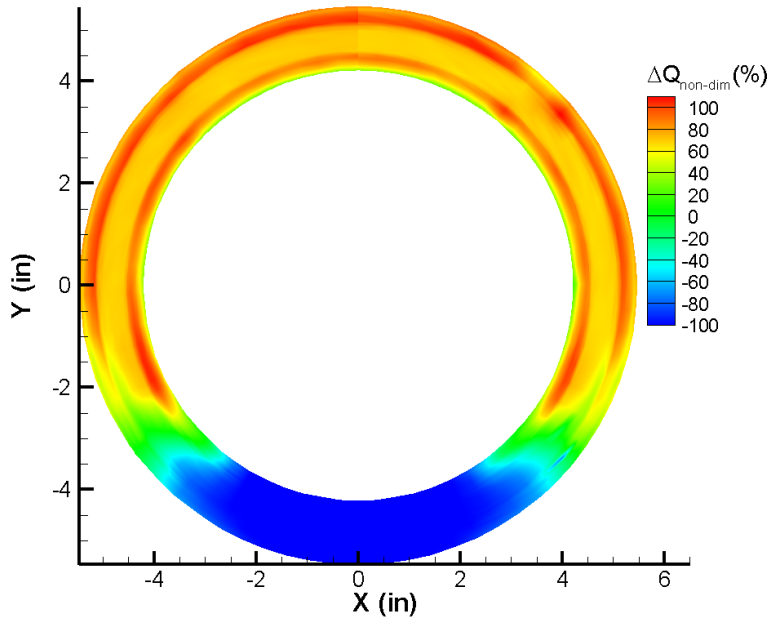

Fig. 3.18: Percentage Difference in Nondimensionalized Dynamic Pressure(%), between an Engine Baseline Model With Gearbox Fairing and Engine Baseline Model Without Gearbox Fairing at Downstream Location

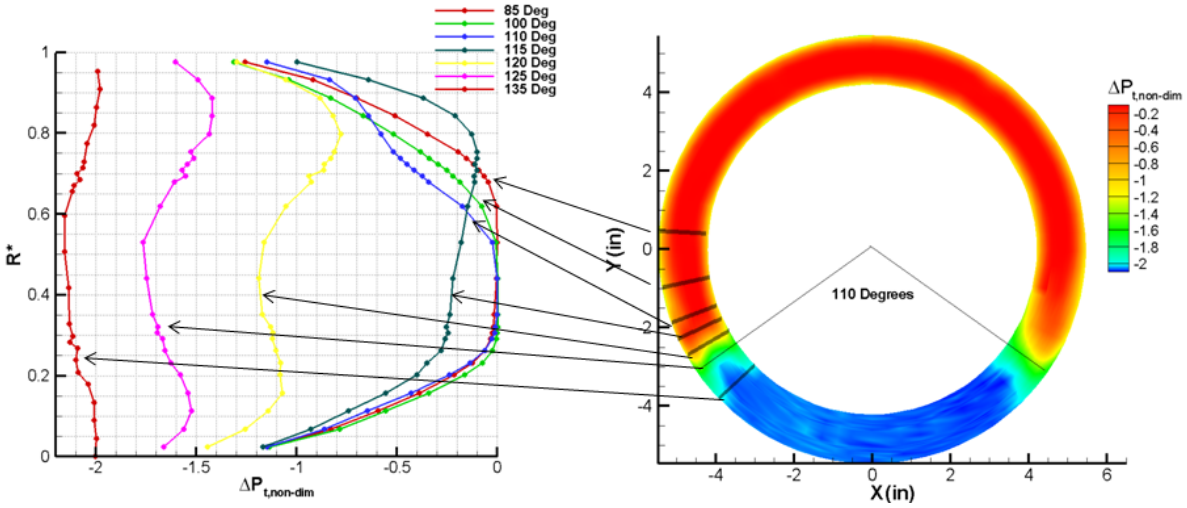

Fig. 3.19: Analysis of Nondimensional Total Pressure Profiles at Regions Close to Gearbox Fairing for Engine Baseline Model without Gearbox Close-Out Fairing at Downstream Location

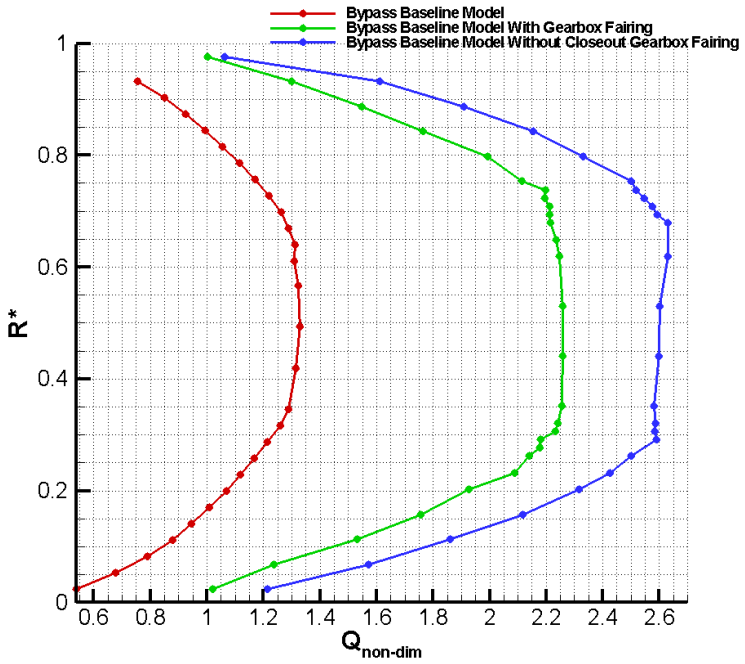

Fig. 3.20: Comparison of Boundary-Layer Profile for the Cases of Engine Baseline Model With, Without Gearbox Fairing and Without Gearbox Close-Out Fairing at 0° Downstream Location

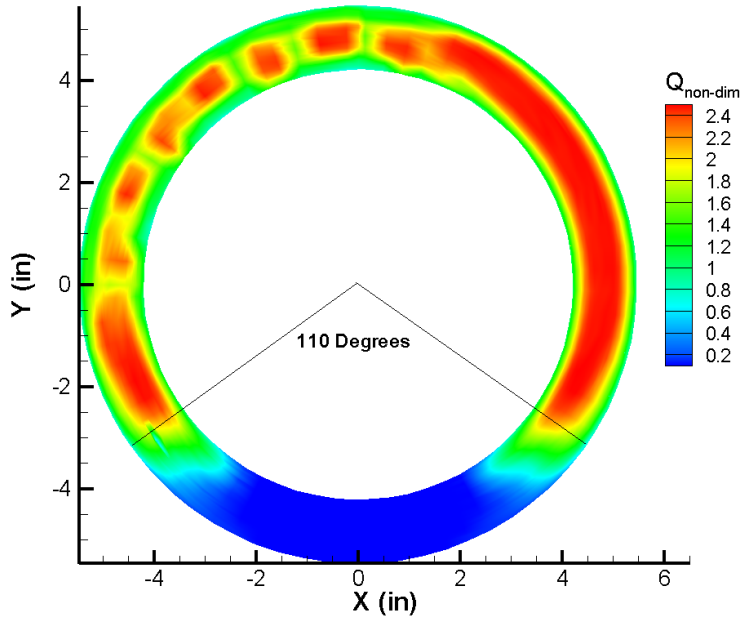

Fig. 3.21: Nondimensionalized Dynamic Pressure Mapping for Engine Baseline Model with Gearbox Fairing and Crane Beams at Downstream Location

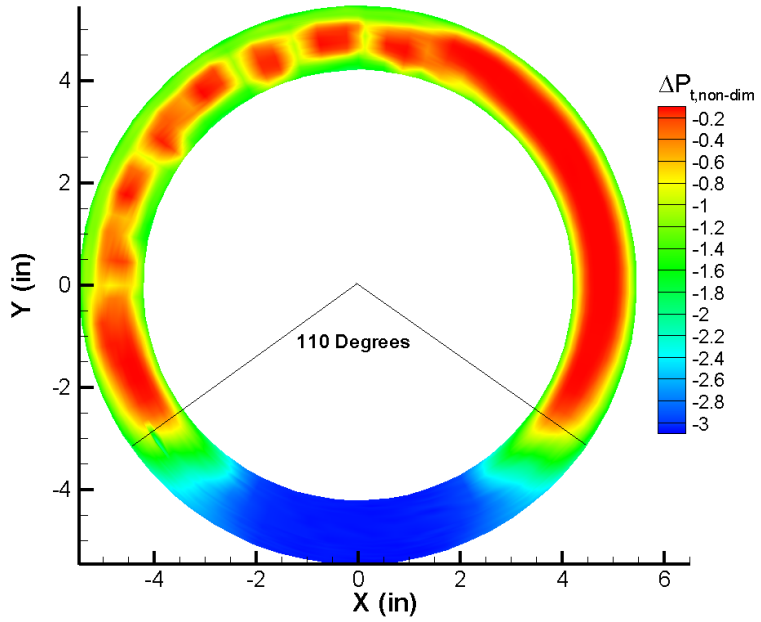

Fig. 3.22: Nondimensional Total Pressure Mapping for Engine Baseline Model with Gearbox Fairing and Crane Beams at Downstream Location

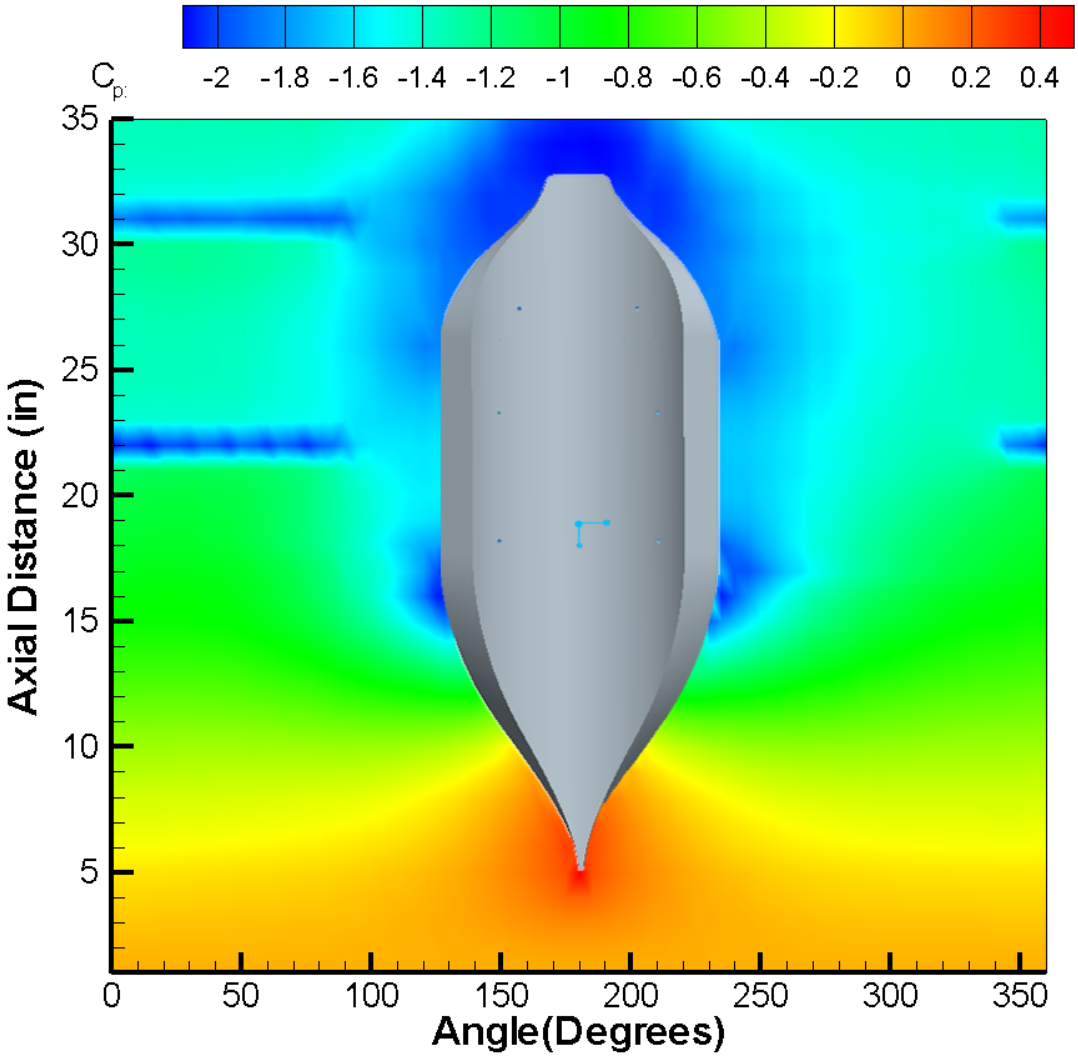

Fig. 3.23: Surface Static Pressure Coefficient Mapping of Inner Tunnel Wall for Engine Baseline Model with Gearbox Fairing and Crane Beams Configuration

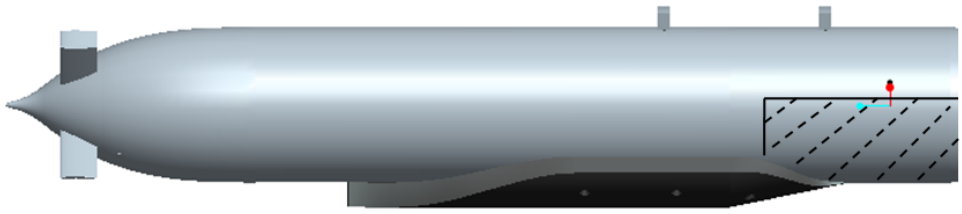

Fig. 3.24: Region of Interest for the Application of Surface Flourescent Oil Flow Visualization for the Test Configuration of Engine Baseline Model with Gearbox Fairing

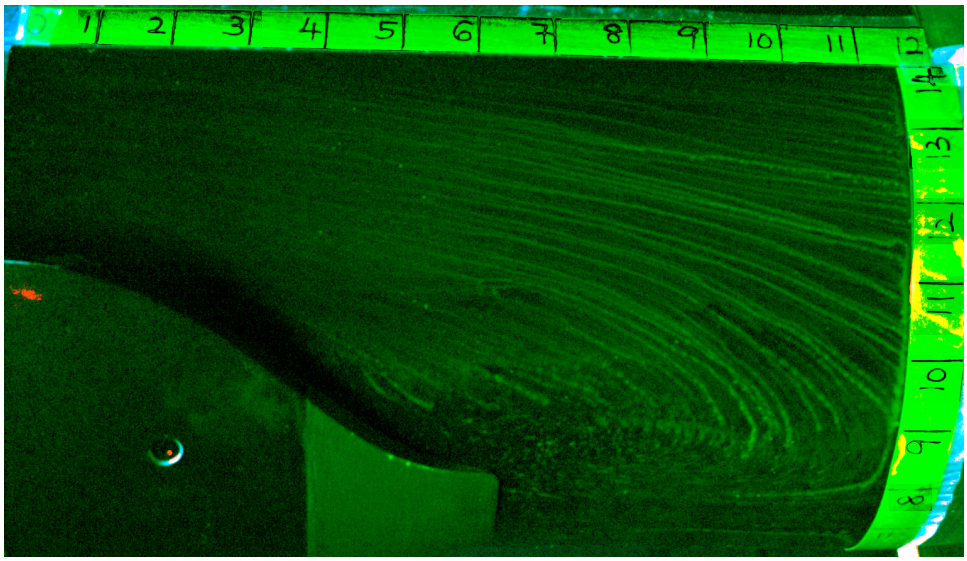

Fig. 3.25: Application of Surface Oil Fluorescent Oil Flow Visualization on Area Behind Close-Out Fairing, 45° From the Centerline of the Model with Flow Direction Moving to the Right

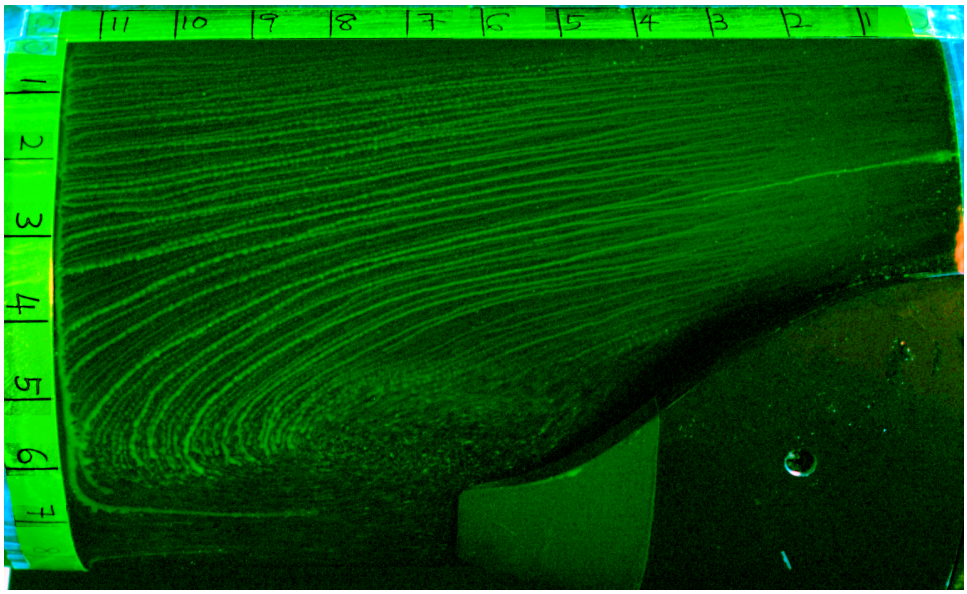

Fig. 3.26: Application of Surface Oil Fluorescent Oil Flow Visualization for Area Behind Close-Out Fairing, 45° From the Centerline of the Model with Flow Direction Moving to the Left

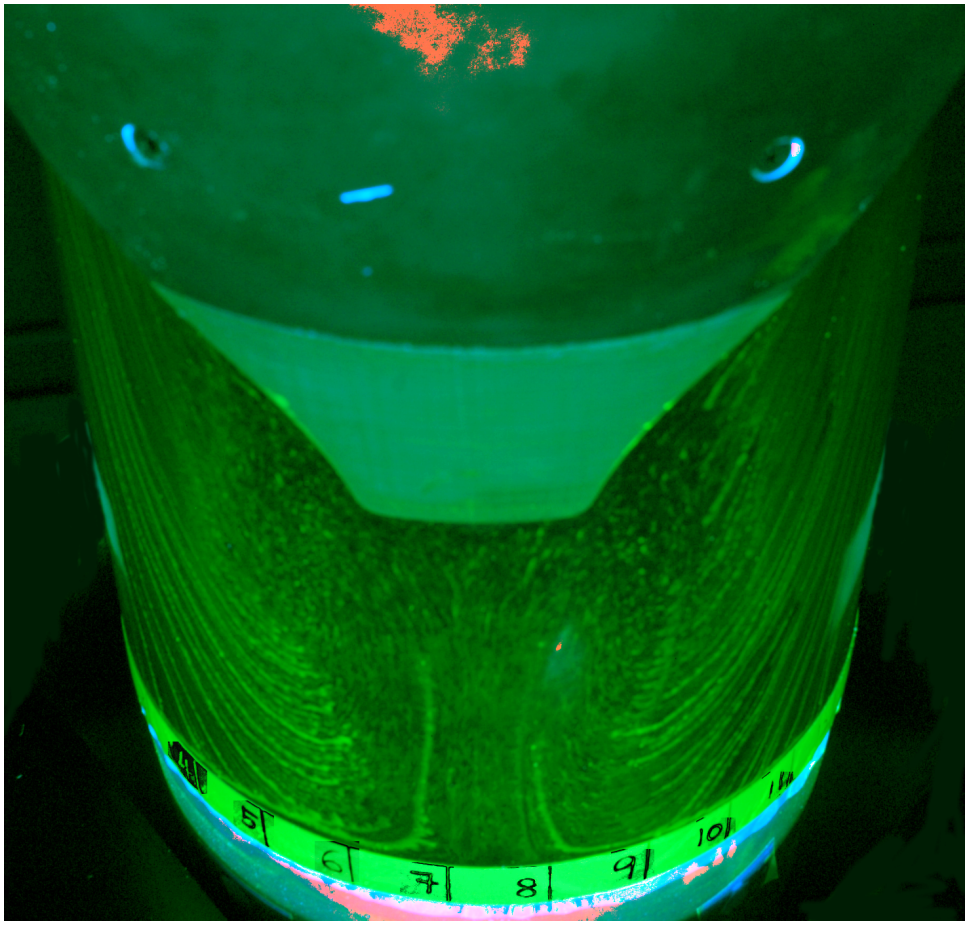

Fig. 3.27: Application of Surface Oil Fluorescent Oil Flow Visualization for Area Behind Close-Out Fairing, 90° Beneath the Close-Out Fairing

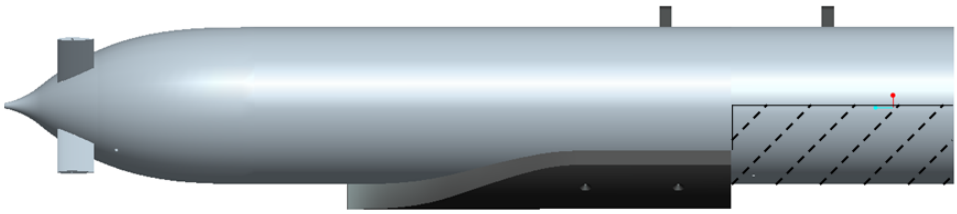

Fig. 3.28: Region of Interest for the Application of Surface Flourescent Oil Flow Visualization for the Test Configuration of Engine Baseline Model without Close-Out Gearbox Fairing

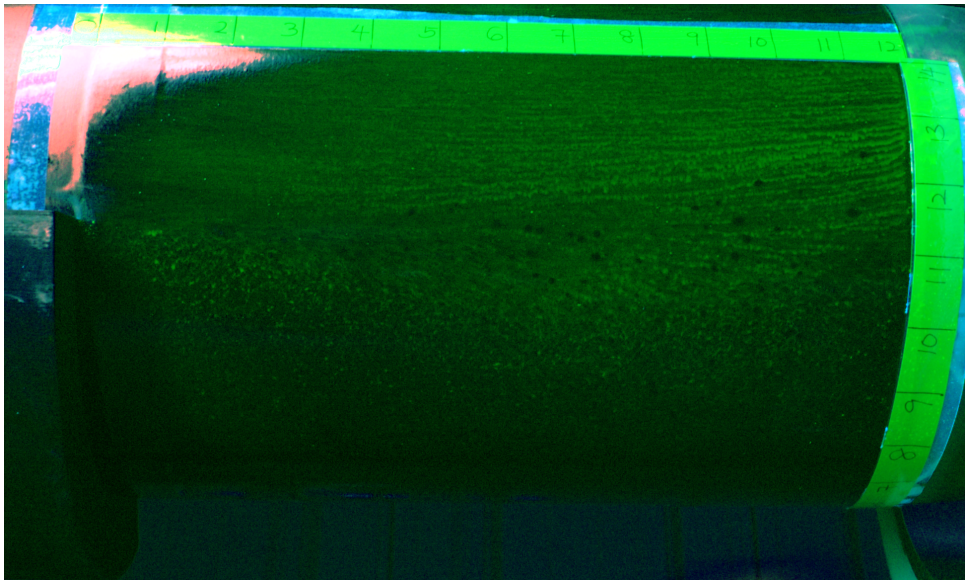

Fig. 3.29: Application of Surface Oil Fluorescent Oil Flow Visualization With Close-Out Fairing Removed, 45° From the Centerline of the Model with Flow Direction Moving to the Right

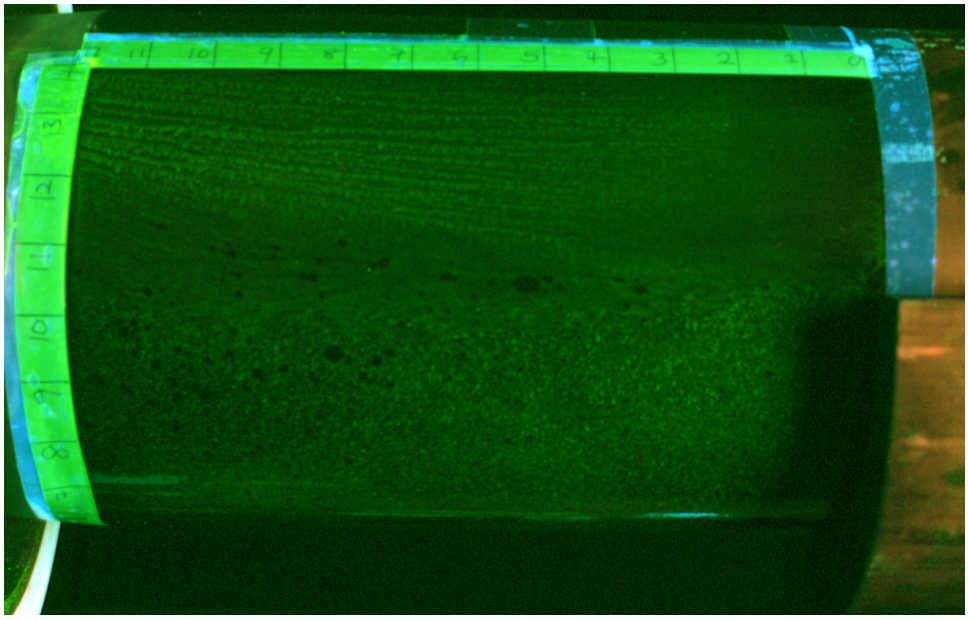

Fig. 3.30: Application of Surface Oil Fluorescent Oil Flow Visualization With Close-Out Fairing Removed, 45° From the Centerline of the Model with Flow Direction Moving to the Left

Appendix A - Design of the Contraction Cone

Morel[20] states that the most important variable in the design of an effective contraction is the contraction ratio (CR) followed by the contour and length of the contraction. These variables control the exit flow uniformity of the contraction as well as flow separation. For the use of the design of an effective contraction, the flow parameters of C_{pe}, C_{pi} and $\tilde{u}$ were defined. These parameters refer to the wall pressure coefficient at point of maximum wall velocity, wall pressure coefficient at point of minimum wall velocity and flow nonuniformity coefficient, respectively. Further information about these coefficients can be found in Morel.[20]

Using a finite difference method, Morel solved the Euler's equation and found that the cubic shape contour produces the lowest wall pressure coefficients and therefore considered it the most suitable for contraction designs for short, non-separated nozzles. The computations were also used to generate design charts for an effective contraction based upon the wall pressure coefficients and the ratio of contraction length and diameter at the contraction inlet, L/D. The desirable range of contraction length and inlet diameter ratios for most nozzles of interest is shown in Eq. A-1

$$0.75 \leq L/D \leq 1.25 \tag{A-1}$$

Based upon the recommendations by Morel, the contraction cone is designed to be two matching cubic ars formed using Eq. A-2 and Eq. A-3.

$$f = 1 - \frac{1}{X^2}\left(\frac{x}{L}\right)^3 \quad x/L \leq X \tag{A-2}$$

$$f = \frac{1}{(1-X)^2}\left(1-\frac{x}{L}\right)^3 \quad x/L > X \tag{A-3}$$

Where x is a specific point on the cubic arc in the longitudinal direction, L is the length of the contraction cone and X is defined as

$$X = X_m/L \tag{A-4}$$

Where X_m is the matching point of the two cubic arcs. A detailed schematic of the cubic arc contour wall and its associated nomenclature can be found in Fig. A.1. Since the contraction cone will be attached in front of the engine baseline model with a fixed diameter of 8.42 inches and installed in a 11.1 inch diameter axisymmetric wind tunnel test section (Section 2.2.1.2), the contract ratio is constrained at 4.14. By following the recommended range of contraction length (L) and inlet diamater (D) ratios as shown in Eq. A-1 and also taking into consideration the constraints from the axisymmetric test section pieces, a value of 1.225 is chosen for the L/D parameter. This fixes the length of the contraction cone at 13.6 inches. Morel's contraction design chart for a CR of 4 in Fig. A.2 was then used to predict the flow quality in and out of the contraction inlet and outlet based upon the chosen L/D value. To avoid flow separation at the contraction inlet and outlet, Morel recommended values of C_{pi} and C_{pe} of less than 0.5 and 0.06, respectively. Flow nonuniformity, $\tilde{u}$ should also be less than 2%. It can be observed that by designing the cubic arc matching point X to be at 0.25, the values of C_{pi} and C_{pe} are approximately 0.075 and 0.01, respectively, with a flow nonuniformity of less than 1%. These values are significantly less than Morel's separation values.

To further evaluate the design of the contraction, a commercial computational fluid dynamics (CFD) package, FLUENT was used to analyze the flow in and out of the contraction. The 2-D computational domain and the mesh generated for the CFD analysis is shown in Fig. A.3. As shown in that figure, the set-up of the computational problem was based upon the installation of the contraction cone in a wind tunnel test section, therefore, the flow outlet will be the annular bypass inlet. Due to symmetry, the problem was set-up in a half plane. The flow inlet was also extended 5 inches forward from the contraction inlet to

allow flow to develop before entering the contraction region. The entire domain consists of 4061 nodes with a total of 3900 quadrilateral cells. The Reynolds Stress Turbulence Model (RSM) with enhanced wall treatment and pressure gradient effects was used. Atmospheric pressure and the pressure drop required to achieve a Mach 0.4 flow was specified at the inlet and outlet boundary conditions, respectively. Results show that the flow increases in speed within the contraction region smoothly with no significant total pressure losses other than close to the contraction and tunnel walls near the exit where boundary layers have started to develop. This is shown in Fig. A.4 and Fig. A.5 respectively. No flow separation was observed. The velocity profile at the end of the contraction as plotted in Fig. A.6 also indicates that the flow is very close to uniform.

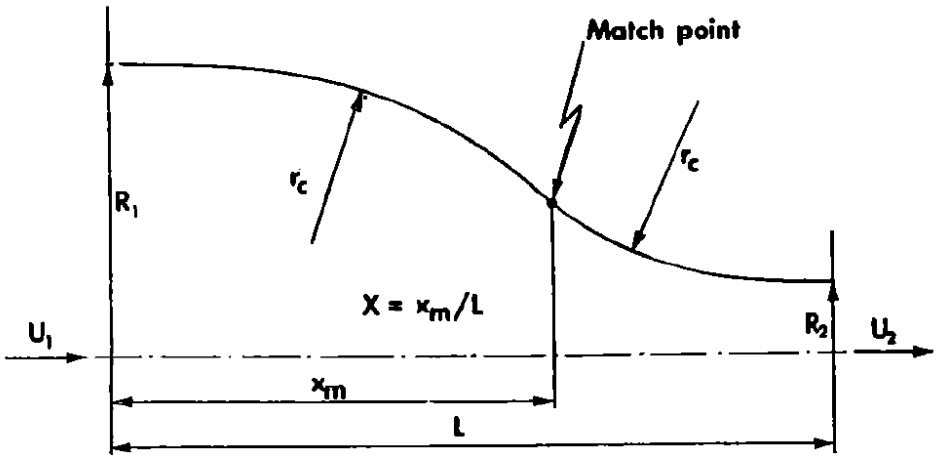

Fig. A.1: Nomenclature for the Design of the Contraction Cone[20]

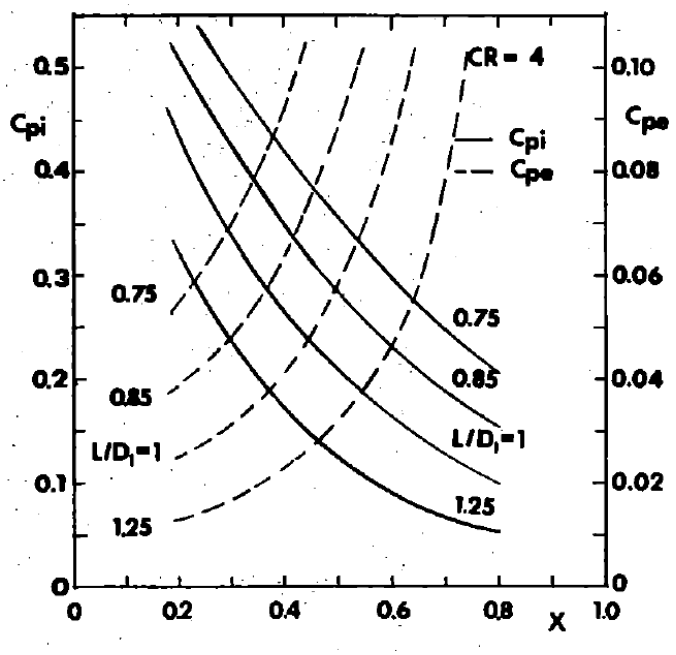

Fig. A.2: Design Chart of a Contraction with a CR of 4[20]

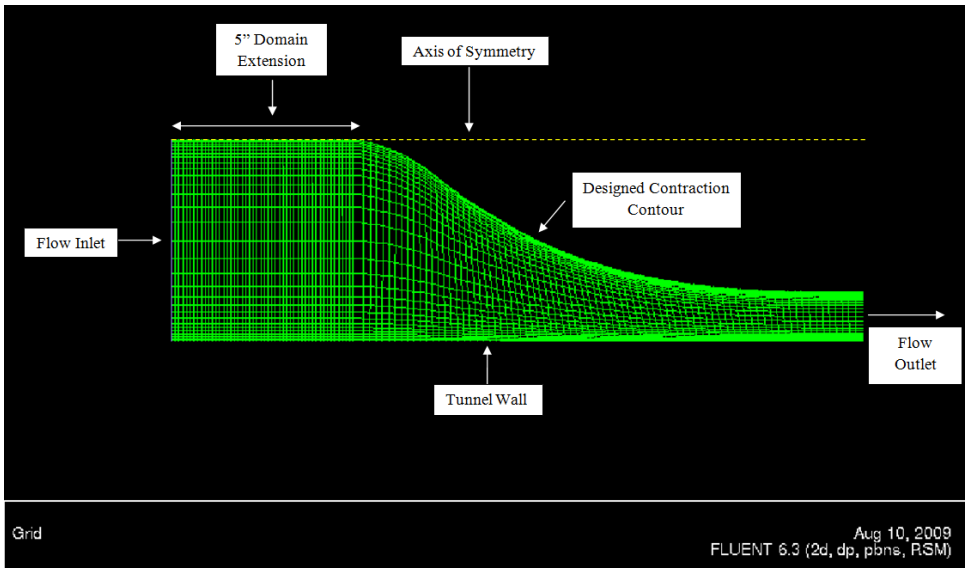

Fig. A.3: The Computational Domain and its Mesh Generated for the Contraction Region for CFD Analysis in FLUENT

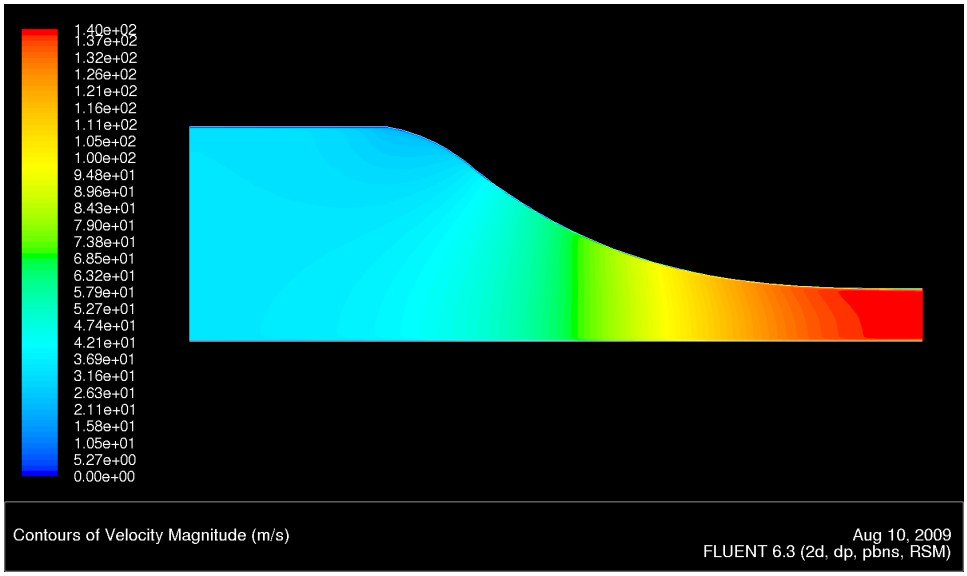

Fig. A.4: Velocity Contours of the Contraction Region

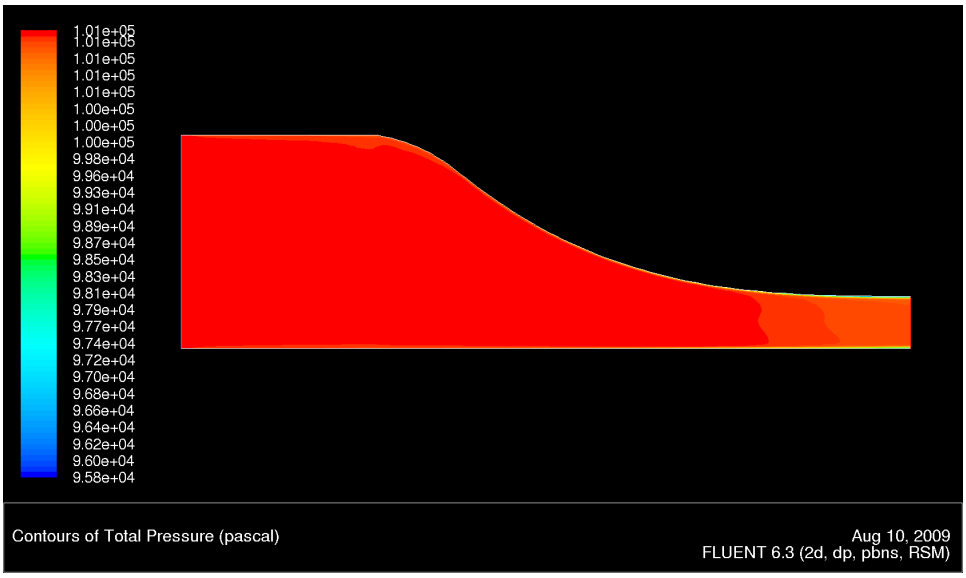

Fig. A.5: Total Pressure Contours of the Contraction Region

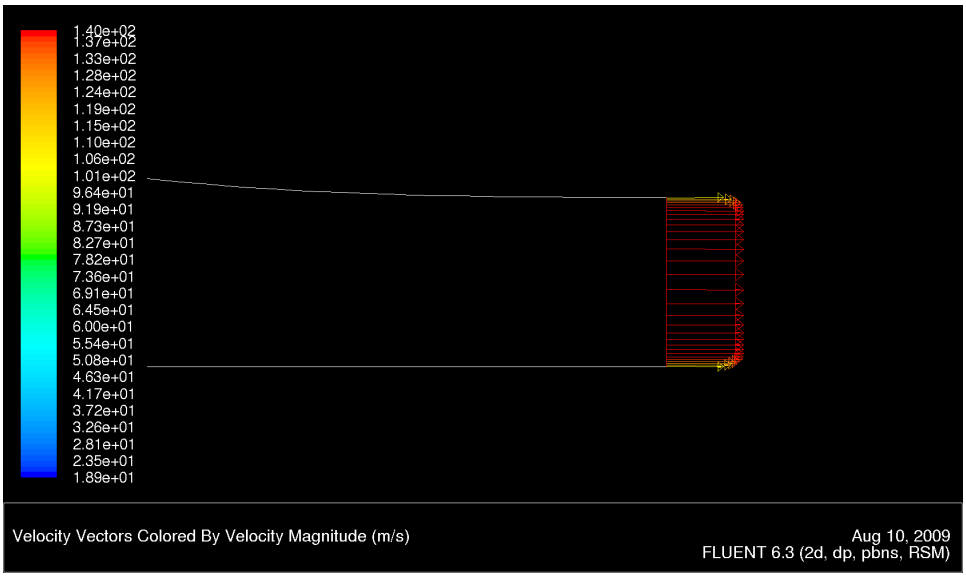

Fig. A.6: Velocity Profile at the Contration Outlet

Appendix B - Design of Aft-Body Diffuser

The geometry of the diffuser is fully described by the diffuser angle θ and divergence ratio, N/W, where N refers to the diffuser length and W refers to the diameter of the duct right before the diffuser. The aft-body diffuser was designed based on the design chart provided by Blevins[21] for a conical diffuser. This is shown in Fig. B.1 where the line of first appreciable stall for a conical diffuser is shown. Stall is the condition where the flow separates from the diffuser wall while an appreciable stall is defined by Blevins as

Flow generally follows diffuser contours. Boundary layer thickens. Small regions of separation and erratic flow are generally first seen in corners and they occupy no more than 1/5 *of diffuser wall. There is little or no reverse flow.*

Therefore, based on those guidelines and taking into consideration of the constraints and requirements of the test facility, the aft-body diffuser was designed at a diffusive angle of 4.5° extending a total length, N of 44 inches with the diameter of the duct, W at 2.68 inches (1.34 inches in diameter for one side of the bypass annulus). The measurement for the duct is fixed by the engine baseline model geometry. By applying the geometry values to Fig. B.1, it can be determined that the design is just above the line of first appreciable stall for a conical diffuser. Due to space constraints in the test facility, the design was considered to be satisfactory.

The determination of the appropriate distances to place the aft-body diffuser struts was based upon the calculation of flow over a circular cylinder. The 1 inch x 1 inch struts were assumed to be a 1 inch diameter cylinder. By combining a uniform flow with velocity V_∞ and a doublet of strength κ, the flow over a cylinder can be modeled as a streamfunction

shown in Eq. B-1 described in polar coordinates.[27]

$$\psi = (V_\infty r \sin\theta)\left(1 - \frac{R^2}{r^2}\right) \tag{B-1}$$

Where R refers to the radius of the cylinder. Fig. B.2 shows the flow over a cylinder with its associated nomenclature. By differentiating Eq. B-1, the velocity field of flow around a cylinder in the r direction can be obtained. This equation is shown in Eq. B-2

$$V_r = \frac{1}{r}\frac{\partial\psi}{\partial\theta} = \left(1 - \frac{R^2}{r^2}\right) V_\infty \cos\theta \tag{B-2}$$

Setting the incoming velocity V_∞ at 300 ft/s, radius of the cylinder to be 0.5 inch and the angle of the flow at close to 180°, the normalized velocity in the radial direction was plotted against the radial distance, r from the center of the cylinder. The graph showing the relationship between these two varibles is shown in Fig. B.3. It can be observed in Fig. B.3 that the radial velocity reaches 99% of the free stream velocity at approximately 6 inches away from the center of the circular cylinder. Therefore, the first pair of the aft-body diffuser struts were placed to be a conservative 8.5 inches away from the leading edge of the conical diffuser to prevent significant flow disturbances from propagating into the bypass duct.

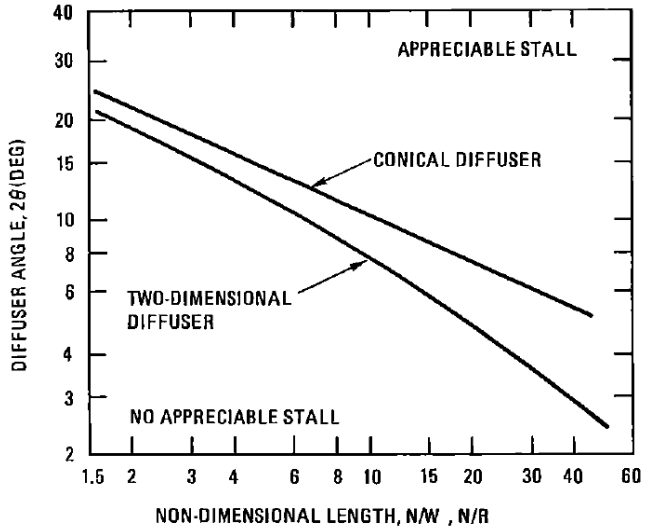

Fig. B.1: Design Chart for a Conical Diffuser[21]

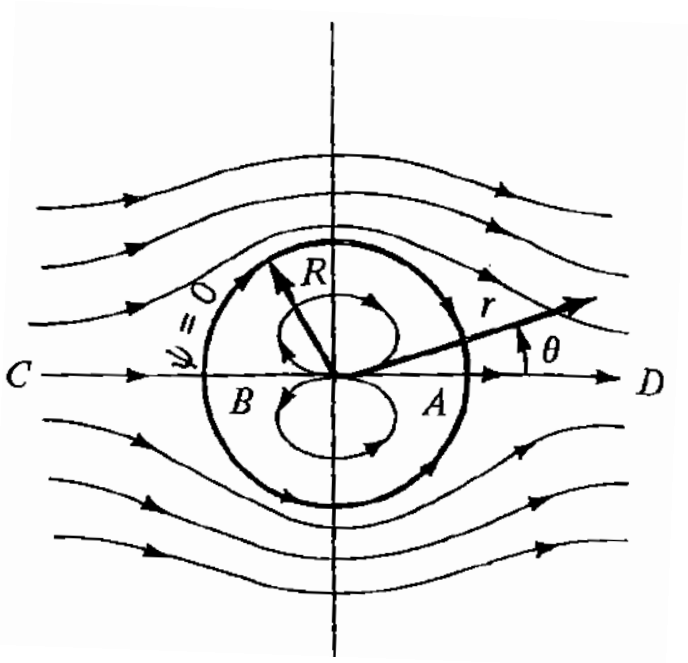

Fig. B.2: Flow Over a Cylinder[27]

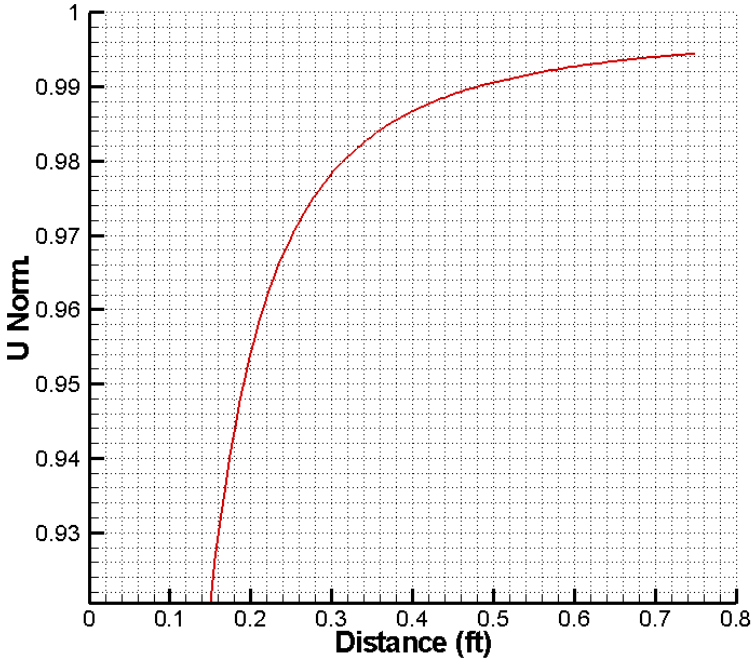

Fig. B.3: Relationship Between the Radial Velocity and Cylinder Radial Distance for Flow over a Circular Cylinder

Appendix C - Assembly of Full Test Model

The step by step assembly process for the full test model is as below:

1. *Slide the engine baseline models onto the alumimum beam through the center cavity according to the sequence shown in Fig. 2.2. Part E of the engine baseline model should be inserted first followed by the rest of the four parts. Make sure that the rounded corner in each model is positioned at the 12 O'clock position.*

2. *Slide the second section of the contraction cone onto the beam. The same rule applies as in Step 1 in regards to the position of the rounded cavity corner.*

3. *Slide the first part of the contraction cone onto the beam and position it in place by tightening 0.25 inch set screws into the two holes located at the underside of the contraction cone onto the aluminum beam. This secures the contraction cone and baseline models with the aft-body diffuser.*

4. *Attach the gearbox fairing on the underside of the engine baseline model. If the engine baseline model sections are positioned correctly, there should be eight No. 10 holes; two for the attachment of the in-flow diverter, four for the main gearbox fairing and two for the closeout fairing.*

5. *Complete the assembly by attaching the pair of crane beams on the upperside of the engine baseline models. There should be eight No. 6 holes.*

6. *The complete assembly of the test model is shown in Fig. C.1.*

Fig. C.1: Complete Assembly of the Test Model

Appendix D - Design of Axisymmetric Tunnel Sections

The axisymmetric tunnel sections are responsible for housing the test model and consists of three sections; tunnel sections A, B, and a rotating test section C. These sections measure 24 inches, 42 inches and 42 inches in length, respectively. Tunnel section A is connected to the wind tunnel inlet via the first square-to-round section followed by the rotating test section C, while tunnel section B connects to the other end of rotating test section C before transitioning into the wind tunnel diffuser via the second square-to-round section. The tunnel sections were then connected to one another using gear bearings and gear housings described in Section 2.2.1.3. This design fixes tunnel sections A and B but provides test section C with the ability to rotate.

Tunnel section A was designed with three sets of screw holes in place. The first set consists of 16 holes drilled circumferentially with a spacing of 22.5° from the outer surface of the axisymmetric section into the wall. These holes were fabricated to connect a bearing to the extreme end of tunnel section A. On the opposite end, eight No. 10 holes were located, spaced 45° apart and drilled into the wall of the axisymmetric piece from the side so that a ring-shaped round flange can be attached. The round flange will assist in making a connection with the square-to-round section. The third set of holes consists of four No.5 holes drilled 90° apart positioned 6.5 inches from the end of the axisymmetric section. These holes represent the locations where the struts from the contraction cone will make a connection with the test section. Detailed dimensions of the round flange and tunnel section A is shown in Fig. H.2 and Fig. D.1.

Apart from two sets of screw holes, tunnel section B was designed in a similar way to tunnel section A. Referring to Fig. D.2, tunnel section B has been drilled with similar screw holes on both ends as tunnel section A to connect another pair of bearing and round flange

to both ends of this 42 inch piece. The additional two sets of 3/8 inch holes on the surface of tunnel section B serve as the locations where the struts of the aft-body diffuser will be attached to in which the entire test model will be cantilevered and supported from. These screw holes are eventually slotted to provide additional assembly space for the entire engine test model within the test facility in case of any unforeseen misalignments from the model or axisymmetric pieces.

The rotating test section C was assembled in between tunnel sections A and B to form the bypass annulus with the engine test model. Therefore, numerous screw holes are in place in this test section to serve as either mounting locations for experimental apparatus or as surface static pressure taps (Fig. D.3). Similar to tunnel sections A and B, the extreme ends of the rotating test section C were fitted with screw holes for the attachment of components to connect to other tunnel sections. In this case, 16 10-32 inch screw holes were drilled 1.35 inches from both ends, spaced 22.5° circumferentially apart to secure a pair of gear housings called gear housing A and gear housing B, respectively. Gear housing A and B are designed to attach on the right and left ends of the rotating test section C, respectively, for the connection to the fixed bearings on tunnel section A and B. The arrangement of this set-up can be observed in Fig. 2.22.

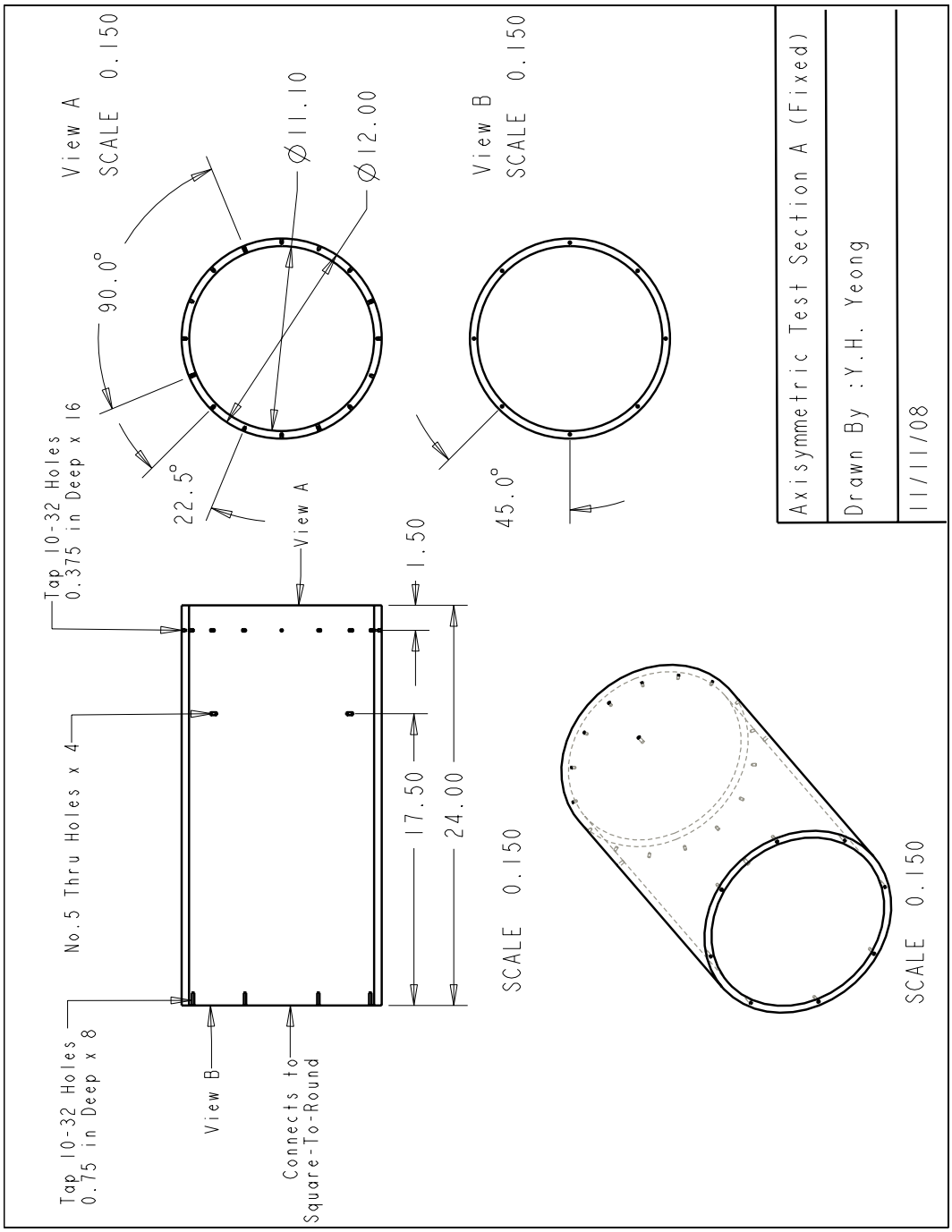

Fig. D.1: Axisymmetric Tunnel Section A (Fixed) Drawing

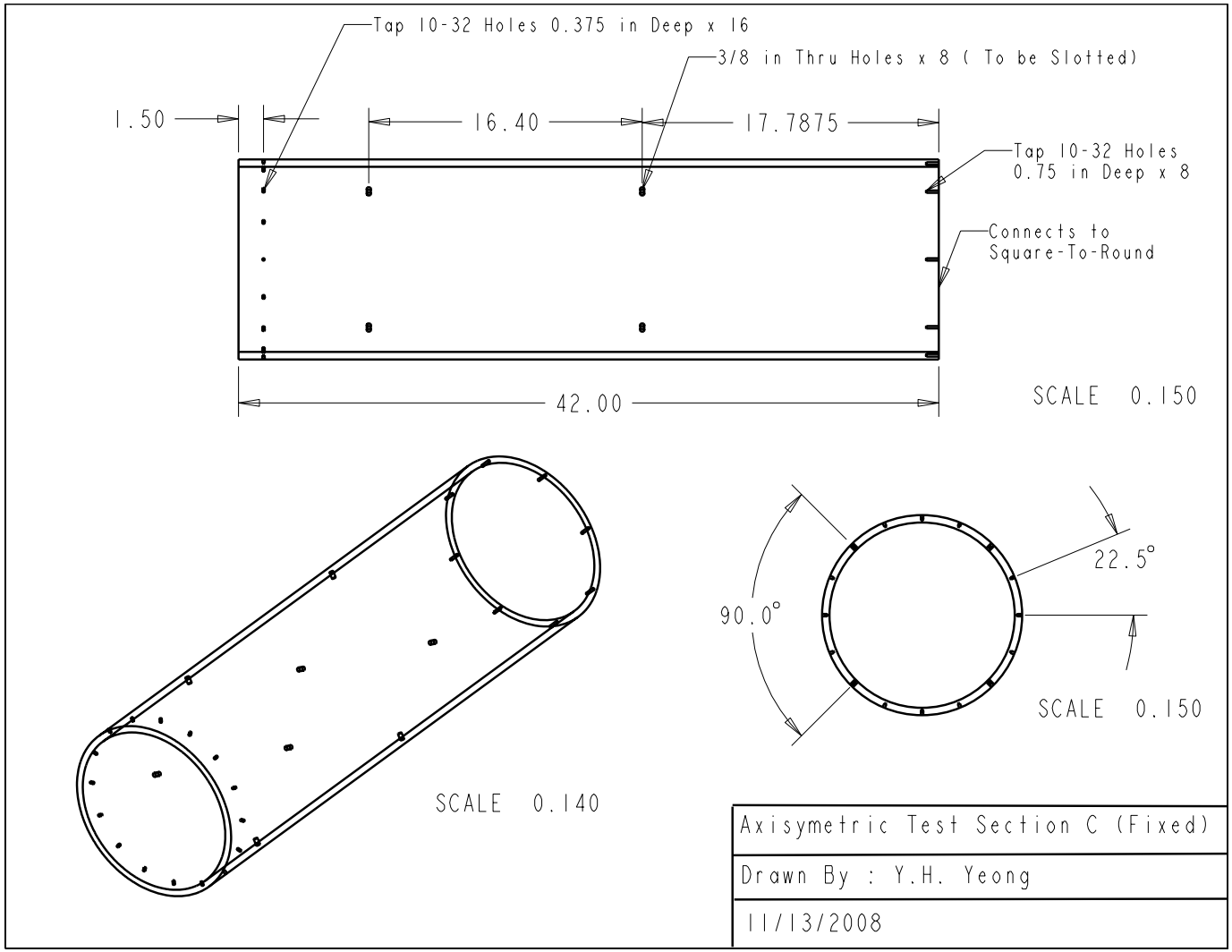

Fig. D.2: Axisymmetric Tunnel Section B (Fixed) Drawing

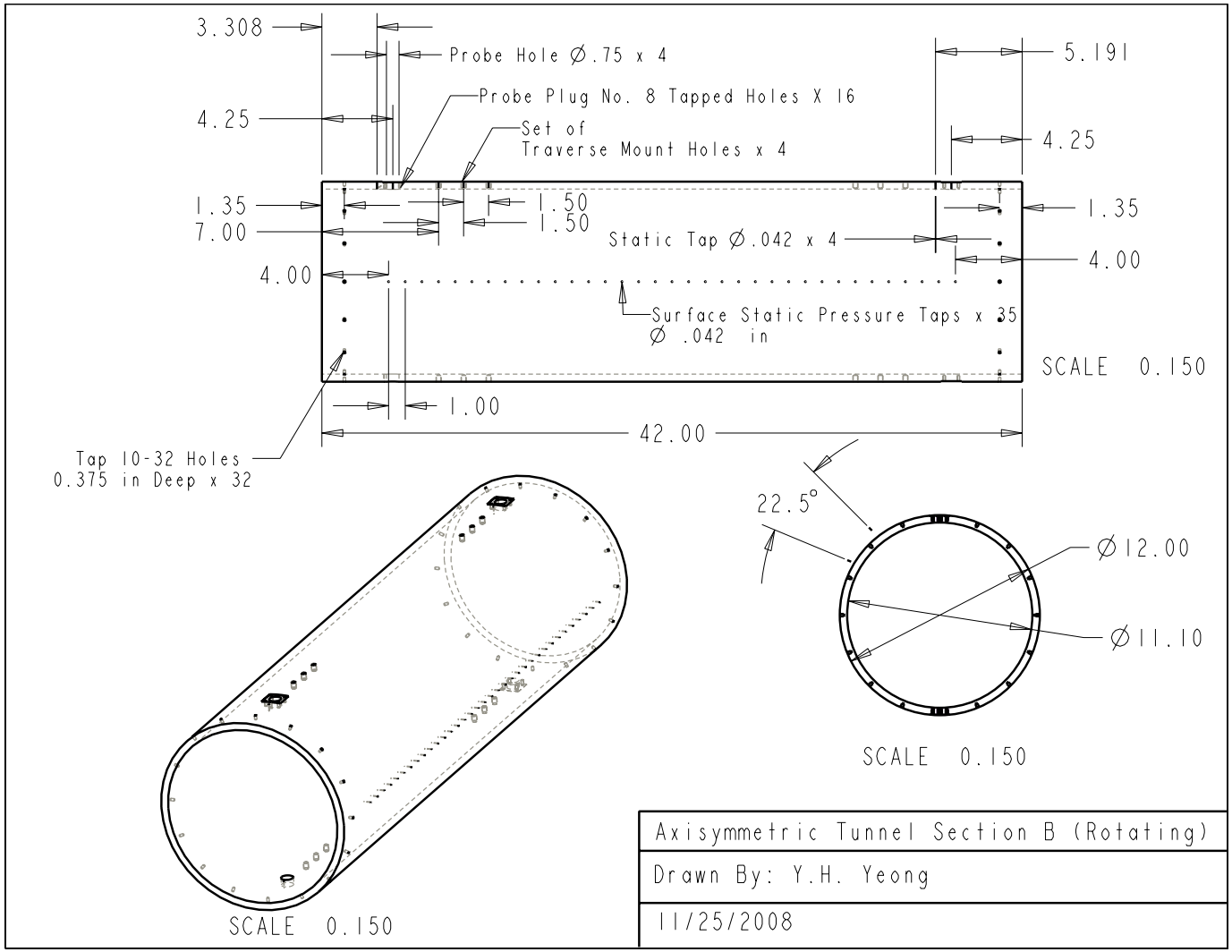

Fig. D.3: Axisymmetric Rotating Test Section C Drawing

Appendix E - Design of the Gear Bearings

The fixed gear bearing is a ring-shaped component with an inner diameter of 11.915 inches to match the outer diameter of the axisymmetric test section. The component is 2 inches thick to accomodate the placement of counter-bore screw holes spaced 22.5° circumferentially apart for the attachment of the bearing to the axisymmetric test sections as well as a groove for an O-ring (Fig. E.1). Since the entire outer surface of the fixed gear bearing rotates within the gear housing, the O-ring provides the necessary seal between the two bearing components to prevent a leakage of flow during wind tunnel operation.

There are two factors in ensuring an accurate seal for a dynamic rotary application, the material for the O-ring and the dimensions of the O-ring groove. The O-ring selected for this application was a 1/4 inch fractional width, 0.275 inch actual width Buna-N cord stock. Buna-N, also known as standard nitrile is widely used as a general seal and performs well with both petroleum or silicone oils. The lubricant eventually applied on the rotating surfaces of the bearings is a petroleum-based jelly called Vaseline. The groove of the O-ring on the fixed gear bearing has a groove depth and width of 0.263 inches and 0.378 inches respectively. These values were recommended by Problem Solving Products Inc., a company specializing in seal applications and design for a 0.275 inch O-ring. The recommended dimensions will provide the correct amount of squeeze in between the surfaces of the O-ring and the gear bearings to prevent a leakage in flow and at the same time allow the components to rotate.

As observed from Fig. E.2 and Fig. E.3, the gear housing is also a ring-shaped component, measuring 4 inches thick and 16.06 inches in diameter. The inner portion of the gear housing was designed to be divided into two cavity sections of different diameters and drilled from opposite ends. The first cavity meausures 14.195 inches in diameter and is 2 inches

deep while the second measures 11.915 inches in diameter to match the outer diameter of the axisymmetric test section with a depth of 1.75 inches. These two cavity sections are seperated by a flush surface 0.25 inches thick and 11.095 inches in diameter. Therefore, the fixed gear bearing was inserted in its entirety into the first cavity to form a rotating surface while the rotating test section was positioned in the second cavity. The gear housing was further secured to the rotating test section through counter-bore screws tightened in a circumferential manner around the axisymmetric piece. This concept connects and forms a rotating surface on both ends of the test section to gear bearings in tunnel sections A and B, respectively. In addition to providing a rotation motion for the test section, gear housing A is also responsible of transimitting torque from a geared stepper motor to the entire test section through a ring gear. The ring gear was designed to fit on a circular protruding section measuring 0.8 inches thick on gear housing A and secured via 16 No.10-32 screw holes positioned circumferentially apart by 22.5°.

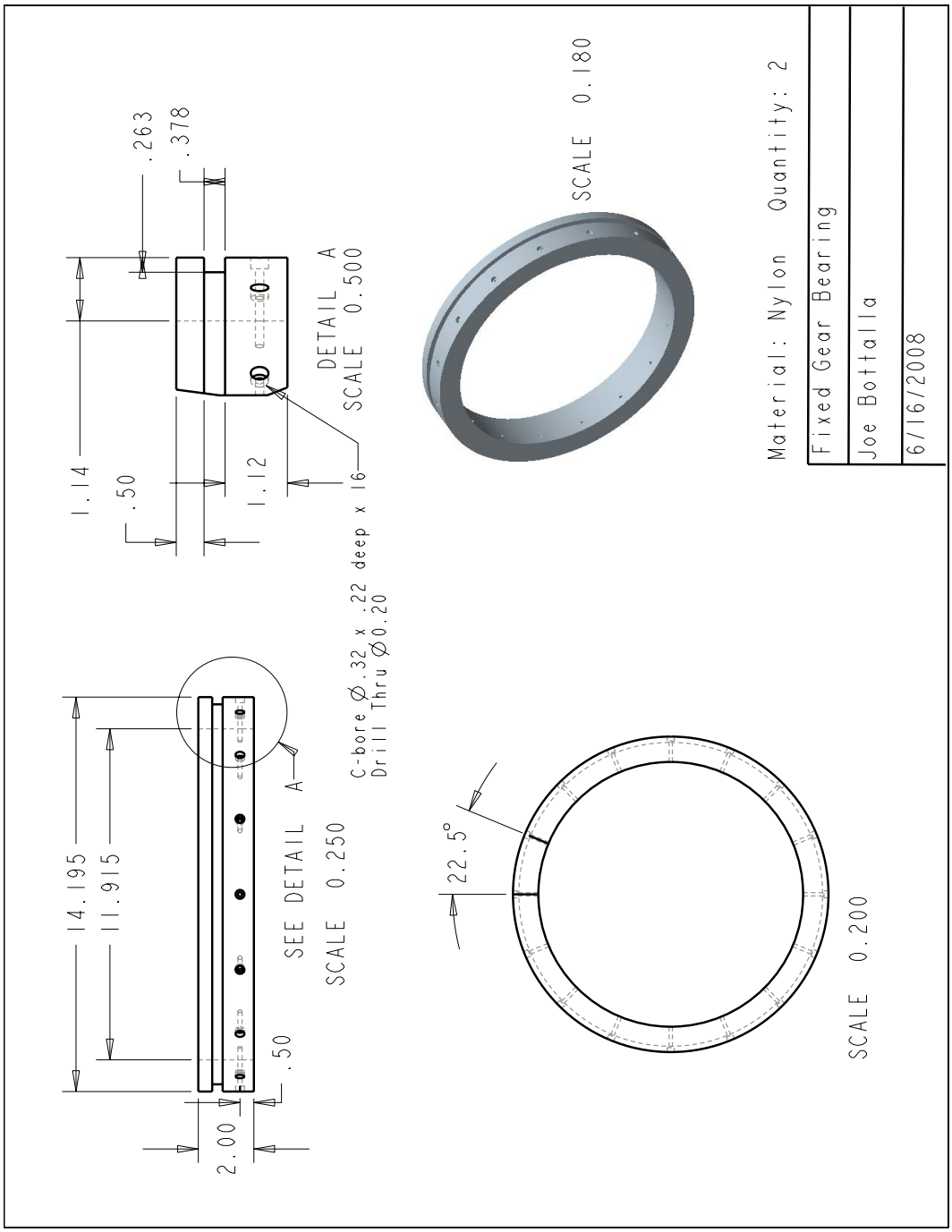

Fig. E.1: Fixed Gear Bearing Drawing

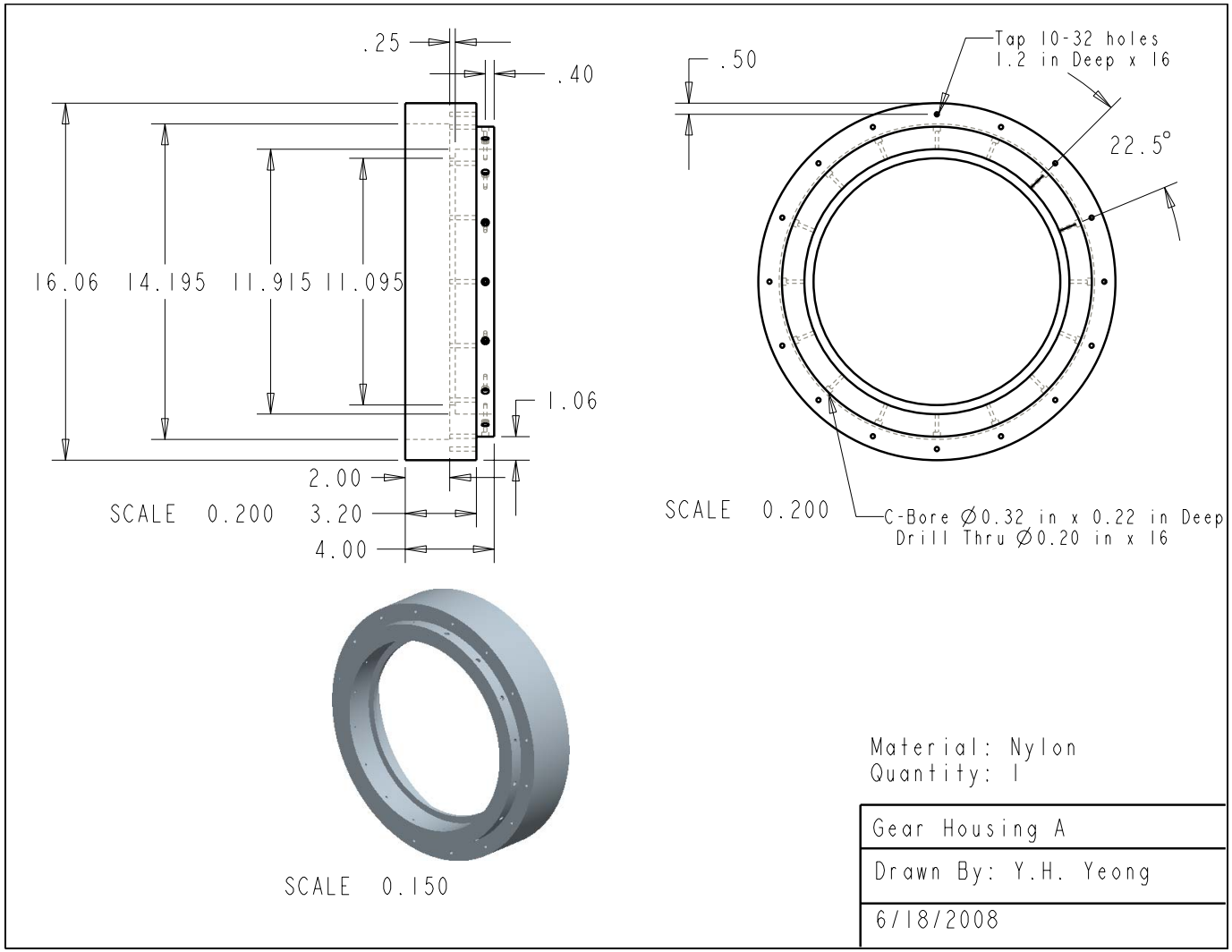

Fig. E.2: Gear Housing A Drawing

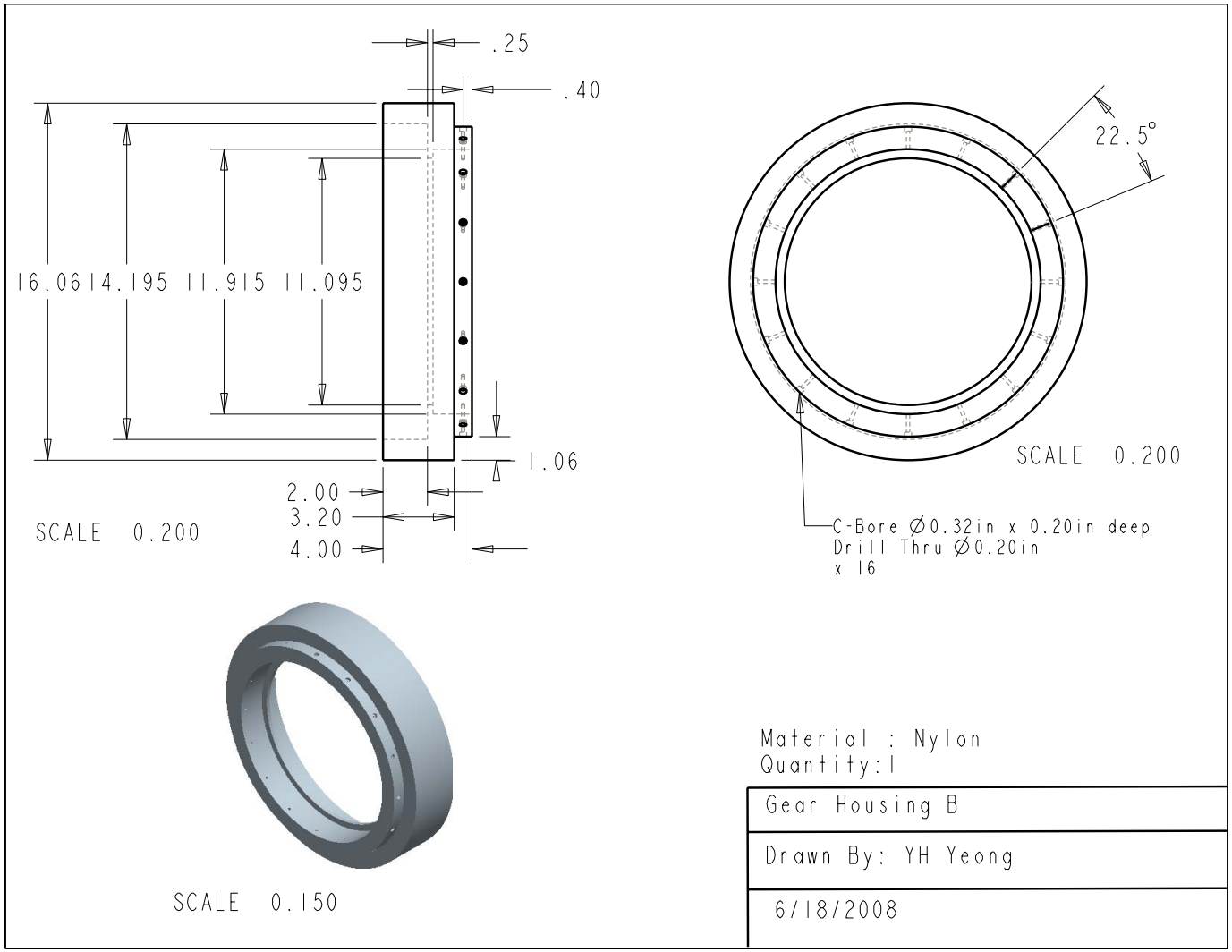

Fig. E.3: Gear Housing B Drawing

Appendix F - Design of Frames

The three frames, fabricated by Fox Valley Metal Tech consist of a 40 inch x 22 inch frame to support tunnel section A and two 40 inch x 38 inch frames for the support of both the rotating test section and tunnel section B respectively. The frames were made out of 2 inch by 2 inch steel tube with a wall thickness of 11 Gage. Each of the frames were welded with four steel plates on the top surface of the frame for the attachment of additional angled supports as well as mounting blocks with tapped holes on the underside of the frame for the insertion of casters. In addition, all the ends of the four legs were attached with metal square caps with a $1/2-13$ inch tapped hole through the center. The goal is to insert swivel leveling mounts on each of the legs of the frames through the metap square caps. After the maneuvering of the frame with the test section into position for assembly, the casters will be raised while the swivel leveling mounts will be released to secure the entire piece on the floor. Another purpose of installing the swivel leveling mount is to account for uneven floor surfaces in the Aerodynamics Research Lab. Detailed drawings of the frames and all is associated components can be found in Fig. F.2 to Fig. F.12.

To form a connection between the angled supports and the frame, steel L-bars were attached to the welded steel plates on the frame. The L-bars will provide the necessary surface for the attachment of the angled supports. The angled supports consist of aluminum L-brackets positioned at approximately 55° from the surface plane of the frame with either support pads or rollers attached to the ends of the angled supports. Tunnel sections A and B will be supported by the angled L-brackets with support pads while the rollers will support the rotating test section. The reason for this set-up is due to the fact that the test section will rotate while tunnel sections A and B remains fixed. A schematic showing the set-up for the complete structural support for the axisymmetric tunnel is shown in Fig. F.1.

The rollers were made of Nylon with an outer diameter of 2 inches and a face width of 0.88 inches. A 1/4 inch screw was inserted into the center of the nylon roller to serve as the axle for rotation while an aluminum "U" channel serves as support to the rotating axle. Detailed drawings of the different components of the roller can be found from Fig. F.13 to Fig. F.17.

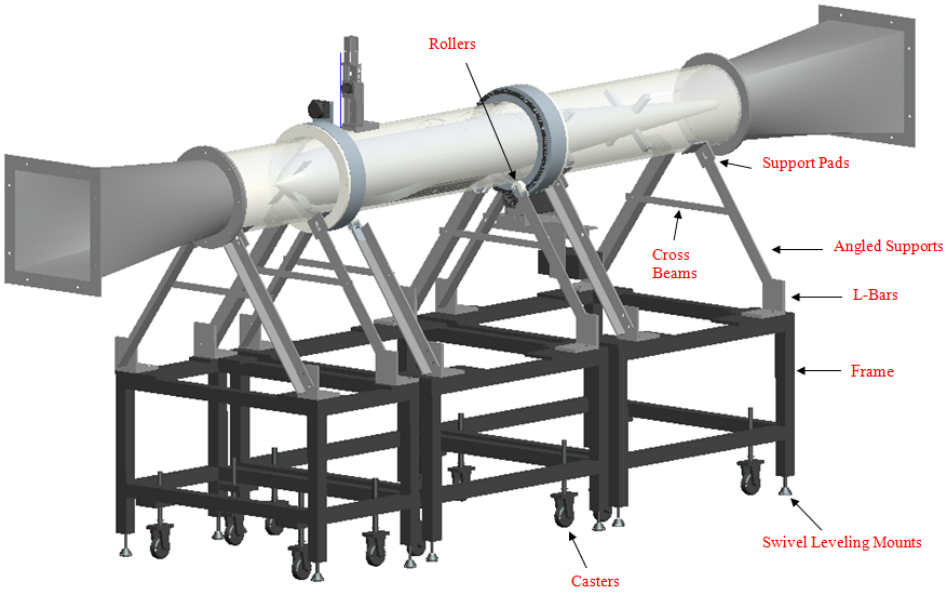

Fig. F.1: Structural Support Components for the Axisymmetric Test Section

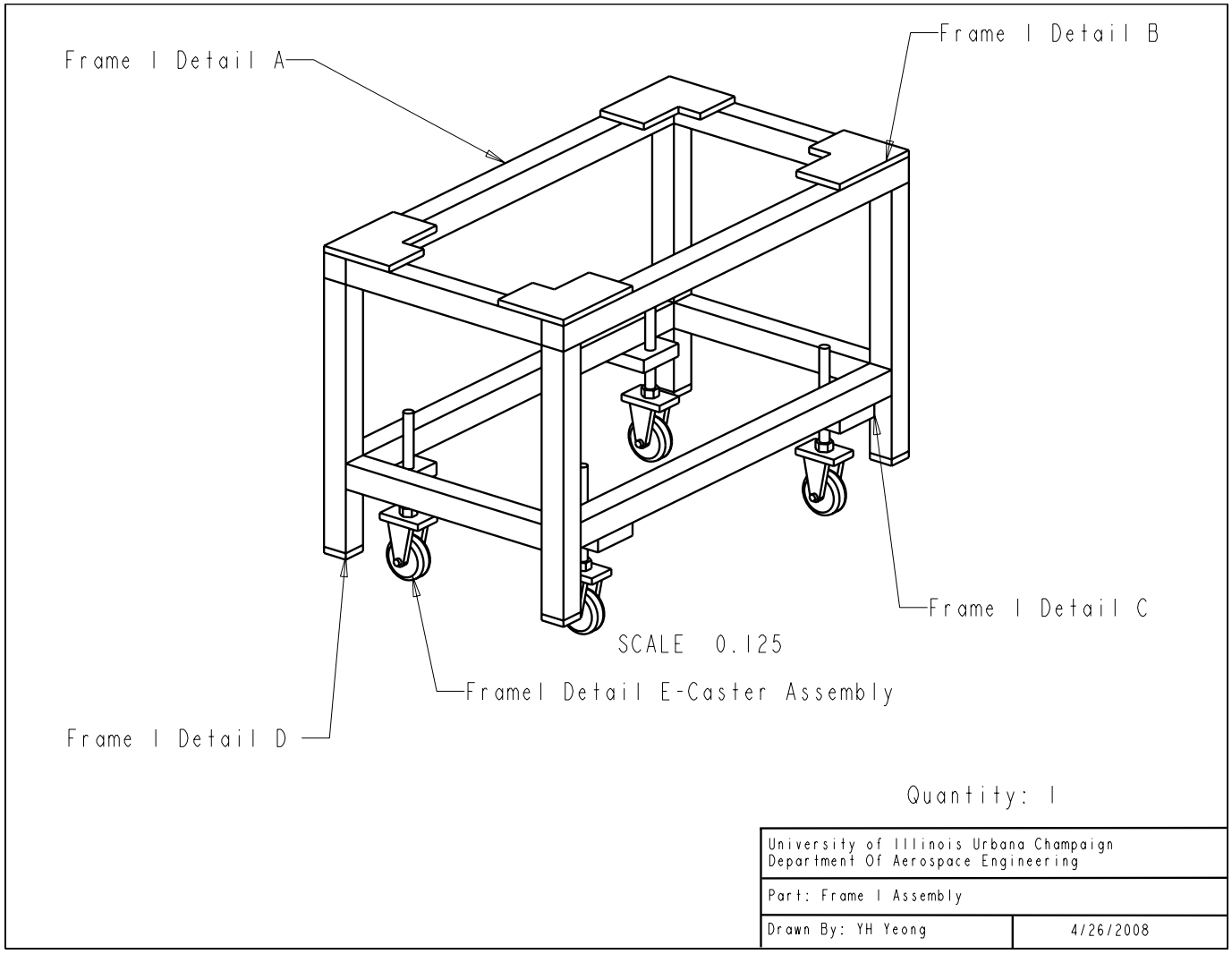

Fig. F.2: Isomteric View of Frame 1 with Attached Components

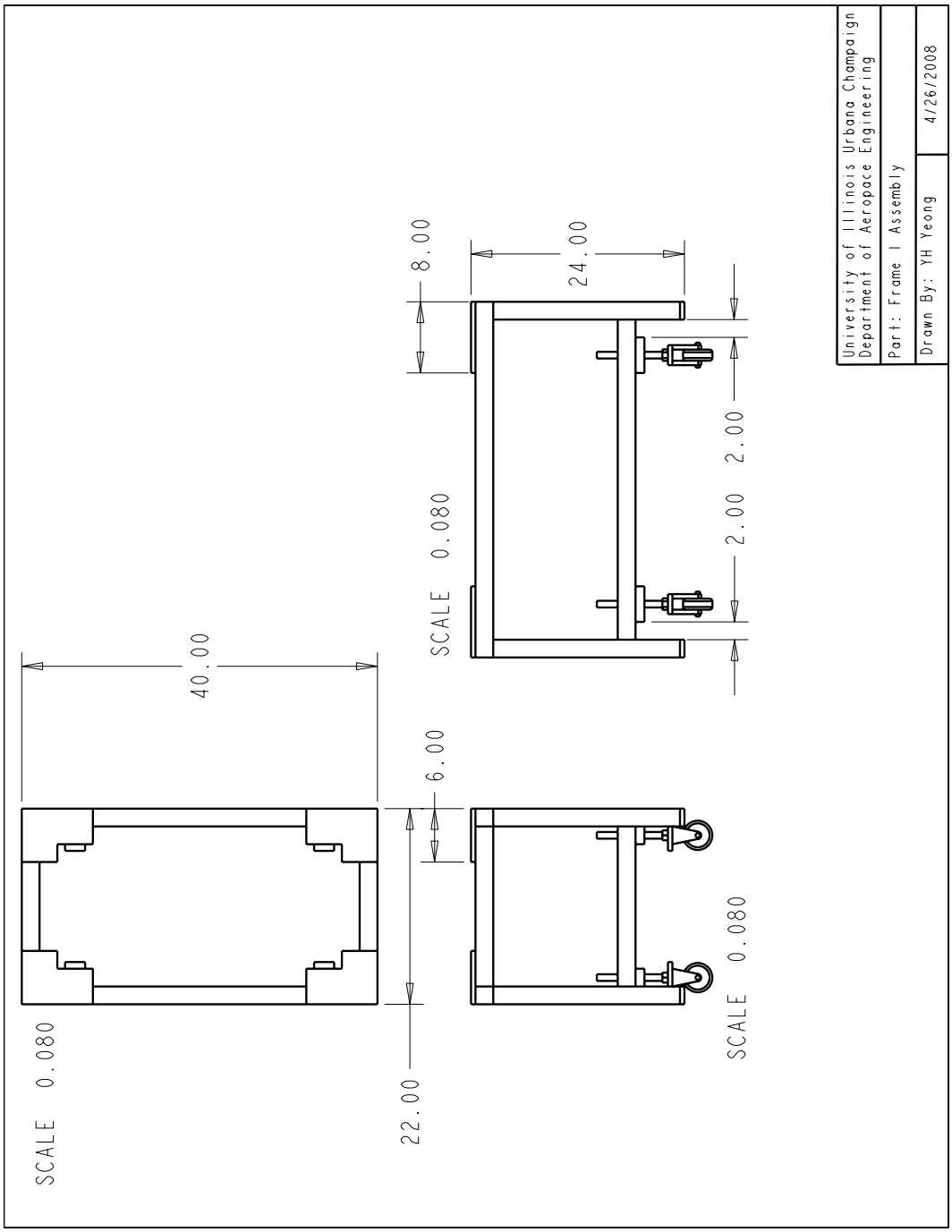

Fig. F.3: Dimensions of Frame 1

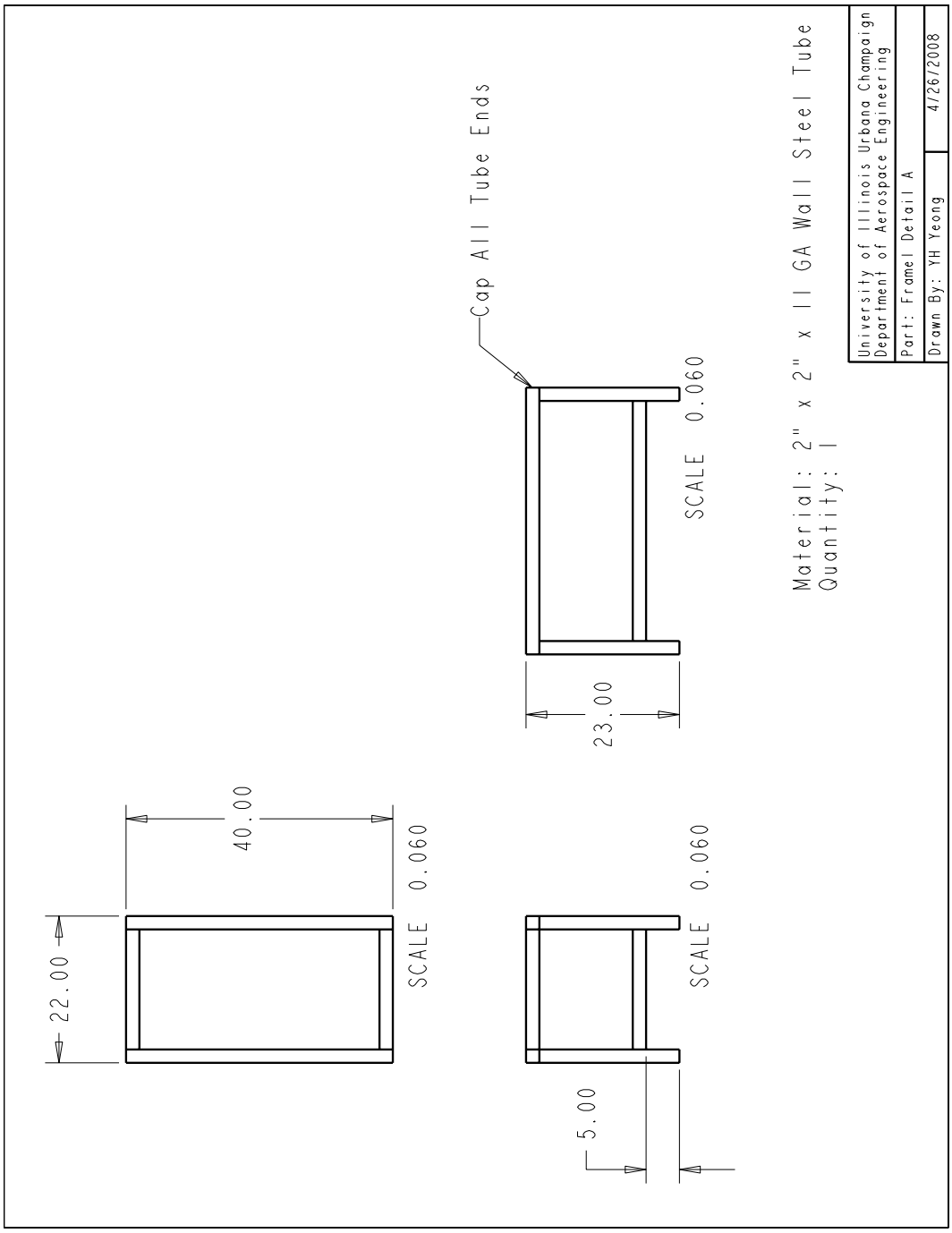

Fig. F.4: Frame 1 Detail A Drawing

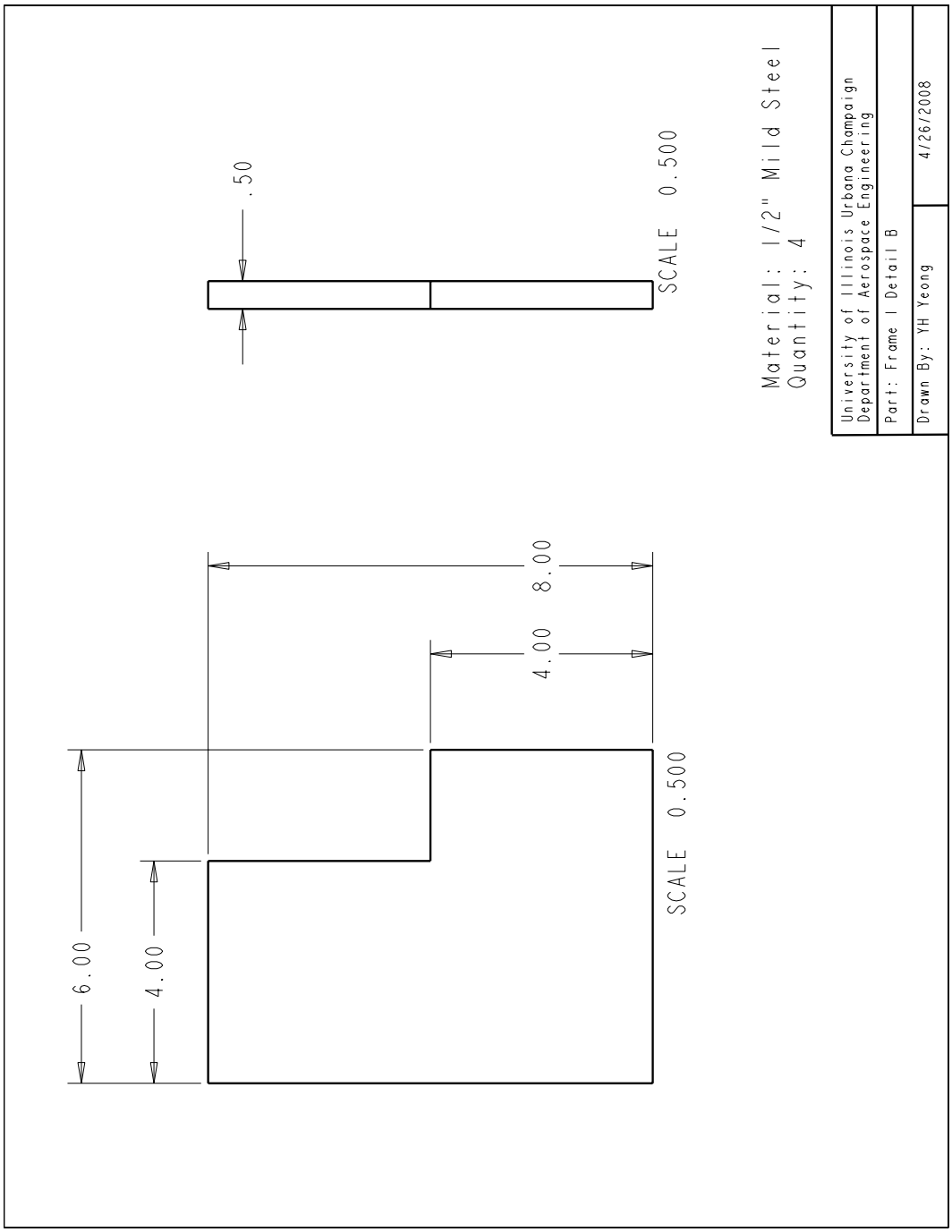

Fig. F.5: Frame 1 Detail B Drawing Drawing

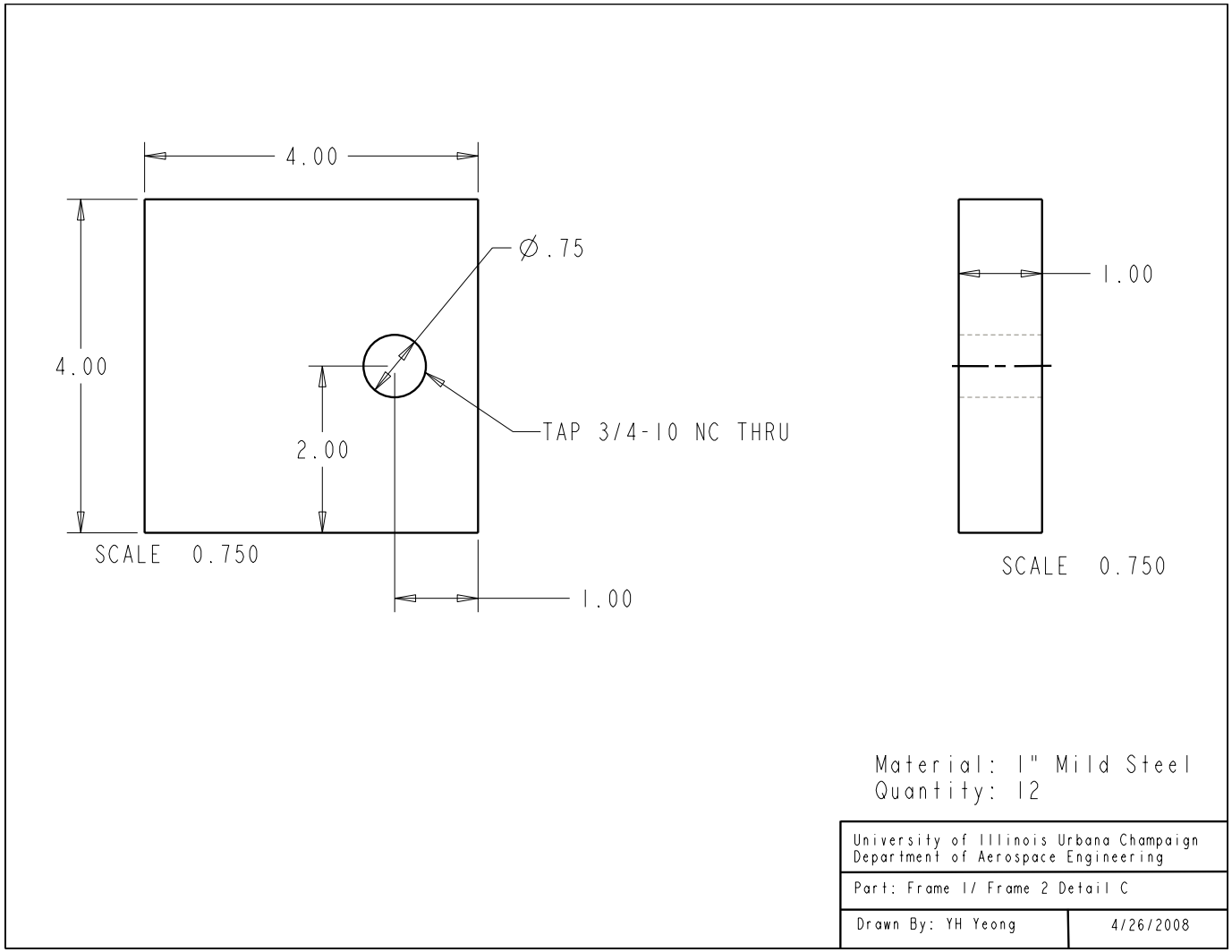

Fig. F.6: Frame 1 Detail C Drawing Drawing

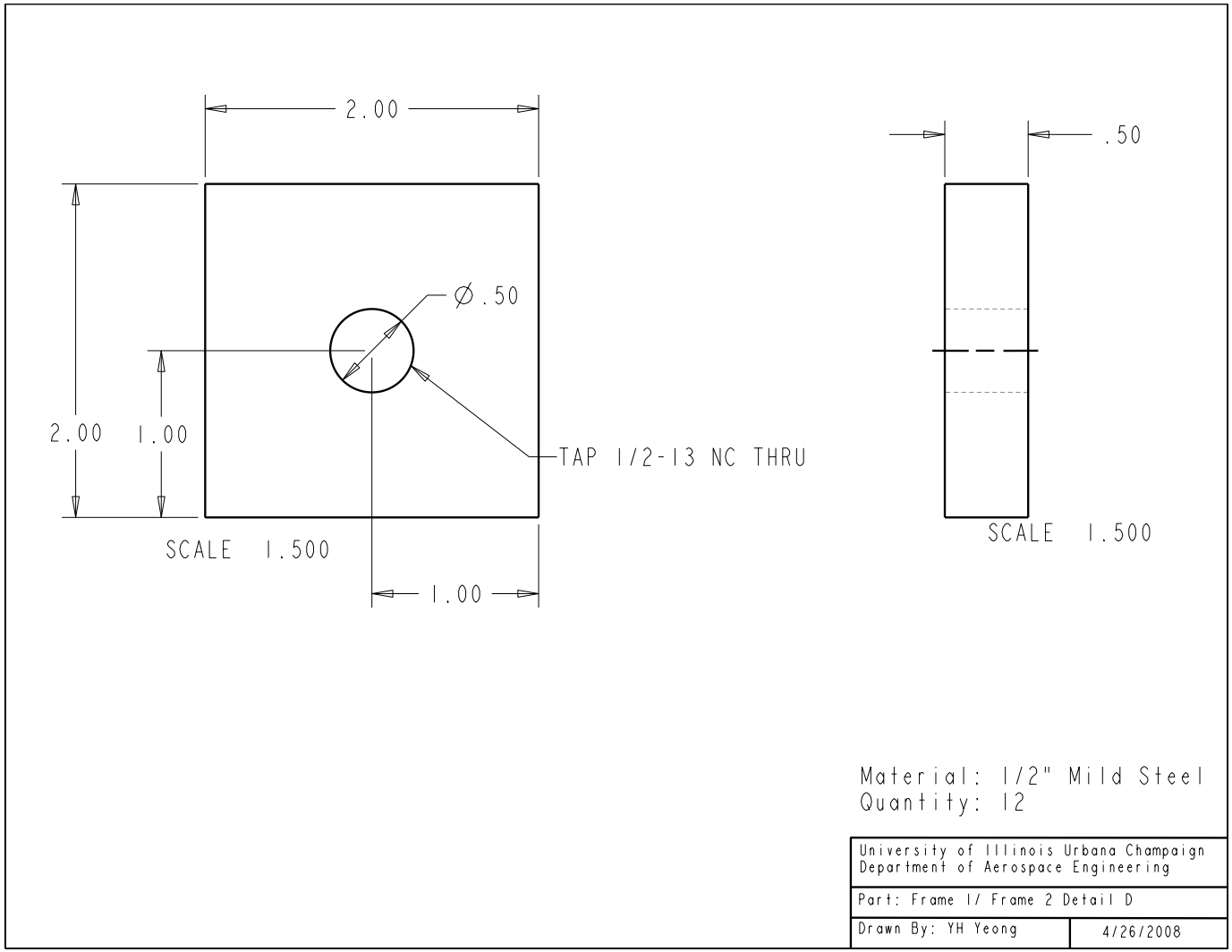

Fig. F.7: Frame 1 Detail D Drawing Drawing

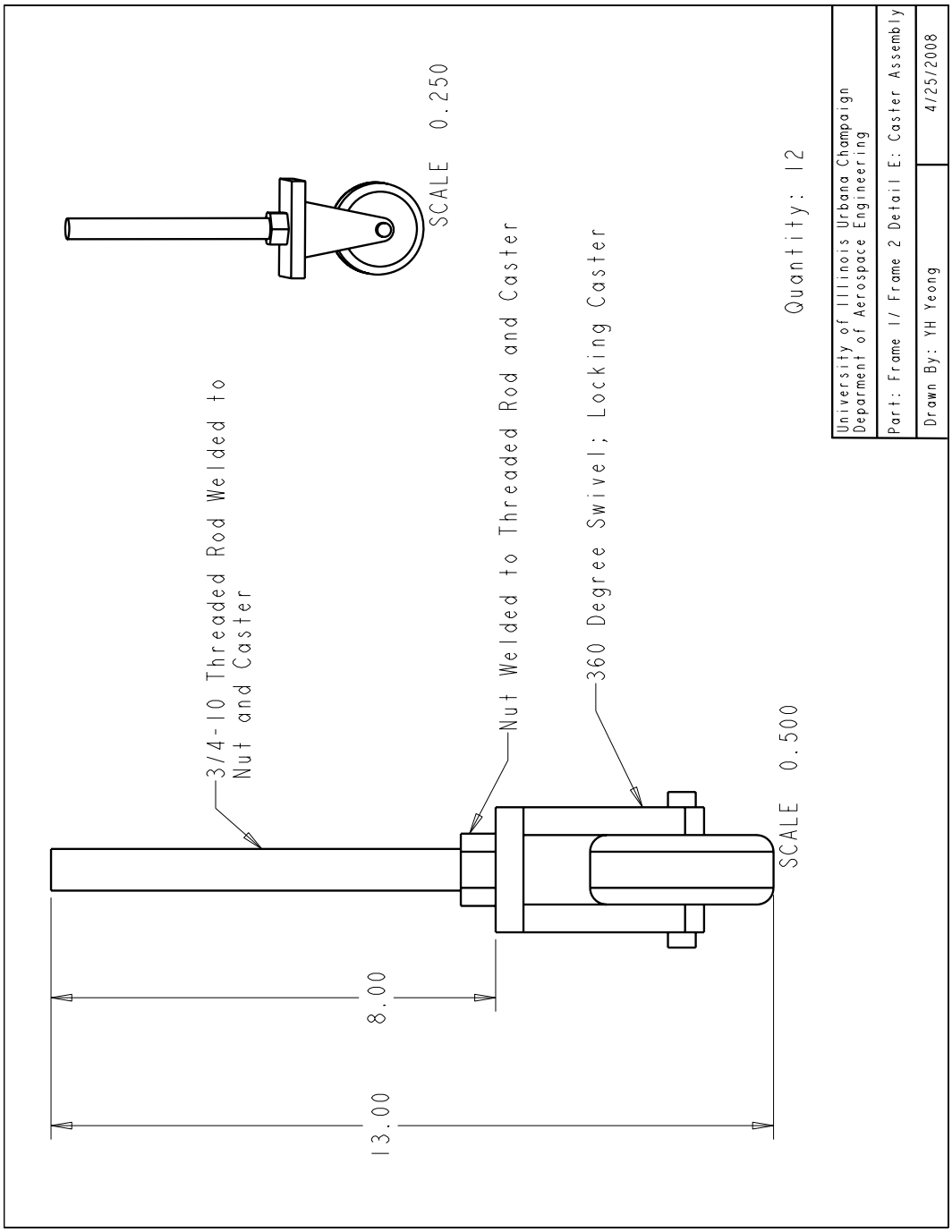

Fig. F.8: Caster Drawing

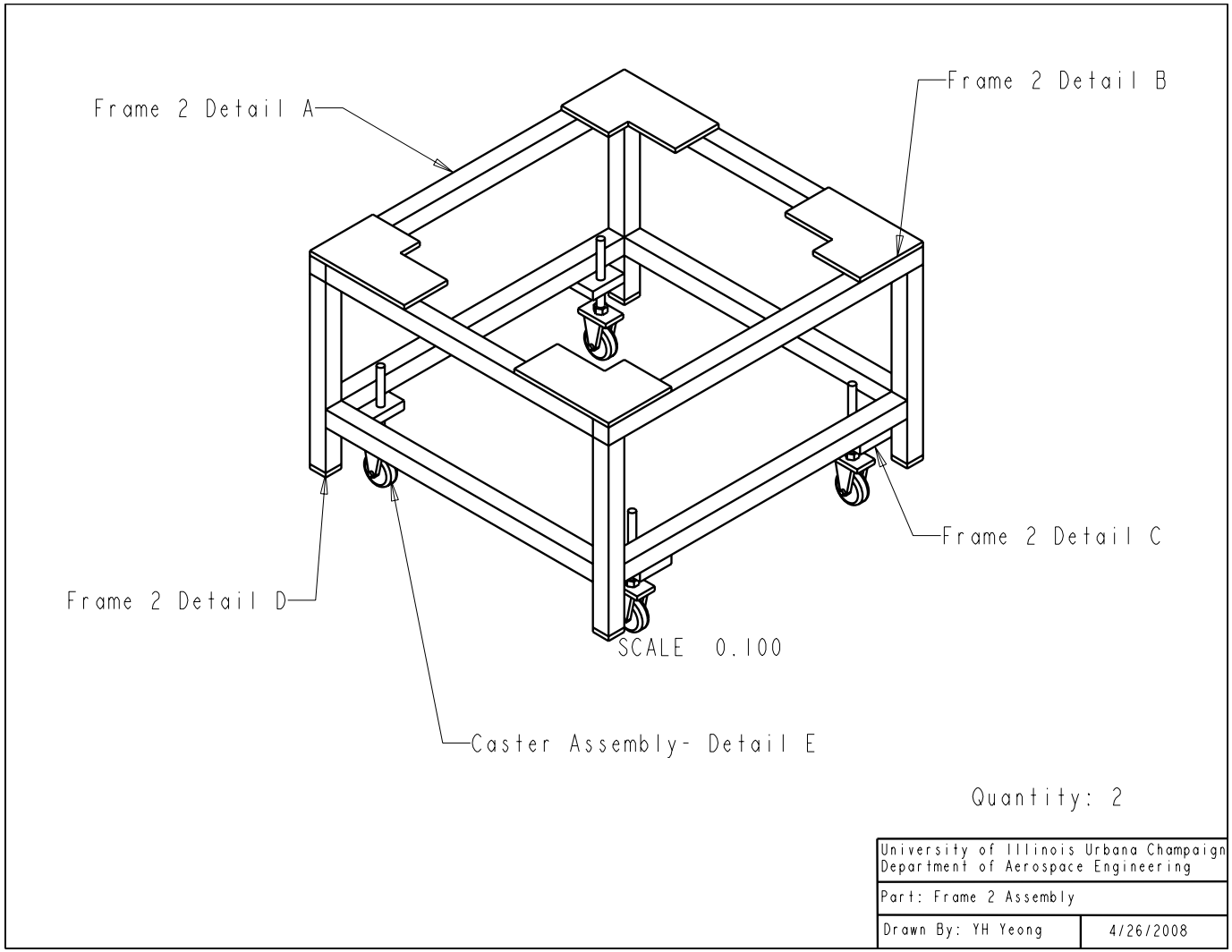

Fig. F.9: Isomteric View of Frame 2 and 3 with Attached Components

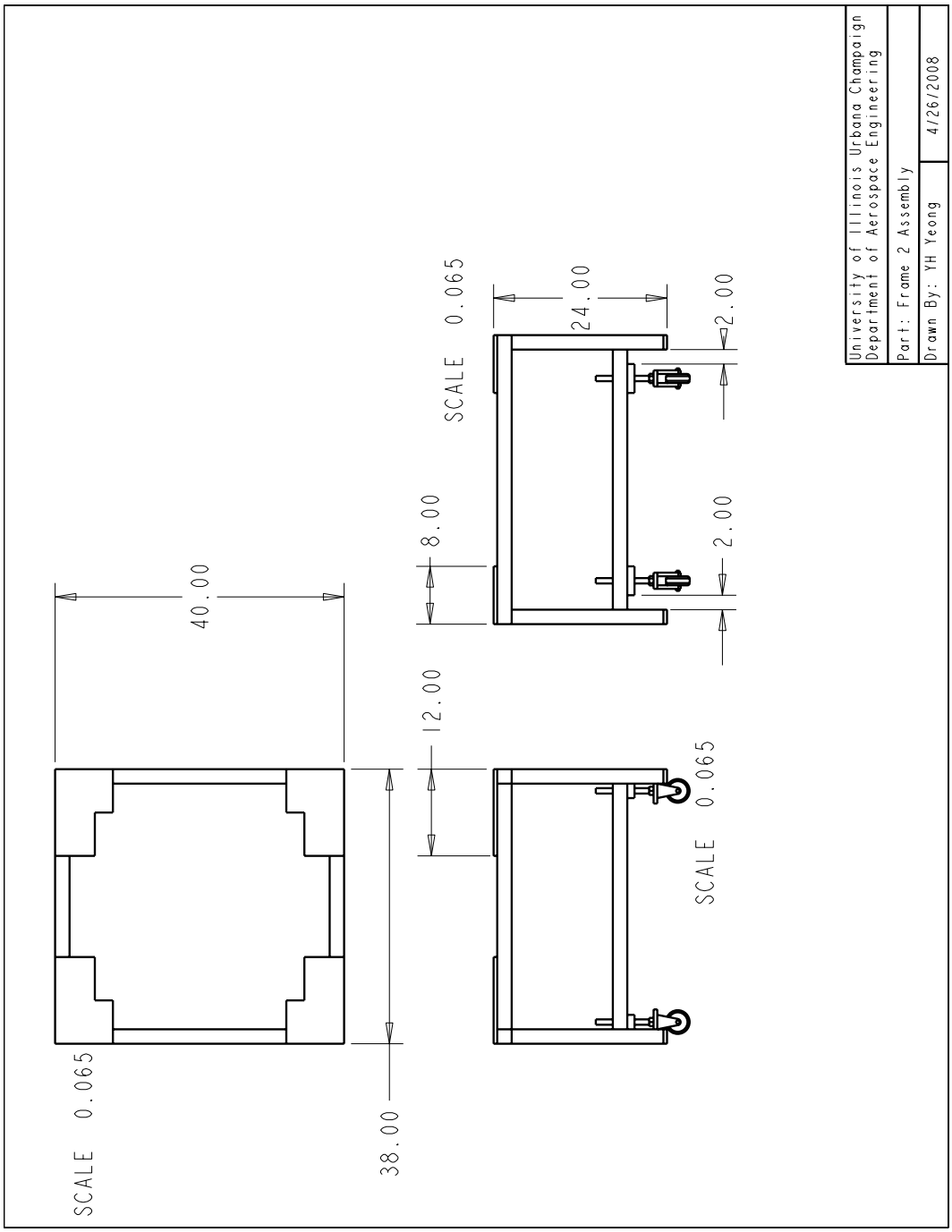

Fig. F.10: Dimensions of Frame 2 and 3

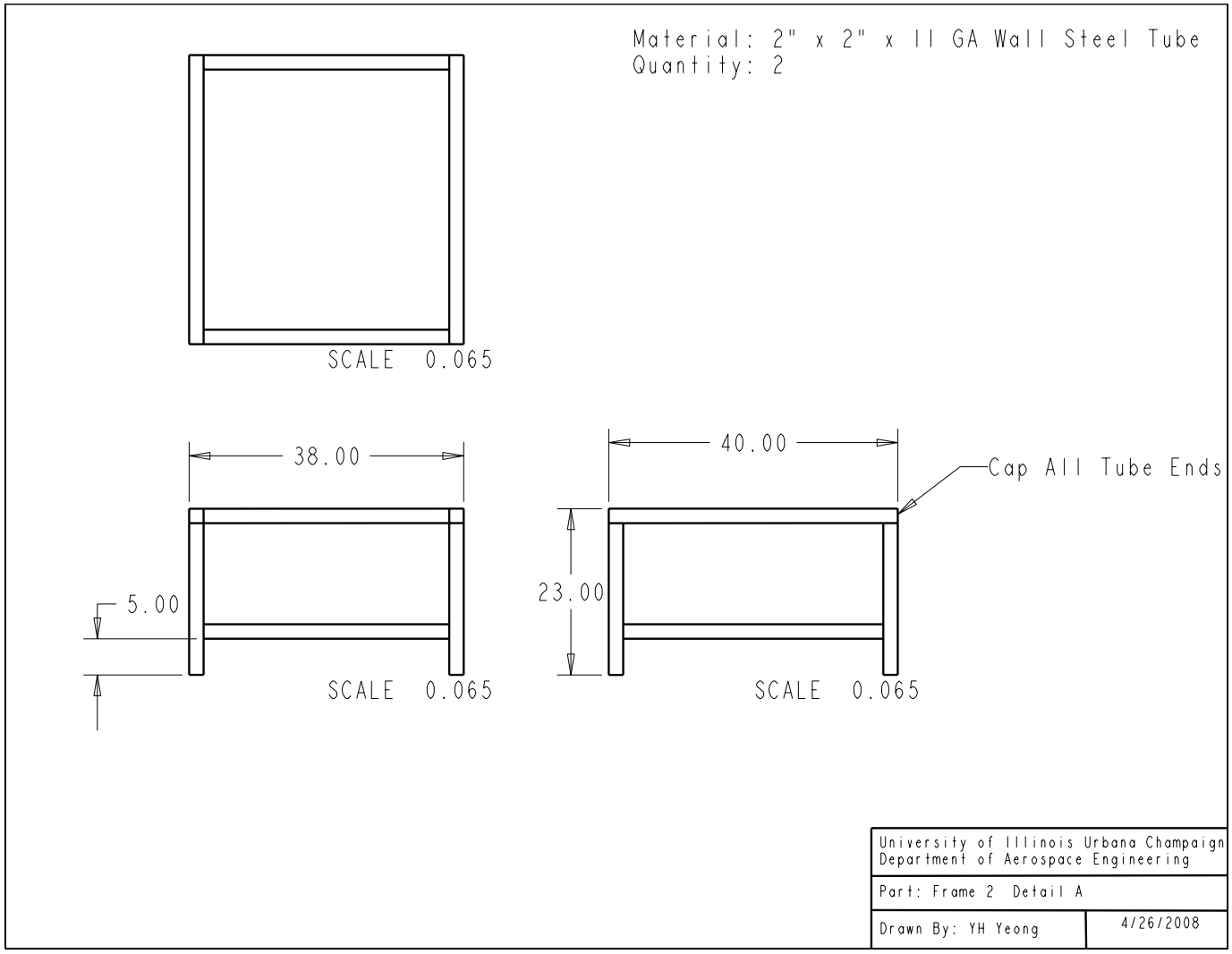

Fig. F.11: Frame 2 Detail A Drawing

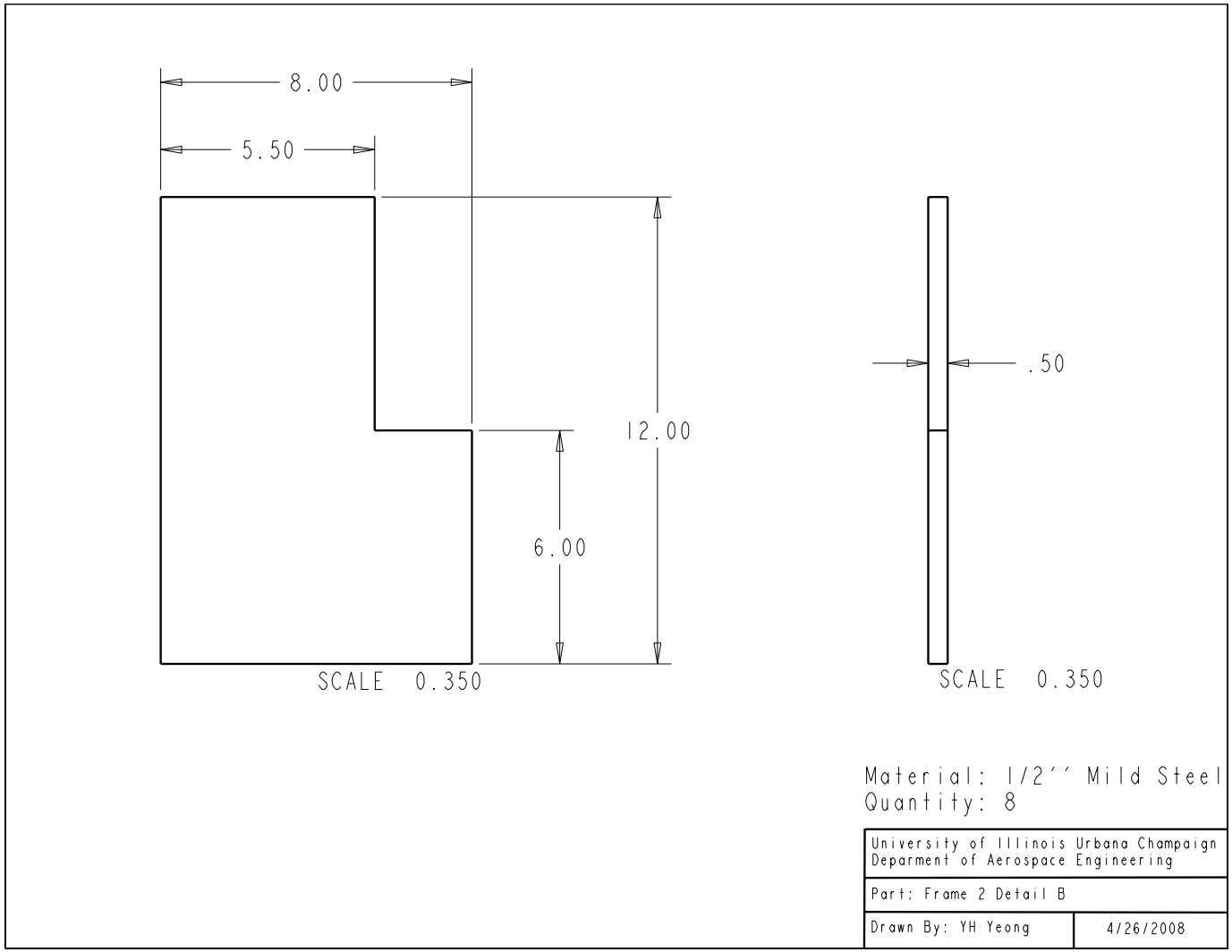

Fig. F.12: Frame 2 Detail B Drawing

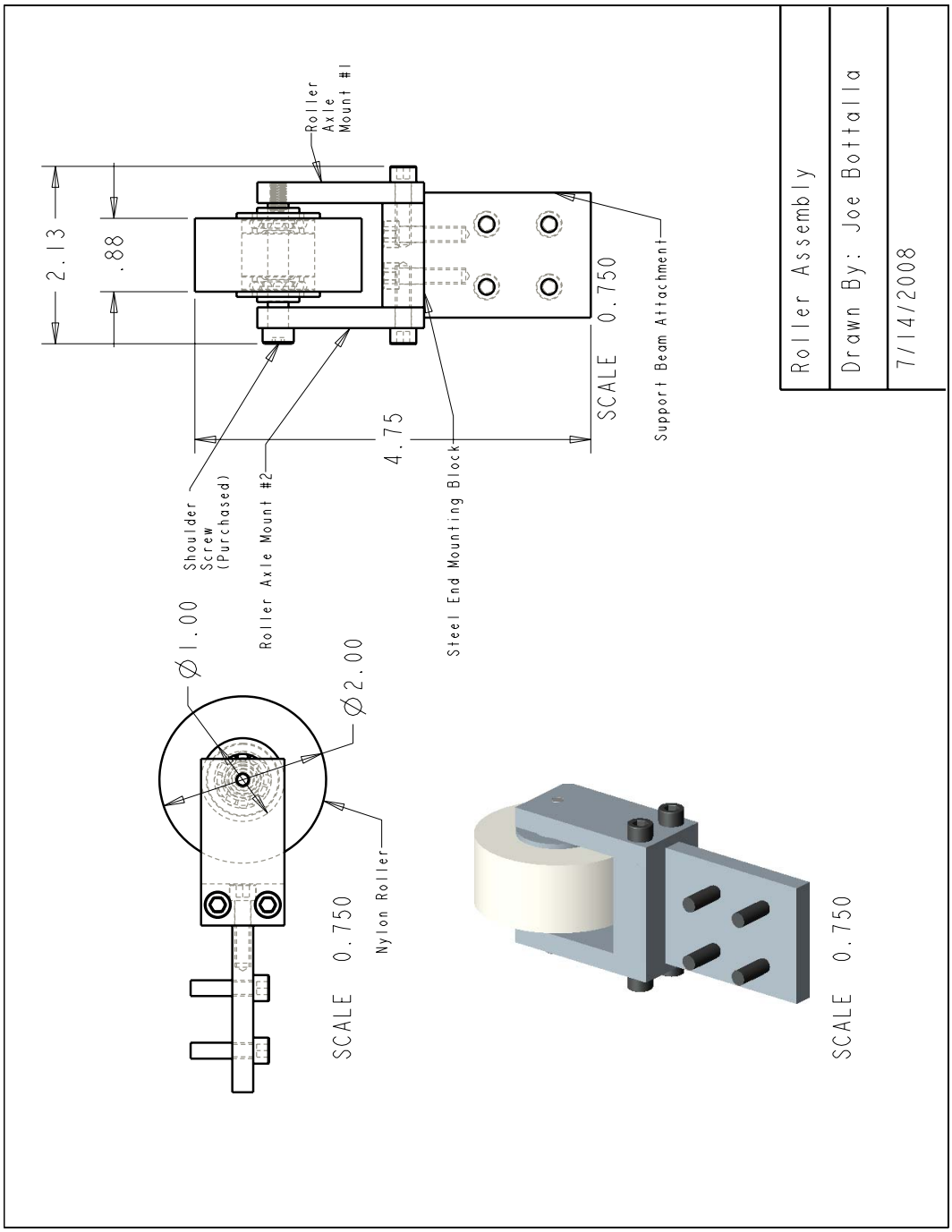

Fig. F.13: Assembly of Roller Component

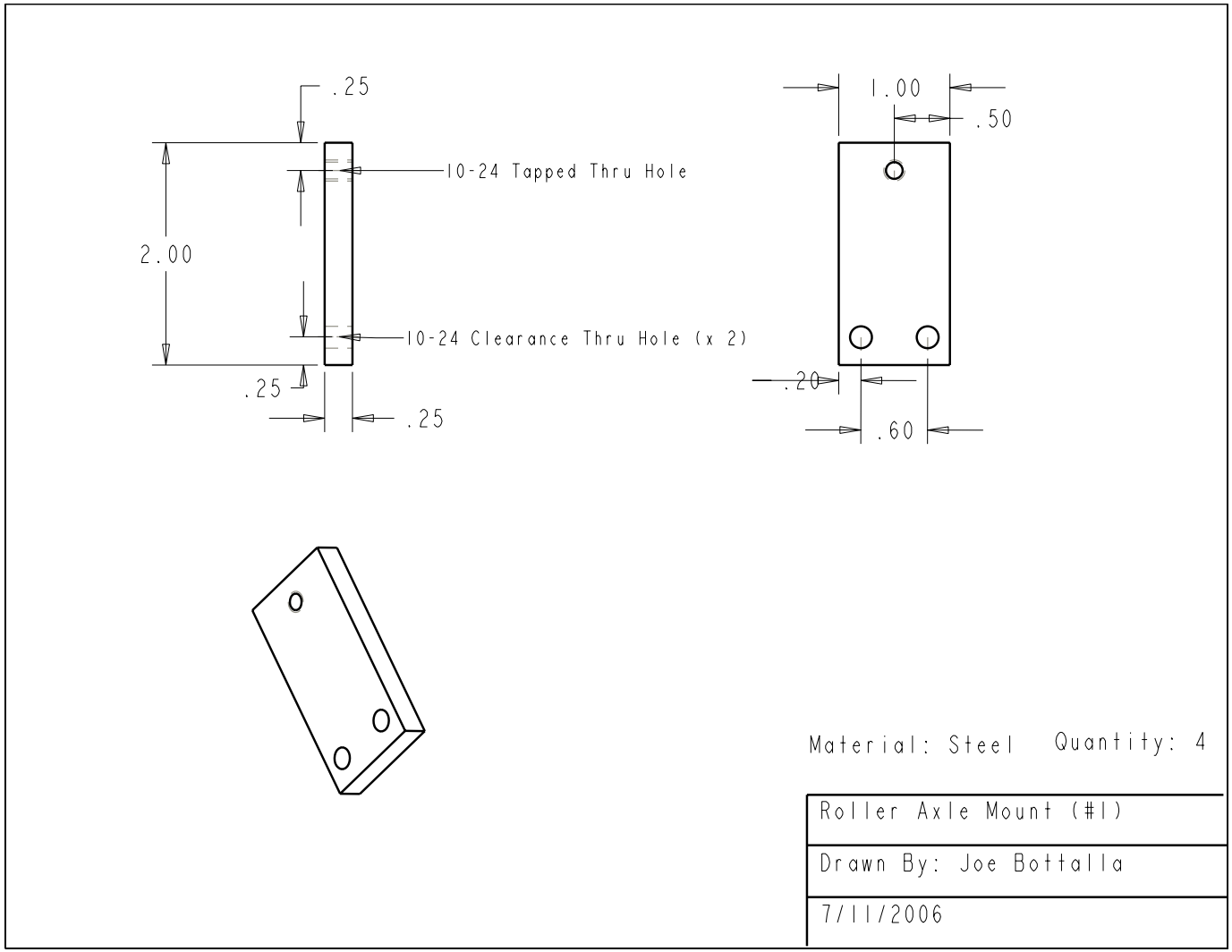

Fig. F.14: Roller Axle Mount No.1 Drawing

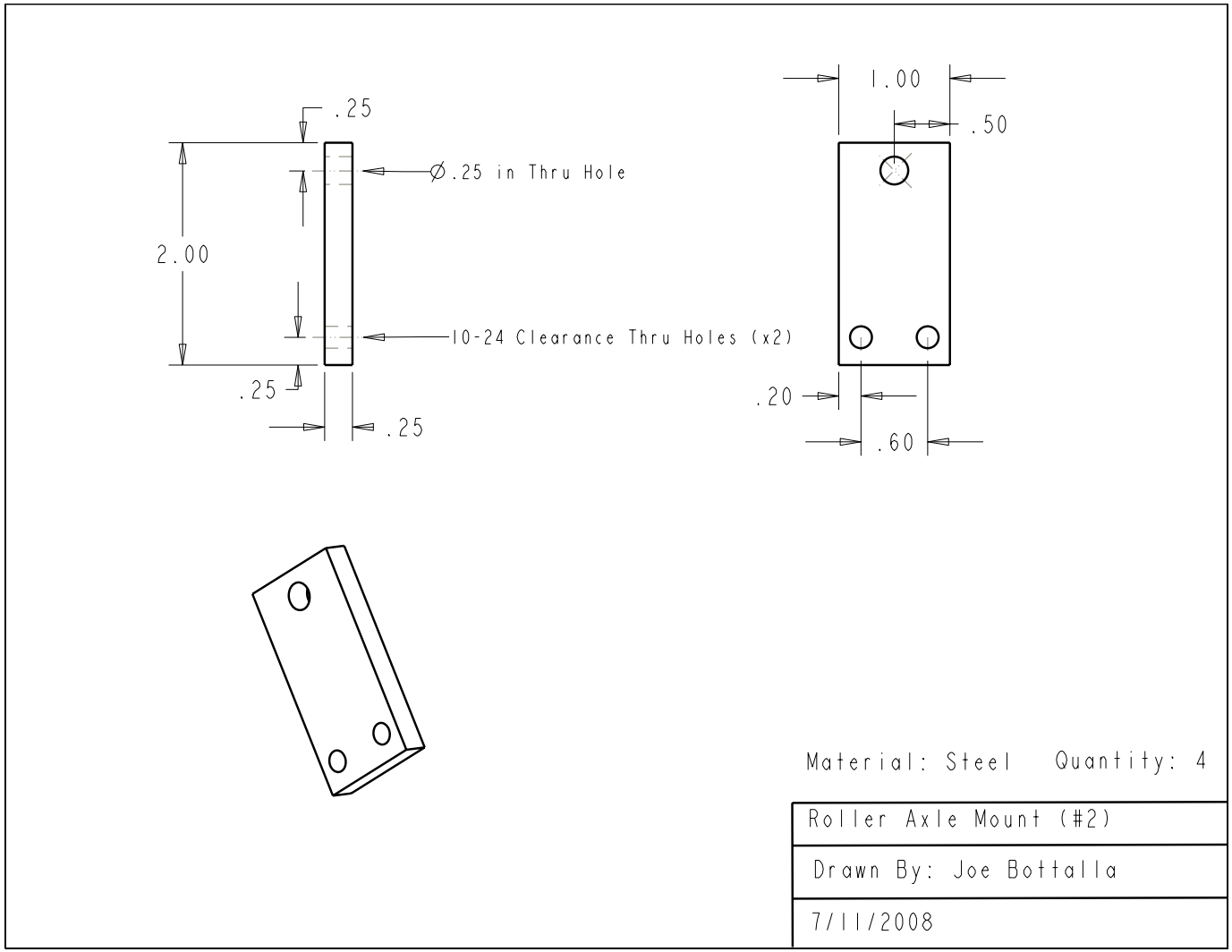

Fig. F.15: Roller Axle Mount No.2 Drawing

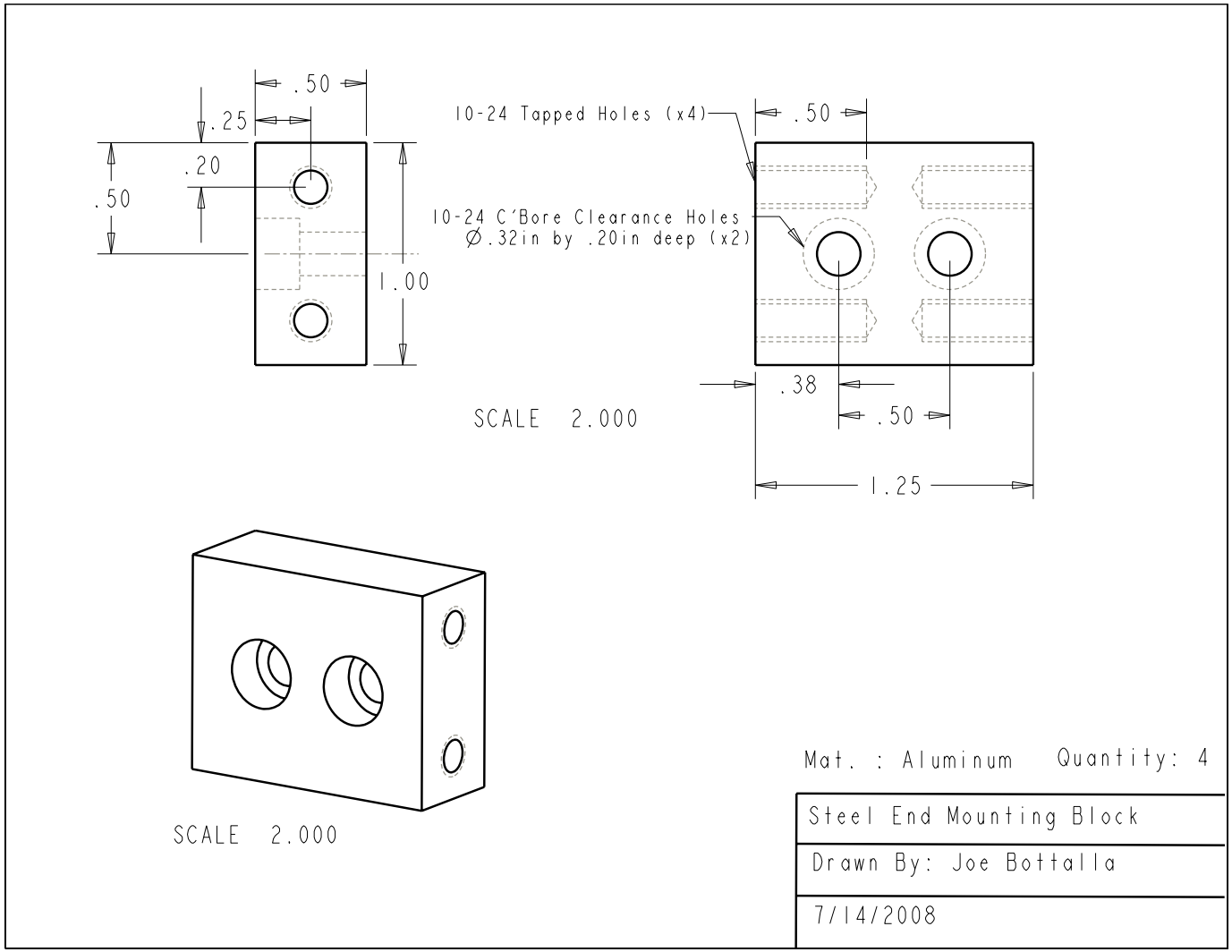

Fig. F.16: Steel End Mounting Block Drawing

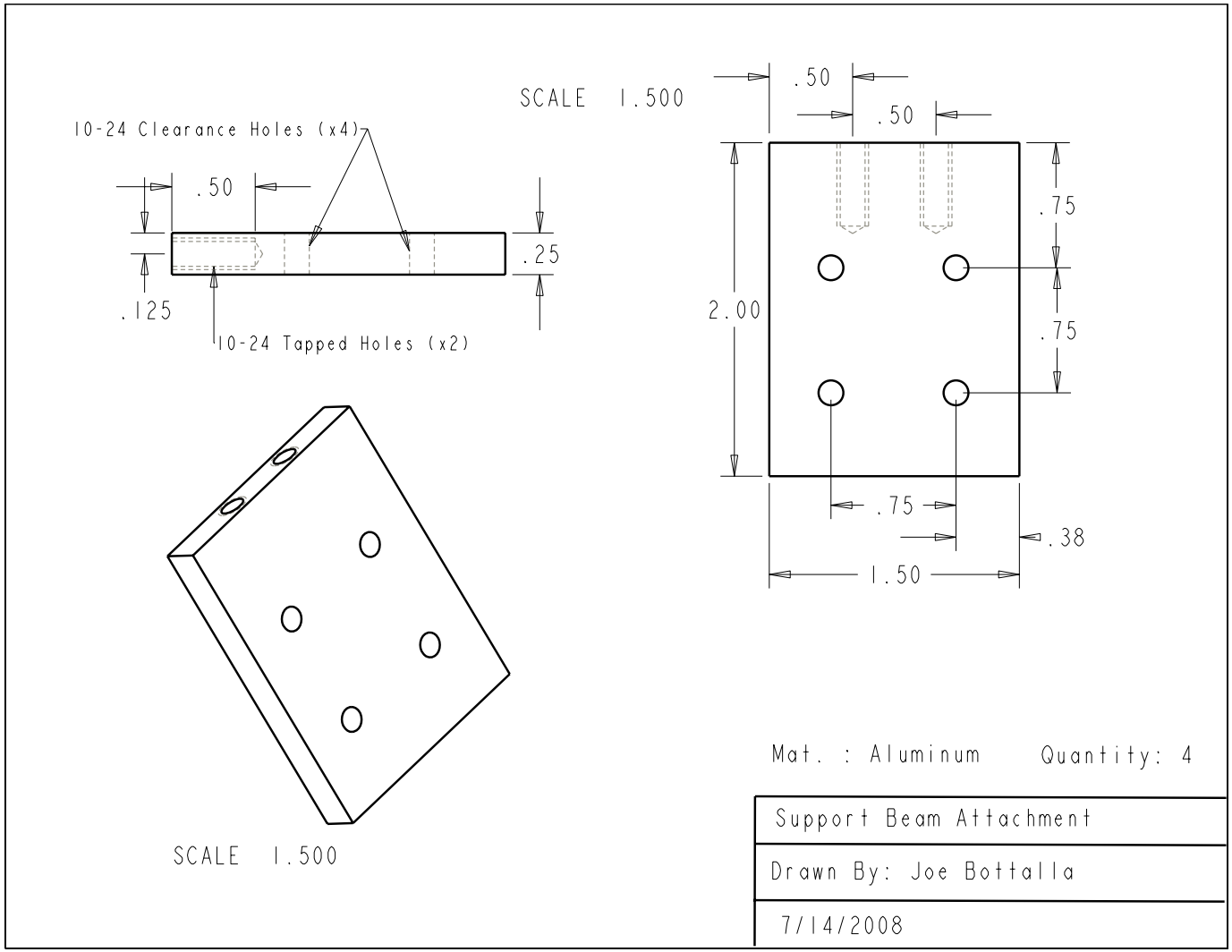

Fig. F.17: Support Beam Attachment Drawing

Appendix G - Assembly of Bypass Facility with Full Test Model

The step by step assembly process for the bypass facility with the full test model is as below:

1. *Position the squre-to-round section on the inlet of the wind tunnel diffuser using C-clamps and secure the section using bolts through the holes provided. holes.(Fig. G.3)*

2. *Place tunnel section B on the 40 inch by 38 inch frame with support pads. Maneuver the entire piece to a position in front of the square-to-round piece using the casters. The round flange previously installed on tunnel section B should be facing the round end of the square-to-round piece.*

3. *Place the first circular alignment plate (Fig. G.1) within tunnel section B and close to the downstream section. The plate should be placed vertically to cover the entire annulus of the axisymmetric test section.*

4. *Position the alignment laser pointer (Fig. G.2) on a tripod and place the tripod with the laser at a distance far upstream from tunnel section B. Adjust the height of the tripod as well as the pitch and yaw angles of the laser pointer so that the laser beam hits the center of the circular alignment plate. Once the laser pointer is correctly positioned, DO NOT move the entire laser set-up. The center of the circular alignment plate is marked by a small hole.*

5. *Place the second circular alignment plate within tunnel section B at the upstream section. Adjust the position of the frame with tunnel section B to position the laser dot at the center of the second circular alignment plate. The frames can be raised or lowered by adjusting the casters.*

6. *Once tunnel section B is aligned, remove the first circular alignment plate at the down-*

stream section and connect tunnel section B onto the square-to-round section by gently maneuvering the frame to prevent misalignments. The second circular alignment plate can also be removed.

7. *Secure tunnel section B to the square-to-round section using the bolt holes. Raise the casters of the frame and release the swiveling mounts to secure the entire frame with the axisymmetric section on the ground.(Fig. G.4)*

8. *Position the aft-body diffuser of the test model with the center beam within the annulus of tunnel section B so that the holes on the aft-body diffuser struts match the slot holes drilled on axisymmetric section. Insert the screws through the slot holes and into the struts without tightening them. The aft-body diffuser with the center beam should now be cantilevered in the axisymmetric section.(Fig. G.5)*

9. *Slide the center cavity of the engine baseline models onto the center beam according to the sequence shown in Fig. 2.2. Part E of the engine baseline model should be inserted first followed by the other four parts. Make sure that the rounded corner in each model is positioned at the 12 O'Clock position.(Fig. G.6)*

10. *Attach the gearbox fairing and crane beams on the underside and upperside of the engine baseline models respectively.(Fig. G.7)*

11. *Place the rotating test section on the second 40 inch x 38 inch frame with rollers. Lubricate the inner surfaces of the gear housing with Vaseline.*

12. *Carefully maneuver the rotating test section C using the frame casters so that the engine baseline models with blockage components are inserted within the annulus of the axisymmetric test section. Extreme care should be taken as not to damage the crane beam and gearbox fairing component.*

13. *Attach the fixed gear bearing on tunnel section B into gear housing A located on the end section of the rotating test section C to connect the two axisymmetric test sections. Raise the casters of the frame and release the swiveling mounts to secure the entire frame with rotatin test section C on the ground.(Fig. G.8)*

14. *Place the gear stepper motor on the cross beam of the angled supports on the rotating test section. Insert the spur gear on the shaft of the stepper motor to mesh the gear teeth of the spur gear with the ring gear attached on gear housing A. Lock the spur gear into position with the aluminum key and secure the entire stepper motor set-up on the cross beam with bolts through the motor base plate.*

15. *Place tunnel section A on the 40 inch by 22 inch frame with support pads. Using the frame casters, attach the fixed gear bearing on tunnel section A into the gear housing B on the rotating test section C to connect the two axisymmetric sections.*

16. *Slide the contraction cone into the annulus of tunnel section A and the center cavity of the contraction cone onto the remaining end of the center beam. The location of the screw holes on tunnel section A should match the screw holes on the contraction cone struts. If not, remove the screws in the slot holes in tunnel section B and adjust the position of the entire model within the axisymmetric sections.*

17. *Secure the contraction cone, and hence the entire test model, into the axisymmetric sections by tightening two set screws into the set screw holes located on the underside of the contraction cone. This process involves reaching into the annulus of tunnel section A with an Allen wrench.*

18. *Raise the casters of the frame and release the swiveling mounts to secure the entire frame with tunnel section A on the ground.*

19. *Position the second square-to-round section on the 15 inch by 15 inch square end of the wind tunnel inlet using C-clamps. Secure the piece using the bolt holes.*

20. *Maneuver the wind tunnel inlet to connect the inlet and square-to-round section with tunnel section A. The wind tunnel inlet can be raised or lowered by adjusting the height of the inlet casters. Insert bolts through the square-to-round section and the round flange installed permanently on tunnel section A to complete the entire assembly of the bypass facility.(Fig. G.9 and Fig. G.10)*

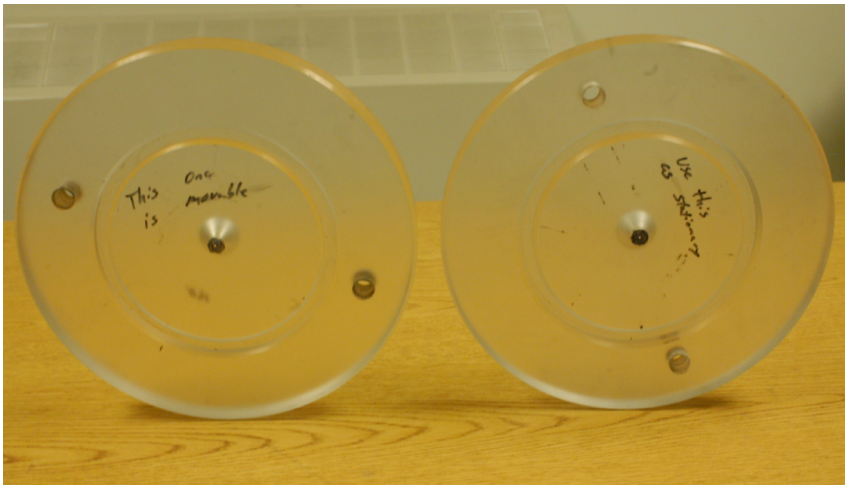

Fig. G.1: Circular Alignment Plates used for Alignment of Axisymmetric Pieces

Fig. G.2: Laser Used for Alignment of Axisymmetric Pieces

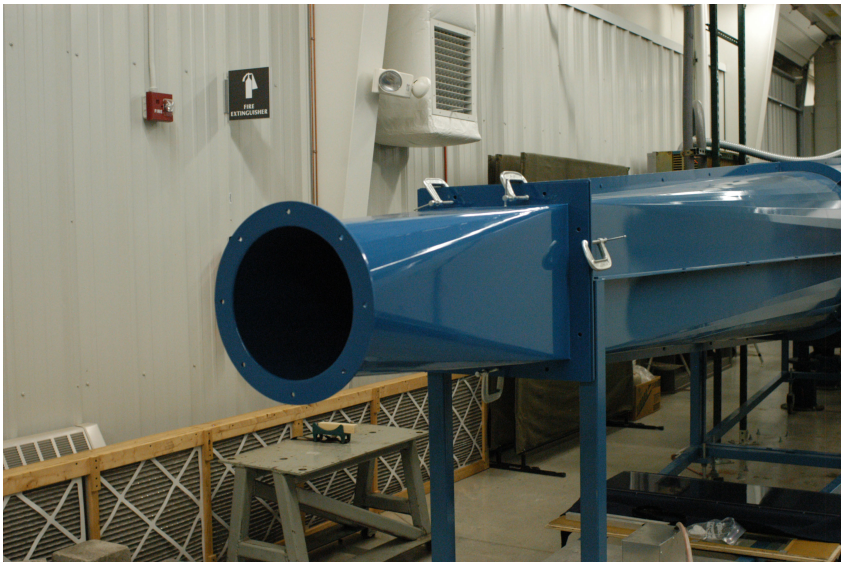

Fig. G.3: Step 1- Attach Square-To-Round Piece to Diffuser

Fig. G.4: Step 2- Tunnel Section B Aligned and Attached to Square-To-Round

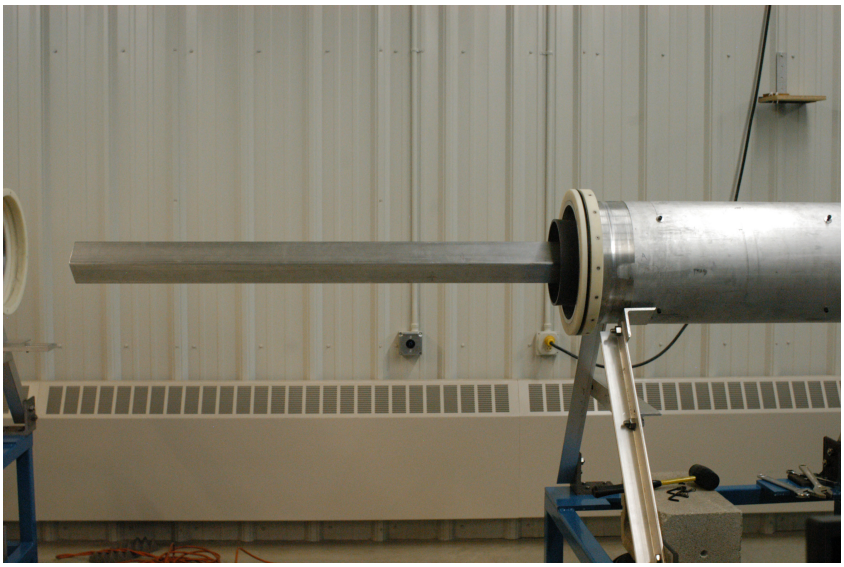

Fig. G.5: Step 3- Insert and Attach Aft-Body Diffuser with Center Beam into Tunnel Section B

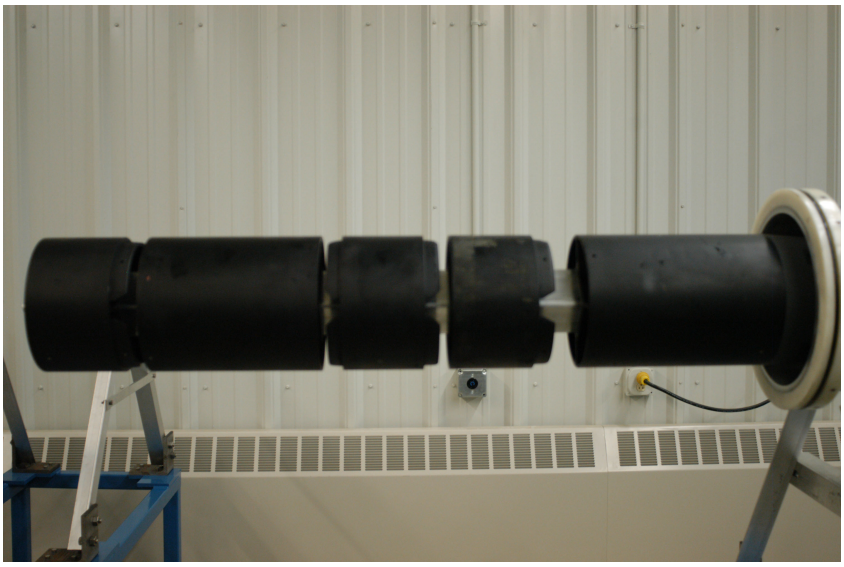

Fig. G.6: Step 4- Insert the Engine Baseline Models according to Sequence on Center Beam

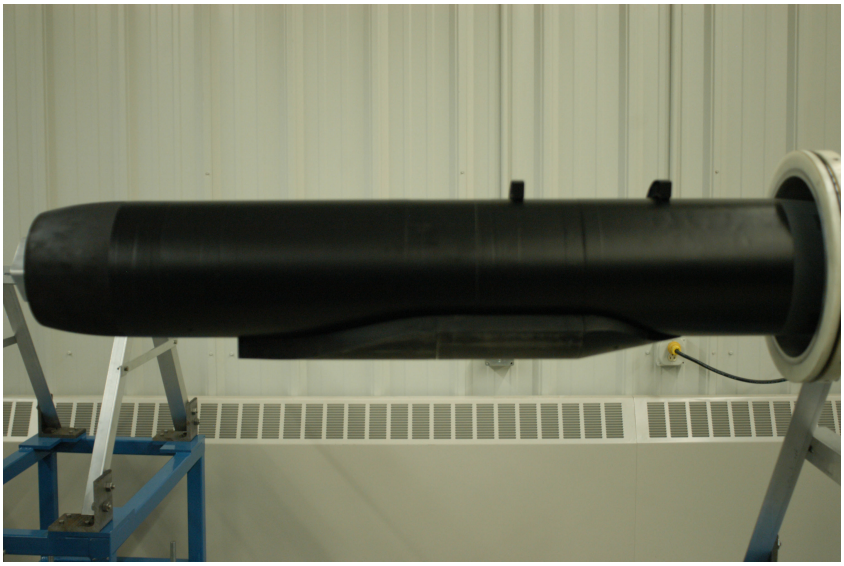

Fig. G.7: Step 5- Attach Blockage Components (Gearbox Fairing and Crane Beams) on Engine Baseline Model

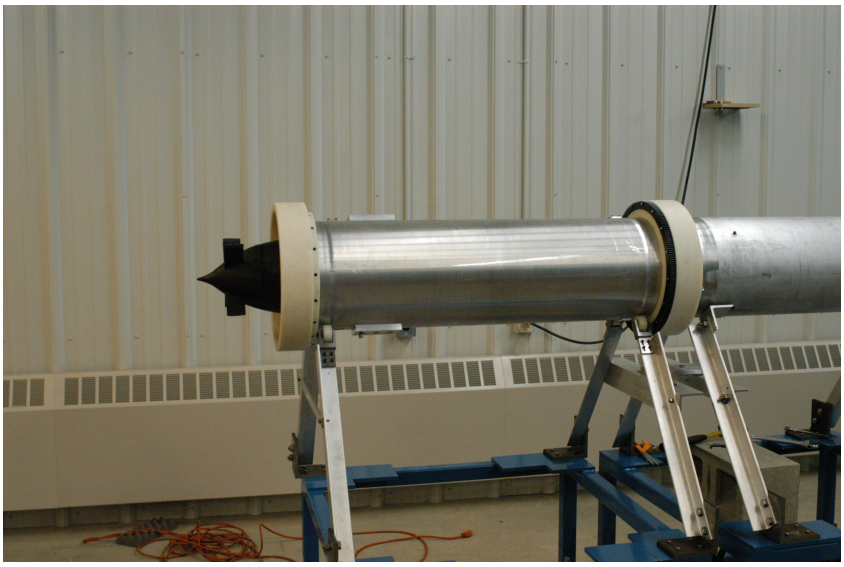

Fig. G.8: Step 6- Attach Rotating Test Section C onto Tunnel Section B and over the Test Model

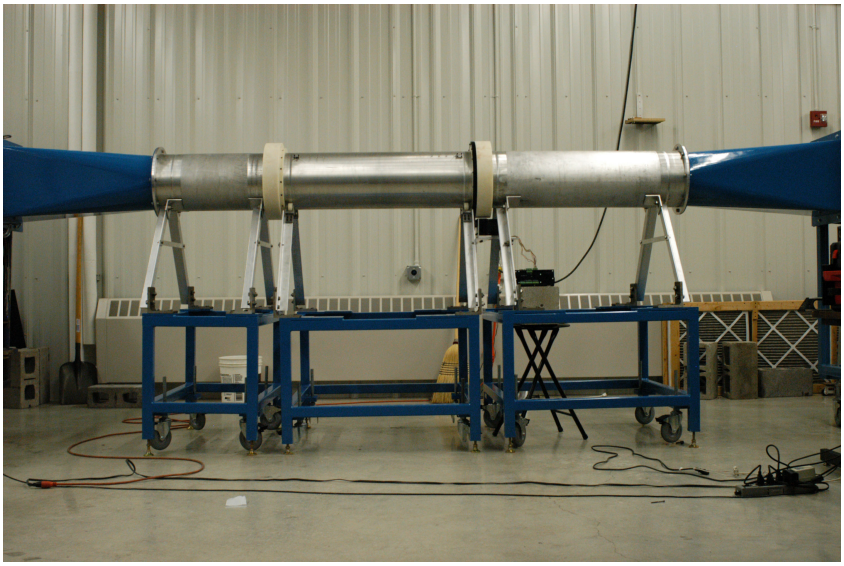

Fig. G.9: Step 9- Attach Tunnel Section A onto the Rotating Test Section C. Secure Wind Tunnel Inlet on Tunnel Section A

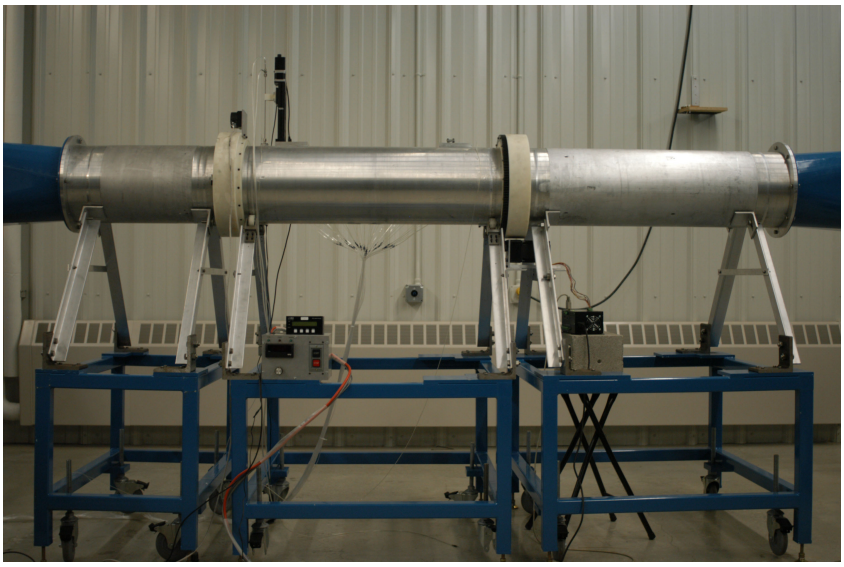

Fig. G.10: Step 10- Final Assembly of Bypass Facility with Pneumatic Connections in Place for Data Acquisition

Appendix H - Miscellaneous Drawings of Bypass Facility Components

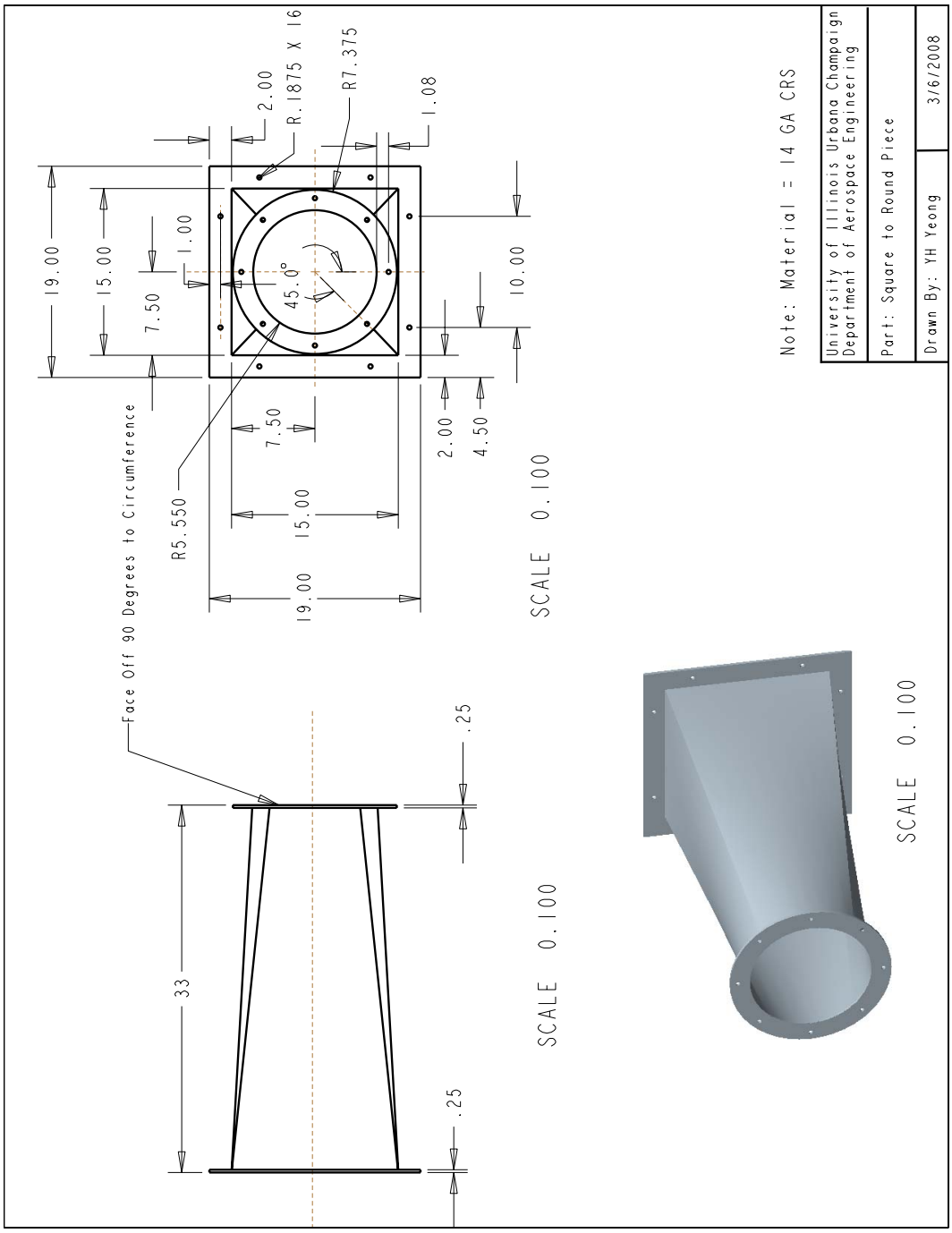

Fig. H.1: Square-to-Round Section Drawing

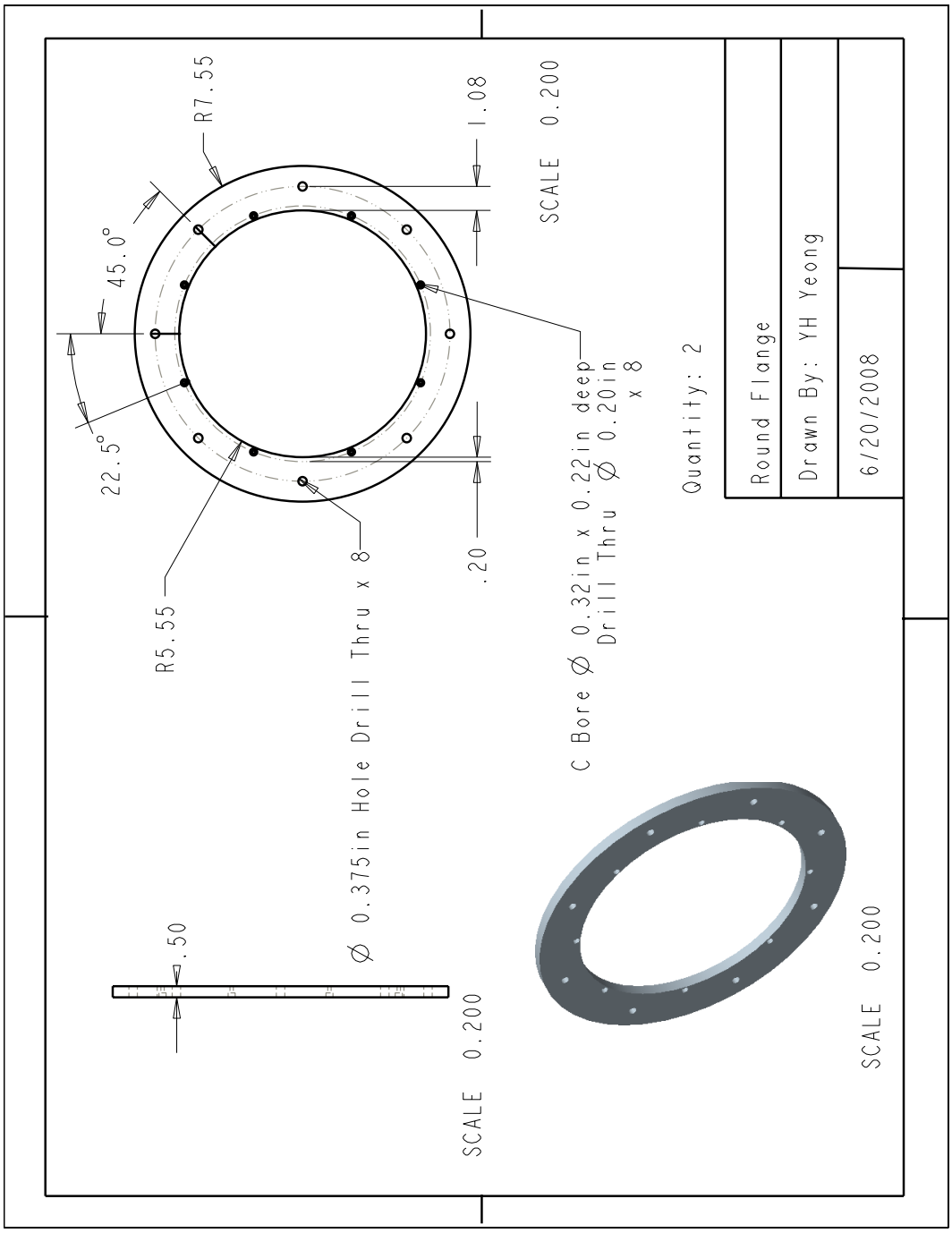

Fig. H.2: Round Flange Drawing

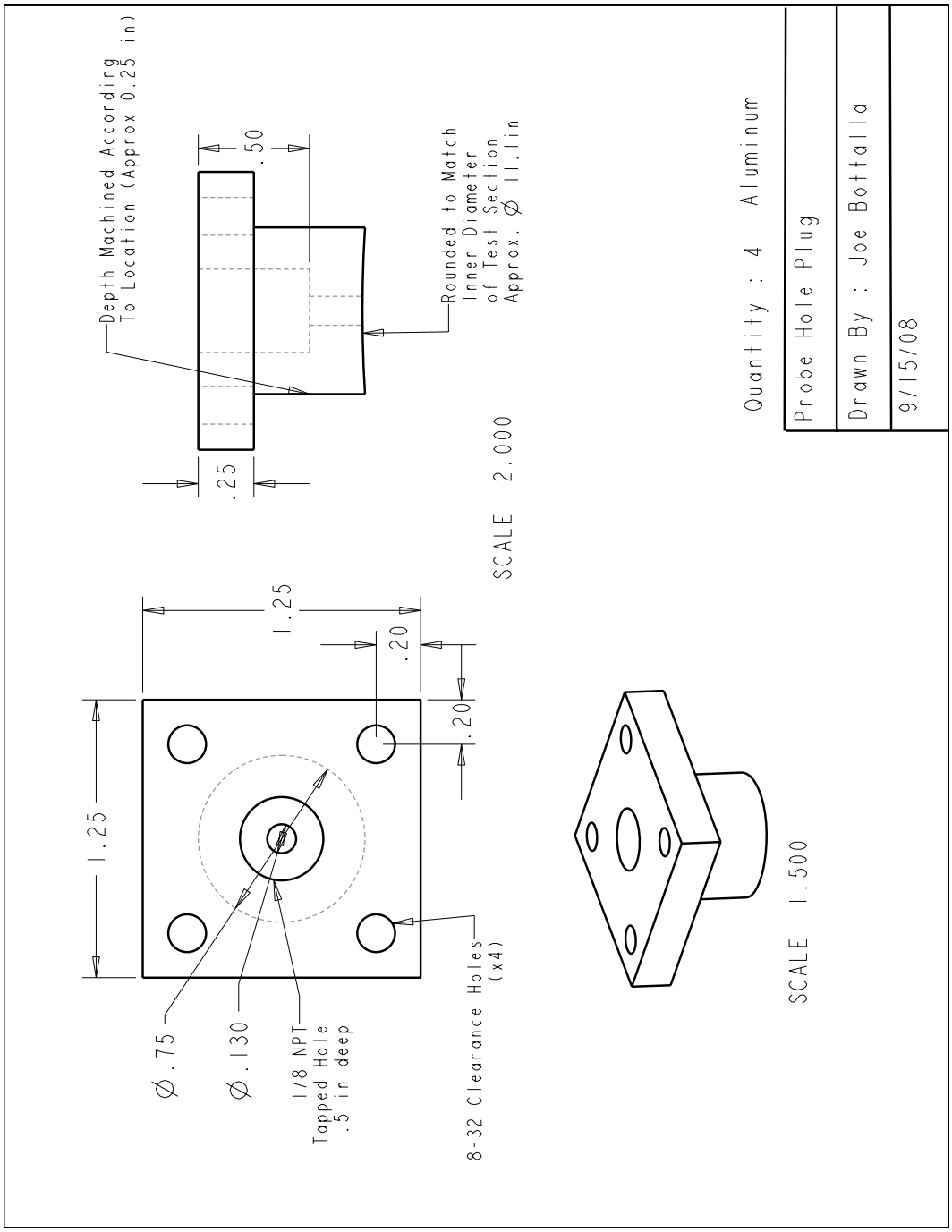

Fig. H.3: Probe Plug Drawing

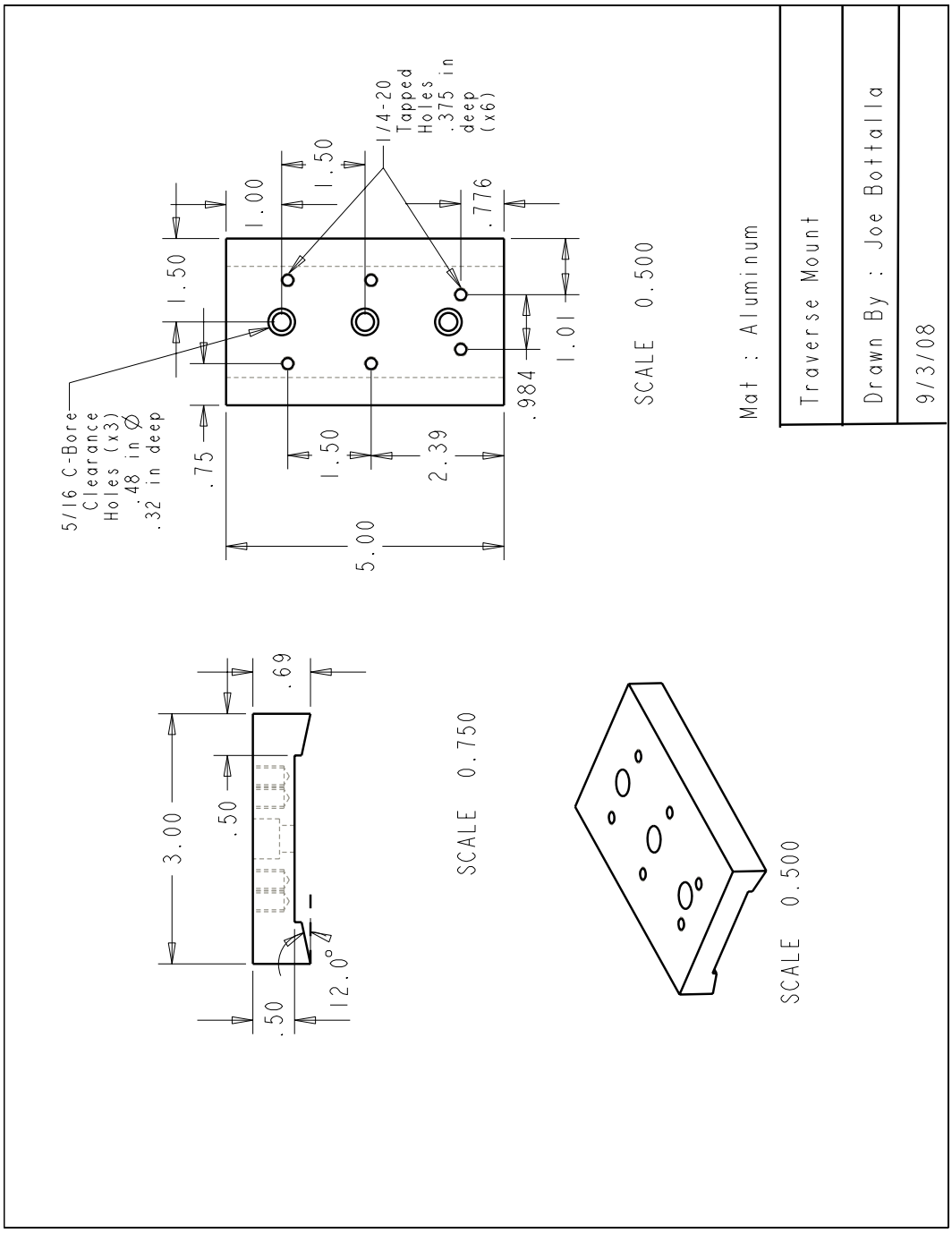

Fig. H.4: Traverse Mount Drawing

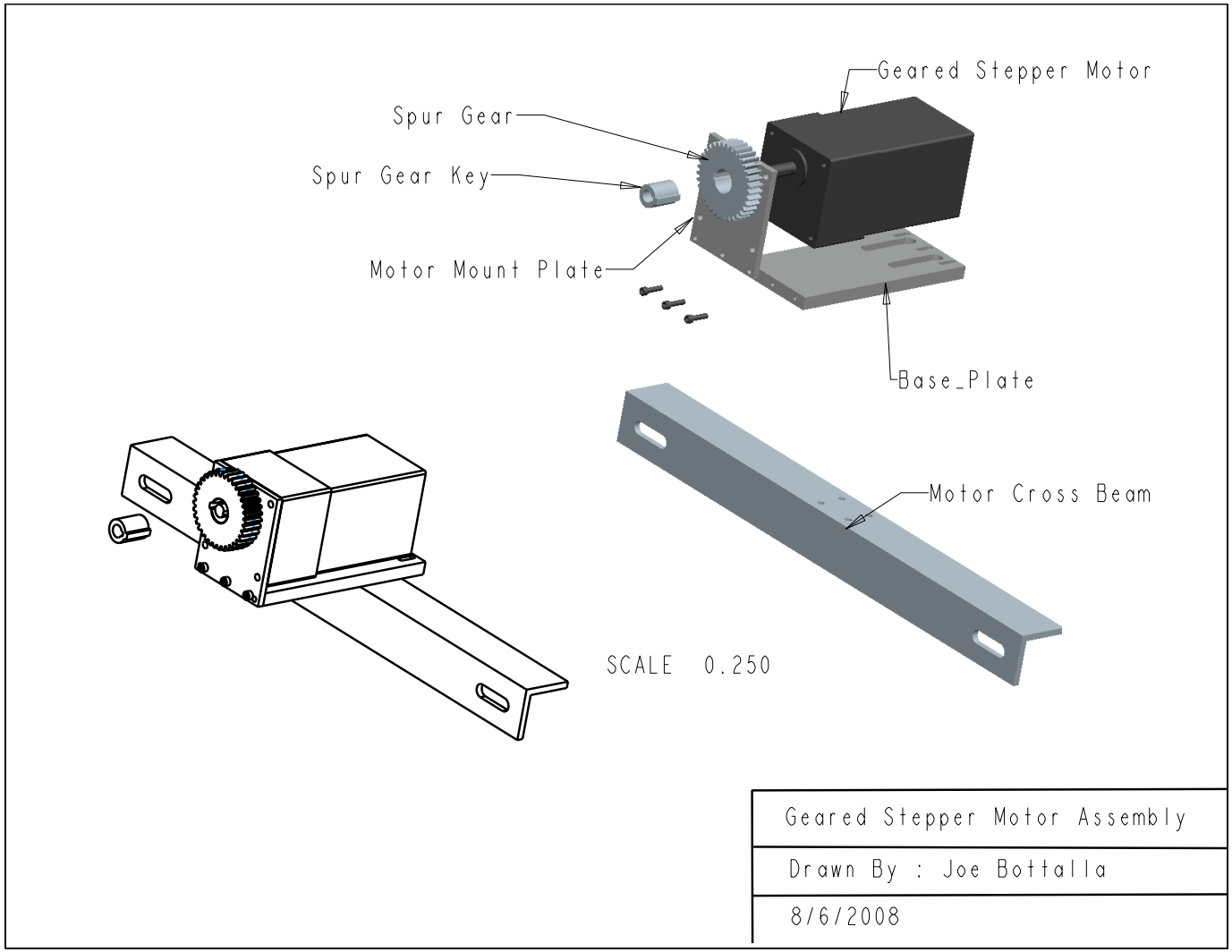

Fig. H.5: Set-up of Gear Motor with Support Components

Appendix I Linear Traverse and Inclinometer

The motorized linear traverse is used to traverse the pressure probes in a radial manner across the bypass annulus. The device is a Zaber Model KT-LSR150B. It has the capability of traversing a maximum distance of 150 mm or approximately 5.9 inches. This distance is equivalent to 305624 microsteps. Therefore, the device has the range to traverse the pressure probes from the wall of an empty test section to the centerline of the axisymmetric piece. A potentiometer knob located at the top of the device allows the user to manually control the traverse in both speed and direction. At the same time, the traverse can be connected to a computer via a RS-232 serial cable for remote access and control using a Labview program. The linear traverse is also a feedback device, therefore the distance the traverse has travelled is known. To attach a pressure probe to the linear traverse, a clamp was made out of Nylon and attached to the traverse plate of the device. The clamp contains a slot measuring 0.135 inches in diameter machined to hold the pressure probe. The clamp is tightened by placing two No. 1 screws from the side and through the slot, hence securing the position of the pressure probe wihtin the slot. This is shown in Fig. I.2.

As described in Section 2.2.1.5, a stepper geared motor with a controller was used to provide the neccessary torque to rotate the test section. However, since the controller does not have feedback capability, the angle of the test section after a rotational step cannot be acquired. To correct for this problem, an inclinometer was attached to the test section. This device is a US Digital Model A2T absolute optical inclinometer with a resolution of 0.1° (Fig. I.2). This device has the capability of detecting tilt on a single axis for the full range of 360° updated at 250 times per second. It also contains an EEPROM so that information such as the set zero position can be retained within the device even though the power has been turned off. The inclinometer is connected to the data acquisition computer via a serial

encoder interface (SEI) interfacing to a RS-232 serial port and controlled using LabVIEW.

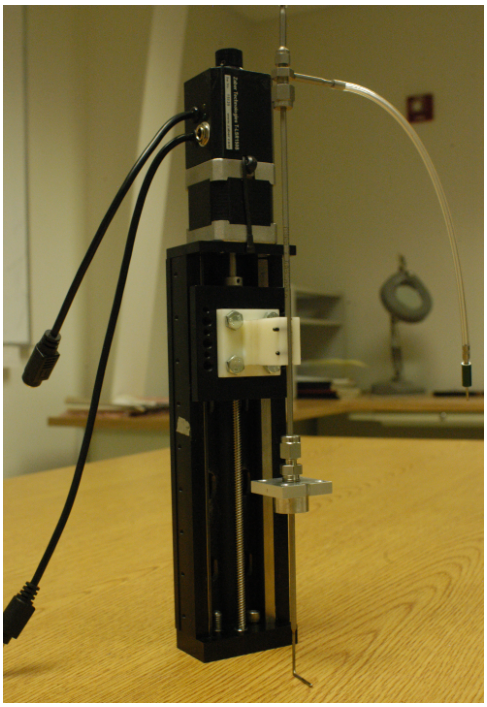

Fig. I.1: Linear Motorized Traverse with Clamp and Probe Attached

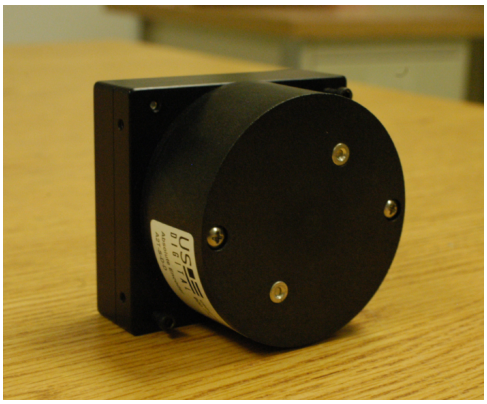

Fig. I.2: Inclinometer